ETH

Eidgenössische Technische Hochschule Zürich
Swiss Federal Institute of Technology Zurich

Enhanced Single-Shot Readout
for Quantum Feedback Experiments

Philipp Kurpiers

Master Thesis
in the Quantum Device Lab
Laboratory for Solid State Physics

Professor: Prof. Dr. Andreas Wallraff
Supervisor: Yves Salathé

Zürich, March 2013

Contents

1 Introduction

"... trying to find a computer simulation of physics, seems to me an excellent program to follow up ... and if you want to make a simulation of nature, you'd better make it quantum mechanical, and by golly it's a wonderful problem, because it doesn't look so easy."

Richard Feynman

The starting point of quantum computation can be found in the 1970s and 1980s where first theoretical models of reversible computations including the laws of quantum mechanics have been developed, inter alia, by Edward Fredkin, Tommas Toffoli [32], Charles H. Bennett [8] and David Deutsch [22]. Richard Feynman's ideas of the simulation of physics by quantum system [27] as well as the discovery of quantum algorithms, e.g. Shor's algorithm [73] or Grover's algorithm [44], which exceed classical ones by a crucial speed-up, leading to an enormous increase of research in the field of quantum information processing in the last decades. Various physical systems are studied for a realization of a quantum computer where David P. DiVincenzo introduces five plus two criteria for the physical implementation of a quantum computer [24].

First, the physical system has to be scaleable and to consist of well defined quantum mechanical two-level systems - quantum bits or qubits. Second, the ability to initialize the states of the qubits in their ground states has to be given. This criterion is necessary for each computational process where the registers should be in a known state at the beginning of the computation. Furthermore, for correcting errors in the quantum computation additional qubits in a low-entropy state are required. In principle, two initialization methods can be distinguished. Passively waiting will equilibrate the qubits with a cold thermal environment in the scale of the qubit transition frequency and hence, prepare them in their ground states. To improve the initialization an active reset of the qubit minimizes residual thermal excitations of the qubits and can rapidly evacuate the entropy from the system [38].

The third and fourth criteria emphasize long coherence times of the qubits, especially longer than the quantum gate operation times and a universal set of these gates. Fifth, the readout of the individual qubit states must be possible after the computation without changing the state of the other qubits. In principle, a limitation in the efficiency of the readout can be circumvented by repeating the algorithm with the same input. But for quantum algorithms which involve a classical channel a readout of the qubit in every single measurement is essential.

Finally, the possibility to transmit the state of one qubit to another is essential for quantum computation as well as quantum communication. Therefore, additional 'flying qubits' are proposed by DiVinzenco which should interconnect with the stationary qubits and can faithfully be transmitted between the different locations. A further algorithm to perform this task is the quantum teleportation protocol [6] which allows also to build a universal quantum computer in combination with the above mentioned five criteria [42].

At first, the majority of these criteria was fulfilled in ensemble quantum computing by NMR spectroscopy [20]. With this technique e.g. Shor's algorithm has been implemented in a 7-qubit quantum computer which allowed to factorize 15 [78]. A second physical system are photons which provide several degrees of freedom to serve as an implementation of qubits, e.g. the polarization and long distance quantum communication and quantum computation is performed with them [56]. Furthermore, physical qubits can be implemented between two energy levels of an ion trapped in an electric field which is an interesting system due to long coherence times and a high accuracy of the control of the single qubits [66].

A common problem especially of the first mentioned physical systems is their scalability and therefore, a solid state implementation seems a promising candidate where on-chip quantum processors can be realized. Therefore, two main architectures are in the focus of the current research. In one of them, the qubits are represented by the spins or the charge of electrons which are trapped in quantum dots [54], where in the other one qubits are realized in non-linear superconducting circuits. As a dissipation-free non-linear circuit element a Josephson junction [47] is included in this circuits resulting in an effective two-level system. The experiments of this thesis are performed in such a solid state architecture where the number of charges on one side of the Josephson junction is the relevant degree of freedom [49]. These charge qubits are coupled to a superconducting 1D resonator [81] which allows to read out the qubit as well as provides the possibility to implement universal qubit gates [28]. In this solid state system the interaction between microwave photons and artificial atoms can be studied in a similar way as in the field of cavity quantum electrodynamics (cavity QED) and hence is called circuit QED.

The main focus of the presented thesis lies on the realization of closed-loop quantum algorithms in single- and multi-qubit circuit QED systems. In a closed-loop system a situation exists, where at least two dynamical systems are combined in such a way that each system affects the other one. For this purpose, the basic requirements of closed-loop quantum algorithms are explained in Chapter 2 where moreover the quantum circuits of the experimentally implemented algorithm are detailed. First, the state initialization by measurement protocol is depicted followed by a consideration of the quantum teleportation algorithm. In Chapter 3, the realization of qubits in non-linear superconducting circuits will be introduced and the physical model of their coupling to a transmission line resonator will be described. Especially, the two-qubit readout will be analyzed in detail, because it is a necessary requirement for the realization of the full quantum teleportation algorithm. Chapter 3 ends with a description of the implementation of a two-qubit gate and a Josephson parametric amplifier, which allows to amplify a signal near the quantum noise limit [79]. The experimental setup is presented in Chapter 4 which includes a brief explanation of the measurement software. The experimental results of the single-qubit experiments are shown and analyzed in Chapter 5. Therefore, technical improvements of the setup are depicted at the beginning followed by an evaluation of the feedback loop to perform a quantum state initialization by measurement protocol. The realization of this protocol as well as a suppression of Rabi oscillation are described furthermore. Finally, the technical implementation and experimental results towards the realization of the full quantum teleportation algorithm are depicted where Chapter 6 is concluded with an experimental test of the feed-forward setup of this algorithm.

2 Quantum information processing

First, basic concepts of quantum information and quantum communication are discussed in this chapter. Therefore, the quantum bit as the quantum mechanical counterpart of the classical bit is introduced theoretically and a description of quantum operations is given. This introduction follows mainly the book of Nielsen and Chuang [60]. Furthermore, quantum protocols especially ones which include feedback loops are outlined.

2.1 Quantum bits

The fundamental unit of classical information and computation is the bit - a classical system with exactly two states, e.g. two positions of an electrical switch. The same holds for quantum computation and quantum information, where the information is encoded in a quantum mechanical two-level system - the quantum bit or qubit [71]. A general qubit state is given as a superposition of the so called 'computational' sates $|0\rangle$, $|1\rangle$:

$$|\psi\rangle = \alpha |0\rangle + \beta |1\rangle \tag{2.1}$$

where alpha and beta are complex numbers and fulfill the normalization condition:

$$|\alpha|^2 + |\beta|^2 = 1 \tag{2.2}$$

$|\alpha|^2$ is the probability to measure the qubit in $|0\rangle$ and $|\beta|^2$ to find it in $|1\rangle$. In principle, one qubit can be in an infinite number of superposition states, but only one bit of information can be extracted, if the qubit is measured. Therefore, it is reasonable to speak of a quantum bit. A common way to illustrate the state of a qubit is the representation on the Bloch sphere (Figure 2.1). For this $|\psi\rangle$ is written omitting a global phase which for a single qubit has no physical meaning as

$$|\psi\rangle = \cos(\theta/2) |0\rangle + e^{-i\phi} \sin(\theta/2) |1\rangle . \tag{2.3}$$

Each possible pure qubit state is located on the surface of the Bloch sphere. Mixed states in contrast, are an ensemble of pure states and thus lie within the sphere. The Bloch vectors of the computational state $|0\rangle$ and $|1\rangle$ are defined by the z axis reaching from the central point to the two poles. Any qubit operation corresponds to a rotation of the Bloch vector which allows an intuitive illustration.

Two important examples are the Pauli $\hat{\sigma}_x$ gate which is equal to a rotation of an angle π around the x axis or the Hadamard operation corresponding to a $\pi/2$ rotation around the y axis:

$$\hat{\sigma}_x = \begin{pmatrix} 0 & 1 \\ 1 & 0 \end{pmatrix}$$

$$\hat{H} = \frac{1}{\sqrt{2}}(\hat{\sigma}_x + \hat{\sigma}_z) = \frac{1}{\sqrt{2}} \begin{pmatrix} 1 & 1 \\ 1 & -1 \end{pmatrix} . \tag{2.4}$$
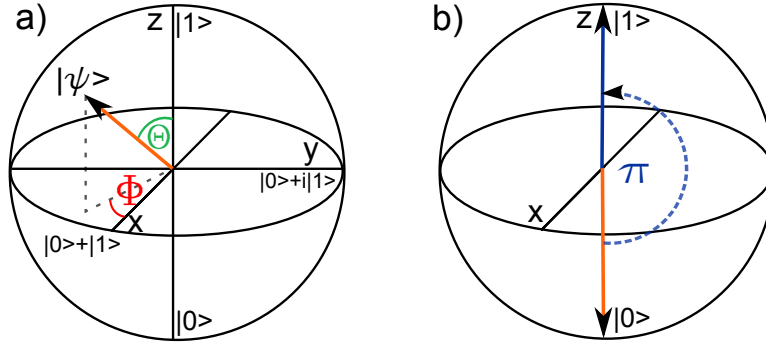
Figure 2.1: a) The Bloch sphere is depicted which represents the one-qubit state space. On the three orthogonal axis X, Y, Z the eigenvectors of the Pauli matrices $\hat{\sigma}_x$, $\hat{\sigma}_y$, $\hat{\sigma}_z$ are located.
b) Illustration of a 'π pulse around the x axis (Pauli $\hat{\sigma}_x$ gate).

This formalism can easily be expanded to multi-qubit states, where, e.g. a general two-qubit state can be defined by a superposition of the four basis states $|00\rangle$, $|01\rangle$, $|10\rangle$, $|11\rangle$:

$$|\psi\rangle = \alpha_{00} |00\rangle + \alpha_{01} |01\rangle + \alpha_{10} |10\rangle + \alpha_{11} |11\rangle \qquad (2.5)$$

Of particular interest are entangled states, because these states show stronger than classical correlations and thus, cannot be described as two independent systems [26] . For example, measuring one qubit of an entangled state leaves the other one in a completely mixed state meaning that it has 50 % probability to be in state $|0\rangle$ or else in state $|1\rangle$, if one considers only this subsystem.

Furthermore, entanglement is used in many quantum algorithms, e.g. in superdense coding. This algorithm allows to transmit two bits of information by sending only a single qubit [7]. Another example is the quantum teleportation scheme, in which an unknown quantum state is 'teleported' from one qubit to another spatially separated one by sending classical information only [6]. The Quantum teleportation algorithm will be described in detail in Section 2.2.2.

The preparation of entangled states requires two-qubit gates, where the controlled NOT (CNOT) gate has to be mentioned. This gate is the prototype for any multi-qubit gate which means that any quantum gate can be composed from single-qubit gates and the CNOT gate [60]. The CNOT gate performs the following operation

$$\begin{pmatrix} 1 & 0 & 0 & 0 \\ 0 & 1 & 0 & 0 \\ 0 & 0 & 0 & 1 \\ 0 & 0 & 1 & 0 \end{pmatrix} \qquad (2.6)$$

on the computational states expressed in the matrix representation and its circuit representation is shown in Figure 2.2.
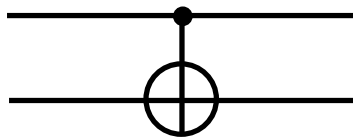

Figure 2.2: Quantum circuit representation of the CNOT gate.

2.2 Closed-loop quantum algorithms

Another essential requirement for many quantum algorithms is the closing of a feedback loop. By a feedback loop a situation is meant, where at least two dynamical systems are combined in such a way that each system affects the other one. By the implementation of a cleverly designed feedback loop a system can be made resilient to external influences or it can change its individual states [2]. A typical example is a thermostat which can be used to control the heating system of a building.
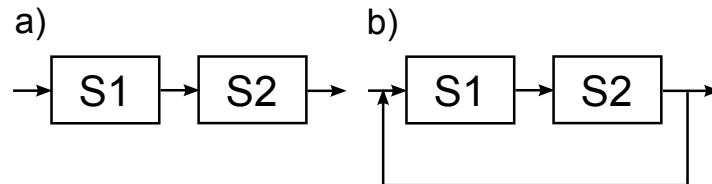

Figure 2.3: a) An open loop system where the signal is propagating along one way.
b) Closed-loop system setting an interconnection between the output of system 2 and the input of system 1.

In the area of quantum information error correction codes can be mentioned allowing to correct arbitrary errors on a single qubit [74]. In these schemes, one qubit state $|\psi\rangle$ is encoded in a specific way with other 'ancilla' qubits. In general, two strategies have been developed to perform this task where both require closed-loop systems. In the first approach, the original state $|\psi\rangle$ can be reconstructed by decoding the information stored in the ancilla qubits in a coherent way, which is a coherent-feedback operation [70]. Furthermore, the ancilla qubits can be reset by a classical feedback scheme, if the code has to be repeated. In a second strategy, the ancilla qubits can be measured and a classical feed-forward operation can be performed to correct the detected error and obtain $|\psi\rangle$ [65]. This operation is called feed-forward, because the result of the measurement affects a different part of the system as the part which is measured [75].

Further examples are the aforementioned quantum teleportation algorithm and qubit initialization by measurement, which will be described in more detail.

2.2.1 Qubit state initialization by measurement

Physical qubits have finite lifetimes, therefore one way to initialize a qubit in its ground state is to wait much longer than the qubit lifetime. This method which is called passive initialization has the disadvantages that it is limited by the residual thermal excitation of the qubit and becomes slow for long qubit lifetimes. To circumvent these drawbacks one can initialize the qubit by performing a measurement of its state and applying a measurement result dependent pulse. In other words, if the qubit is measured in its ground state no pulse should be given, but if the qubit is measured in its excited state, its population is inverted by a $\pi-$pulse. Hence, the initialization can be performed much faster as well as thermal excitation and decay is only relevant during the feedback time [67].

2.2.2 **Quantum teleportation**

The quantum teleportation algorithm is of great importance for quantum communication [13] and quantum computation [16,86]. The principal idea of the protocol is that one is able to transfer the state from one qubit to another, whereby neither the qubit state nor the location of the receiver has to be known [6]. This is also of advantage, because a quantum state cannot be copied (no-cloning theorem of quantum information [84]). Therefore, a quantum state can only be transferred by sending the qubit directly, applying a direct interaction between the qubits or letting them interact with a 'flying' qubit.

In the teleportation scheme the transfer of information is split into a classical and a pure non-classical part. First, the sender (Alice) and the posterior receiver (Bob) share a fully entangled pair of qubits establishing the option for non-classical interaction. At the next step, Alice entangles her qubit further with a third qubit, whose state $|\psi\rangle$ should be teleported. The resulting three qubit state is given by

$$2\,|\phi\rangle = |\phi^+\rangle_A \otimes |\psi\rangle_B + |\phi^-\rangle_A \otimes [\hat{\sigma}_z\,|\psi\rangle]_B + |\psi^+\rangle_A \otimes [\hat{\sigma}_x\,|\psi\rangle]_B + |\psi^-\rangle_A \otimes [-i\hat{\sigma}_y)\,|\psi\rangle]_B \quad (2.7)$$

where $|\phi^{+/-}\rangle$ and $|\psi^{+/-}\rangle$ label the four Bell states and A, B Alice's or Bob's qubits.

Thereafter, Alice performs a measurement on her qubits projecting Bob's qubit in one of the four states $|\psi\rangle$, $\hat{\sigma}_z\,|\psi\rangle$, $\hat{\sigma}_x\,|\psi\rangle$ or $-i\hat{\sigma}_y\,|\psi\rangle$. During that process, the original state $|\psi\rangle$ gets destroyed in accordance with the no-cloning theorem.

Now the classical information part comes into play, where Alice sends Bob two bits of information containing her measurement result. With this information Bob is able to perform the appropriate inverse operation and end up with his qubit in state $|\psi\rangle$. Two additional remarks have to be considered for the classical information channel: First, these channels lead to a closed-loop system in the quantum teleportation algorithm. Furthermore, this process is a feed-forward operation, because the measurement of Alice's qubits affects Bob's qubit in contrast to a feedback on her system. Second, they restrict the information exchange to the speed of light.

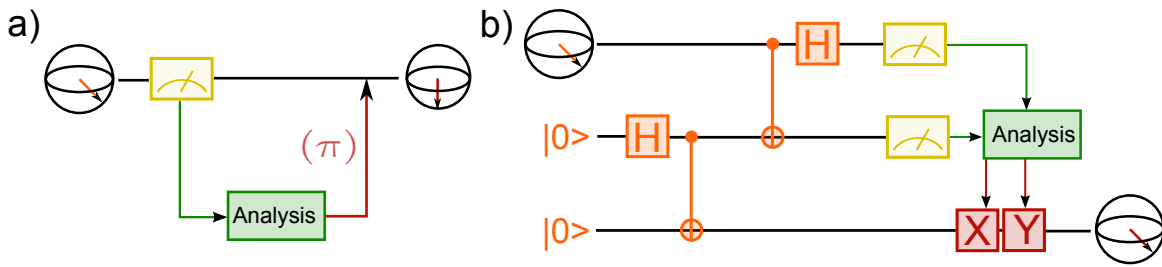Figure 2.4: a) Scheme of the qubit state initialization by measurement, where a measurement dependent $\pi-$pulse is used. b) Quantum teleportation scheme. H denotes the Hadamard gate and X (Y) the Pauli $\hat{\sigma}_x$ ($\hat{\sigma}_y$) gate. Note that $\hat{\sigma}_z$ is equal to $-i\hat{\sigma}_x\hat{\sigma}_y$. The double lines symbolize the classical information channel closing the loop in this circuit.

3 Implementation in superconducting circuits: circuit QED

A promising physical implementation of qubits in solid state systems is based on superconducting circuits including Josephson junctions. Superconducting qubits can be produced on a chip allowing good scalability and the design of the different system parameters, e.g. the qubit transition frequencies. Furthermore, the interaction between qubits is controllable and fast. Increasing coherence times have been achieved in the recent years allowing to perform more extensive quantum algorithms. Another feature making these qubits very interesting is that superconducting circuits are of macroscopic size, but show quantum features such as entanglement or energy quantization [18].

In this chapter main aspects of this implementation are explained which are relevant during the present thesis. Furthermore, several theoretical derivations are underlined with experimental results. First, the 'cavity' which is used in the experiments to read out and couple the qubits is described in Section 3.1 consisting of a superconducting transmission line. In Section 3.2 the architecture of the artificial atom will be detailed by starting with its basic element - the Josephson junction - and going towards a noise-insensitive superconducting charge qubit design - the transmon. By coupling these two systems a cavity quantum electrodynamics (cavity QED) system accrues in a superconducting circuit and is called circuit QED. The basic theoretical model of circuit QED systems will be introduced and adapted for the experimental purpose to read out the qubit state through the resonator in Section 3.3. This model will be expanded to a two-qubit system and especially, the requirements for an optimal single-shot readout will be detailed. Therefore, the analytical solutions in the steady state as well as non-steady state case are derived and analyzed in Section 3.4. Furthermore, a method which includes two measurement tones for the readout is proposed in Section 3.5. A description of the single-shot readout fidelity as well as the optimal threshold is given in Section 3.6 for single- and two-qubit systems. Furthermore, the implementation of the a two-qubit gate via a virtual photon inside the resonator is explained in Section 3.7. Finally, the Josephson parametric amplifier will be described which amplifies the signal with a noise figure near the standard quantum limit and hence, allows the single-shot readout of the qubit state with high fidelity.

3.1 Coplanar waveguide resonator

In the experiments a coplanar waveguide (CPW) resonator is used as 'cavity'. The CPW is a 1D transmission line with its well known 3D counterpart - the coaxial cable. Its center pin is separated by a small distance from the lateral ground planes and lies within the same plane (see Figure 3.1). Short pieces of the transmission line can be modeled by lumped-element circuits. A detailed description of the electrical properties of a coplanar waveguide can be found in the book of Pozar [62].

A high impedance resonator, which is used in the experiments of this thesis, is created by terminating the transmission line by two open circuits with impedance $Z_l = \infty$ at a distance $l = \text{n} \frac{\lambda}{2}$ where λ is the wavelength and n an arbitrary integer. The resulting resonance frequency of the resonator is given by [41]:

$$\omega_r = 2\pi \frac{1}{\sqrt{L_l C_l}} \frac{1}{2l} \tag{3.1}$$

In nonmagnetic materials the capacitance per unit length C_l and inductance per unit length L_l are only geometry dependent. This leads to a a characteristic impedance $Z_0 = \sqrt{L_l/C_l} \approx 50\,\Omega$ for a typical width w= 10 μm of the center pin and a gap size s= 4.5 μm [5]. The resonator can be capacitively coupled to transmission lines at both ends. Due to the impedance mismatch these gap capacitors act as dielectric mirrors. An asymmetric coupling seems reasonable, because on the input side an arbitrarily strong coherent signal can be applied to drive the resonator, while it is desired that most of the photons leak out of the resonator at rate $\gamma_{\text{out}} \approx \kappa$ at the output side. Therefore, about a 100 times larger output capacitor than the input capacitor is used which causes a much stronger coupling to the output than to the input.
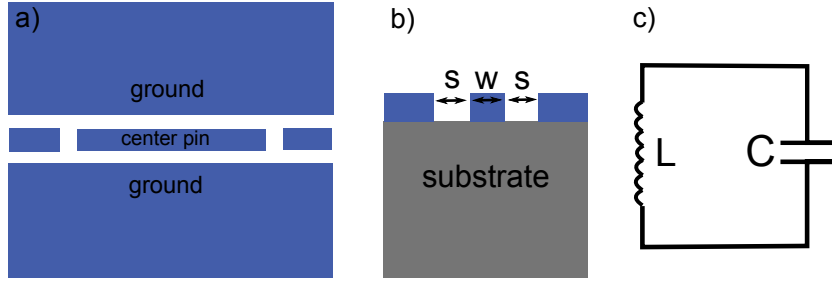
Figure 3.1: Coplanar waveguide resonator geometry: a) Top view of CPW resonator with the grounded center conductor and the lateral ground planes. b) Cross section of the CPW resonator. Here, the width w of the center conductor and the gap size s are specified. The isolating substrate layer consist of sapphire and the metallization layer is made of niobium [31]. c) The lumped element LC-resonator which models the zero-losses CPW resonator.

A total quality factor Q can be defined for the coupled resonator as a combination of the internal and external quality factors. This total quality factor can be directly measured in a resonator transmission measurement. The spectrum of the transmitted power shows a Lorentzian line shape with full-width at half-maximum $\kappa/2\pi$:

$$\text{P}(\omega) = \frac{\text{IL } P_{\text{in}}}{1 + (\frac{\omega - \omega_r}{\kappa/2})^2} \tag{3.2}$$

and is related to the quality factor through:

$$\text{Q} = \frac{w_r}{\kappa} \tag{3.3}$$

P_{in} is the drive power at the resonator input and IL is given by the insertion loss of the resonator. The photon storage time is inverse proportional to κ and therefore, a small κ can be used to store photons in a resonator, where a high κ is useful for a fast readout [31]. Further,

the number of photons inside the resonator is directly proportional to the applied drive power and can be measured by coupling a qubit to the resonator (for details see Section 3.23). κ also specifies the possibility to optimize the qubit readout, especially for multi-qubit systems (see Section 3.4 for details).

At the end of this section, the zero-losses CPW resonator will be quantized. Therefore, it is described as an LC circuit model with resonance frequency ω_r, which can be quantum mechanically treated as an harmonic oscillator [10]:

$$ \mathrm{H} = \frac{\hat{\phi}}{2L} + \frac{\hat{q}}{2C} = \hbar\omega_r \left(\hat{a}^\dagger\hat{a} + \frac{1}{2}\right) \tag{3.4} $$

Here $\hat{\phi}$, $\hat{q}$ are the conjugate variables corresponding to $\hat{x}$, $\hat{p}$ and fulfilling the commutator relation $[\hat{q}, \hat{\phi}] = i\hbar$. $\hat{a}$ and $\hat{a}^\dagger$ represent the bosonic annihilation and creation operator that rises or lowers the number of photons in the resonator, respectively. Their commutator relation holds $[\hat{a}, \hat{a}^\dagger] = 1$.
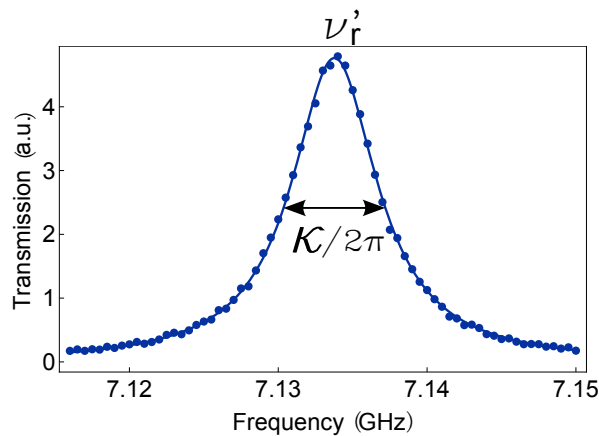
Figure 3.2: The transmission power spectrum of a resonator spectroscopy is shown. The data is fitted by a Lorentzian curve. Typical output powers are on the order of 10^{-18}W corresponding to a situation where a single photon is on average in the resonator. To detect such weak signals one uses low-noise amplifiers and a lock-in technique that allows to improve the signal-to-noise ratio by averaging over many repetitions of the experiment.

3.2 Superconducting qubits

So far, a linear oscillator is described, leading to a equal level splitting in energy. However, intrinsic for a two-level system is the requirement, that two stats can be distinguished from all other states of the system. For this purpose, a nonlinear element has to be added in the circuit which introduces an anharmonicity between the different energy levels. Therefore, the Josephson junction seems predestined as a dissipation-free device with a nonlinear inductance [18].

3.2.1 The Josephson junction

The Josephson junction is built out of two superconductors which are separated by an insulating layer. Cooper pairs can tunnel coherently through this barrier and hence, a super-current I flows between the superconductors. Josephson showed that the supercurrent I and

voltage V depend on the phase difference $\Delta\phi(t)$ between the phases of the two superconducting leads:

$$V(t) = \Phi_0 \, \partial_t \Delta\phi(t)$$
$$I(t) = I_c \, \sin(\Delta\phi(t)) \tag{3.5}$$

$\Phi_0 = \hbar/2e$ is the reduced magnetic flux quantum and I_c is the maximal supercurrent below which no voltage drops across the junction which leads to a dissipation-free device [10]. Invoking Faraday's law ($V = -L\dot{I}$) one can show that the nonlinear inductance of the Josephson junction reads

$$|L_J| = \Phi_0 \sqrt{I_c^2 - I^2} \quad \text{with } I < I_c. \tag{3.6}$$

Furthermore, the junction has an intrinsic capacitance C_J corresponding to a geometric shunting capacitance between the two electrodes which is depicted in Figure 3.3. Therefore, the junction can be seen as an nonlinear oscillator with a resonant angular frequency:

$$\omega_J(I) = \frac{1}{\sqrt{L_J C_J}} = \sqrt{\frac{I_c}{\Phi_0 C_J}} \frac{1}{(1 - I^2/I_c^2)^{\frac{1}{4}}} \tag{3.7}$$

This kind of oscillation is described by an effective particle of mass $\Phi_0 C_J$ moving along the $\Delta\phi$ axis in an tilted washboard potential:

$$U(\Delta\phi) = E_J(1 - \cos(\Delta\phi) - \Phi_0 I \Delta\phi \tag{3.8}$$

where $E_J = I_c \Phi_0$ is the Josephson coupling energy. For I = 0 the potential is sinusoidal and can be approximated around a minimum by a harmonic oscillator potential resulting in an oscillation with $\omega_J(I = 0)$ around a minimum of the potential. Applying a bias current, the potential is tilted and if I becomes equal or larger than I_c the particle runs down the potential and a voltage drop occurs across the junction. Through the slight anharmonicity of the potential the spacing between the energy levels decreases with increasing quantum number and therefore, each transition has a different frequency [18].
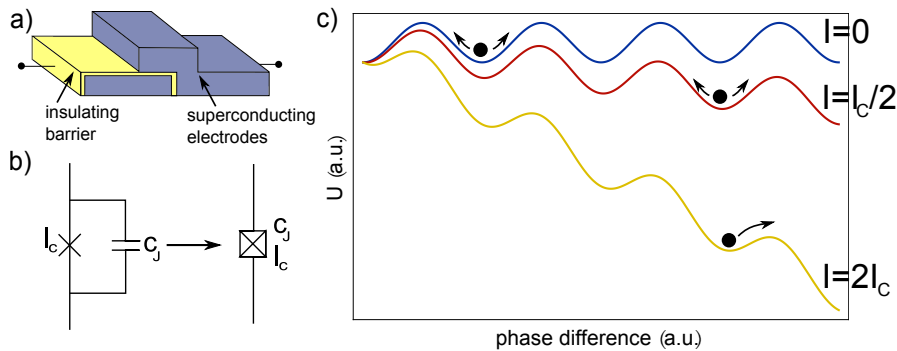
Figure 3.3: a) A schematic representation of the Josephson junction where the two superconductors are separated by an insulating layer [21]. b) The electrical symbol of the Josephson junction as a combination of junction denoted by X and the intrinsic capacitance C_J. c) Illustration of the washboard potential. For $I < I_C$ the effective particle representing the Josephson junction is trapped in a potential well and oscillates around the minimum, whereas it runs down the washboard for $I > I_C$ [18].

3.2.2 The Cooper Pair Box

The Josephson junction can be biased with a voltage V_g. The corresponding circuit is shown in Figure 3.4a where a voltage source is coupled via a gate capacitance C_g to one of the superconductors of the Josephson junction, the superconducting island. The second superconductor is grounded and serves as a reservoir of the Cooper pairs. This circuit is called Cooper pair box (CPB) [14]. Besides the coupling energy E_J the charging energy $E_C = \frac{e^2}{2(C_g+C_J)}$ is of relevance in the CPB defining the energy needed to transfer a single electron from one electrode to the other [5].

Figure 3.4: The Cooper pair box: a) A sketch of the CPB which is biased by an external voltage and the corresponding electrical circuit are depicted. b) Schematic of a SQUID loop in which the Josephson energy can be tuned with a magnetic field [21].

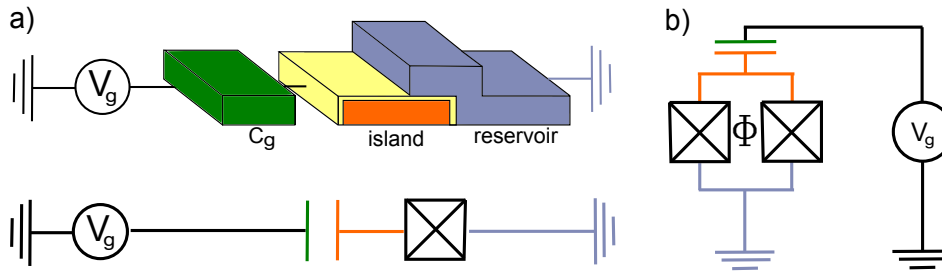In the limit $E_C \gg E_J$ the additional number of Cooper pairs in comparison to the neutral state on one of the superconducting islands can be well defined and the Hamiltonian of the CPB reads

$$H = 4E_C(\hat{n} - n_g)^2 - E_J \cos(\hat{\Delta\phi}) \tag{3.9}$$

where $\hat{n}$ is the number operator defining the number of Cooper pairs on the island and $\hat{\Delta\phi}$ is the conjugated phase operator. $n_g = C_g V_g/2e$ corresponds to the charge of the gate capacitor in units of 2e and can be tuned via the gate voltage.

Rewriting the CPB Hamiltonian in the charge representation where the eigenstates $|n\rangle$ of the number operator $\hat{n}$ form a complete basis, one obtains [58]

$$H = \sum_n \left[4E_C(n - n_g)^2 |n\rangle \langle n| - \frac{1}{2} E_J(|n\rangle \langle n+1| + |n+1\rangle \langle n|) \right]. \tag{3.10}$$

For $E_J = 0$ a quadratic dependence of the energy level on n_g for a fixed number of Cooper pairs is given. These parabolas cross for n_g being integer or half-integer resulting in an energy degeneration of the corresponding charge states (see Figure 3.5a). For a finite Josephson energy this degeneracy is lifted, leading to an avoided level crossing (see Figure 3.5b). For example, at the point $n_g = 1/2$ only the $n = 0$ and $n = 1$ state are of importance which is considered in more detail in the following.

The two new eigenstates at this degeneracy point are $|\pm\rangle = (|0\rangle \pm |1\rangle)/\sqrt{2}$ and are separated by E_J. All other states are much higher in energy and therefore can be neglected. Hence, an effective two-level system is realized for which the Hamiltonian in the computational basis $|0\rangle_C = |-\rangle$, $|1\rangle_C = |+\rangle$ reduces to

$$H = \frac{E_{01}}{2} \hat{\sigma}_z. \tag{3.11}$$

$E_{01} = \hbar\omega_{01}$ is the transition energy between the $|0\rangle_C$ and $|1\rangle_C$ state. For $n_g = 1/2$ it is equal to E_J. An expansion of this model in an area $0 \ll n_g \ll 1$ is detailed in the article of Makhlin [58].

Up to this point an implementation of a two-level system in a superconducting circuit has been shown with the charging energy as one tunable parameter, corresponding to a rotation of one axis of the Bloch sphere. In order to perform arbitrary single-qubit operations at least rotations around two axes of the Bloch sphere have to be accessible. Therefore, also E_J has to become controllable. In order to do this, the single Josephson junction is replaced by a pair of parallel junctions forming a superconducting quantum interference device (SQUID). It can be biased by an external magnetic flux Φ through an inductor loop and therefore, E_J becomes Φ dependent

$$E_J(\Phi) = 2E_J^0 \cos(\frac{\pi\Phi}{\Phi_0}). \tag{3.12}$$

Equation 3.12 holds, if both junctions have the same $E_J = E_J^0$. Furthermore, the form of the CPB-Hamiltonian is retained with an effective Josephson coupling $E_J(\Phi)$.

Qubit transitions between $|0\rangle_C$ and $|1\rangle_C$ around a second axis can be driven by adding a time dependent voltage term $V(t) = V_d \cos(\omega_d t)$ to the constant gate voltage V_g^{DC}. $V(t)$ oscillates at frequency ω_d close to the qubit transition frequency ω_{01}. Inserting this term in Equation 3.9 for $n_g = 1/2$ and restricting the system to two states, one ends up with the driven two-level Hamiltonian [5]:

$$H \approx \frac{E_{01}}{2}\hat{\sigma}_z + \Omega \cos(\omega_d t)\hat{\sigma}_x \tag{3.13}$$

where $\Omega \propto E_C V_d$ is the Rabi frequency of the drive. Therefore, the two field components $\hat{\sigma}_x, \hat{\sigma}_z$ are controllable which allows arbitrary single-qubit operations.
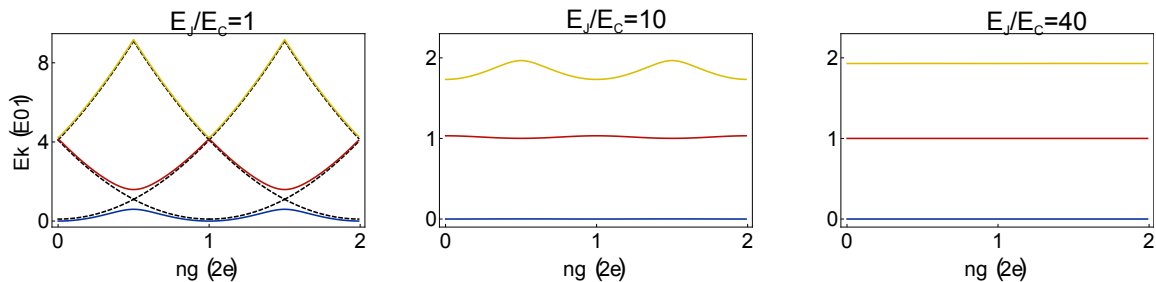
Figure 3.5: Eigenenergies $E_k(n_g)$ of the Hamiltonian 3.10. The first three levels for different E_J/E_C ratios are plotted in units of E_{01} at the degeneracy point $n_g = 1/2$ as a function of n_g. The dashed lines in the left figure show the case for which $E_J/E_C = 0$ where the different levels cross. For a finite ratio an avoided crossing at the degeneracy points occurs which results in separated energy bands. These bands flatten with increasing ratio of E_J/E_C exponentially while the anharmonicity decreases in a low power law for a transmon qubit design (see Section 3.2.3). The ratio $E_J/E_C = 40$ corresponds approximately to the experimental situation. [49]

3.2.3 The Transmon

Cooper pair box qubits have two main quantities: its anharmonicity α and its charge dispersion of the energy levels (see Figure 3.5). The anharmonicity characterizes the goodness of the two-level approximation and is given by:

$$\hbar\alpha = E_{12} - E_{01} \tag{3.14}$$

The charge dispersion defines the variation of the energy levels in relation to environmental offset charge and gate voltage and hence, describes the sensitivity to charge noise. A reduced charge dispersion results in a qubit which is more insensitive to charge fluctuations. This is achieved by increasing the ratio of E_J/E_C. However, a higher E_J/E_C ratio decreases the anharmonicity of the qubit making excitations of higher transitions in the system more probable or extending the time needed to carry out quantum operations due to the fact that a more precise defined frequency spectrum results in longer operation time. One approach to handle this problem, is to operate Cooper pair box qubits at the $n_g = 0.5$ point where a relative flat charge dispersion and a good anharmonicity is given for small E_J/E_C ratios.

In the experiments qubits with a different design are used: the transmon qubits. In this type of qubits the SQUID loop is shunted via a large capacitance C_S, while similarly the gate capacitance C_g is scaled (see Figure 3.6). The advantage of this type of qubit is that the charge dispersion decreases exponentially with E_J/E_C, while the anharmonicity decreases algebraically with a low power law in E_J/E_C. Consequently, the CPB can be made independent of the gate charge and operated at much higher E_J/E_C ratios - the so called transmon regime where $E_J \gg E_C$. Therefore, the transmon becomes nearly insensitive to charge fluctuations, accompanied only by a small loss of anharmonicity (see Figure 3.5). Furthermore, Koch et al. [49] have shown that the effective Hamiltonian has the same form as for the CPB qubit in Equation 3.9.

Typical energy values for $E_C/\hbar$ and $E_J/\hbar$ of transmons qubits are 200-400 MHz and 10-30 GHz, respectively and its anharmonicity can be approximated by:

$$\hbar\alpha \approx -E_C \tag{3.15}$$
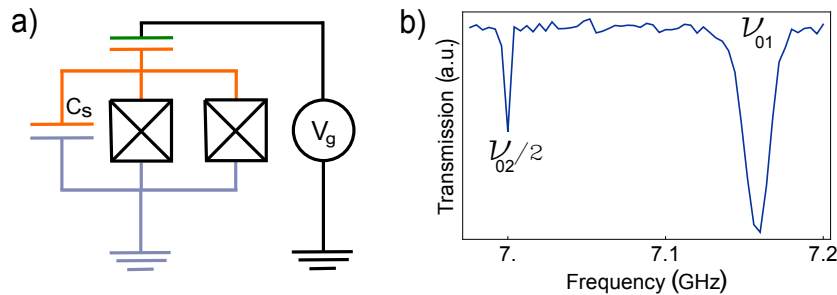

Figure 3.6: a) The electrical circuit representation of the transmon qubit where the SQUID loop is shunted by an large capacitance C_S. b) Experimental data of a quit spectroscopy where the $\nu_{01} = \omega_{01}/2\pi$ transition is driven. Additionally, the $\nu_{02}/2$ transition is visible through a two photon process at a frequency $\alpha/2 = \nu_{02}/2 - \nu_{01}$ below ν_{01}.

3.3 Coupling a Transmon to a resonator

So far, the transmission line resonator and the transmon qubit have been introduced independently from each other. Combining this two elements brings several new and deeply interesting physical properties - the field of circuit QED where e.g. cavity QED experiments can be performed in superconducting circuits. The resonator can be used to control and read out the qubit state as well as can be mediated a qubit-qubit interactions.

3.3.1 Generalized Jaynes-Cummings-model

Placing a transmon at the center of a CPW resonator couples it to the second resonator mode which has its voltage antinode at the center of the resonator. This is depicted in Figure 3.7. The quantization of this circuit leads to an effective Hamiltonian in the realistic limit where $C_r \gg (C_g + C_J)$:

$$
\begin{aligned}
H &= H_{\text{transmon}} + H_{\text{resonator}} + H_{\text{coupling}} = \\
&= 4E_C(\hat{n} - n_g)^2 - E_J \cos(\hat{\Delta\phi}) + \hbar\omega_r \hat{a}^\dagger \hat{a} + 2\beta e V_{rms}^0 \hat{n}(\hat{a}^\dagger + \hat{a})
\end{aligned}
\tag{3.16}
$$

The prefactor of the coupling term is given by $V_{rms}^0 = \sqrt{\hbar\omega_r/2C_r}$ which is the root-mean-square voltage of the local oscillator and the parameter $\beta = C_g/(C_g + C_J)$ and only one mode ω_r of the resonator is considered. The next step to simplify this Hamiltonian is to rewrite it in the basis of uncoupled transmon states $|i\rangle$

$$
H = \hbar\sum_j \omega_j |j\rangle\langle j| + \hbar\omega_r \hat{a}^\dagger \hat{a} + \hbar\sum_i g_{i,j} |i\rangle\langle j| (\hat{a}^\dagger + \hat{a})
\tag{3.17}
$$

where g_{ij} is the coupling energy. In the transmon limit g_{ij} can be restricted to nearest-neighbor coupling $g_{i,i+1}$. Further, the rotating wave approximation is employed to avoid non-energy conserving terms which describe simultaneous excitations or deexcitations of the qubit and the resonator. Therefore, one ends up with the generalized Jaynes-Cummings-Hamiltonian [49]

$$
H = \hbar\sum_j \omega_j |j\rangle\langle j| + \hbar\omega_r \hat{a}^\dagger \hat{a} + \hbar\sum_i g_{i,i+1} |i\rangle\langle i+1| \hat{a}^\dagger + h.c.
\tag{3.18}
$$

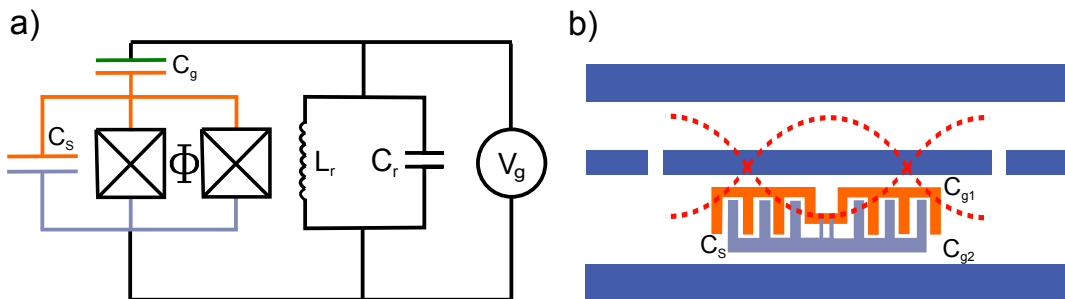where $\hbar g_{i,i+1} \propto \beta(E_J/E_C)^{1/4}$.

Figure 3.7: Coupled System of a transmon qubit and a CPW resonator in an effective circuit diagram and a schematic. Therefore, all previous introduced elements are combined. [49]

Emphasizing that $g_{i,i+1}$ increases together with E_J/E_C allowing to operate the transmon in the strong coupling regime [81]. In this regime g is much larger than the decay rate of the photon inside the resonator κ and of the qubit state γ:

$$g \gg \kappa, \gamma \tag{3.19}$$

Therefore, single quantum excitation can be exchanged between the qubit and resonator resulting in a hybridized entangled system, if $\omega_r = \omega_{01}$, like the hybridization in the orbitals of molecules. This was, for example, shown by Fink et al. [30] by examining vacuum Rabi mode splitting in a circuit QED system.

Note, that g can be engineered in this system, by designing the geometry of the device to control β or by tuning the external magnetic flux and thereby vary E_J.

Additional, in this regime the transmon can be utilized as an actual qubit, because coherent control and readout of the qubit can be performed on much shorter time scales than the excited state decays. Therefore, the transmon is operated in the dispersive limit where the detunings $\Delta_i = \omega_{i,i+1} - w_r$ between the transmon and the cavity are large [5].

3.3.2 The dispersive regime

In the dispersive limit the relation $|\Delta_i| \gg g_{01}$ holds especially for the detunings $|\Delta_0|$ and $|\Delta_1|$. Thus, no direct excitations are exchanged between the transmon and the resonator, but they still influence each other. The effective Hamiltonian can be written in the two-level approximation as:

$$H = \frac{\hbar}{2}(\omega_{01} + \chi_{01})\hat{\sigma}_z + (\hbar(\omega_r + \frac{\chi_{01}}{2}) + \hbar\chi\hat{\sigma}_z)\hat{a}^\dagger\hat{a} \tag{3.20}$$

As one can see, this effective Hamiltonian is of the same form as the Jaynes-Cummings-Hamiltonian with a renormalized resonator frequency $\omega_r' = \omega_r + \chi_{12}/2$ and a qubit frequency $\omega_{01}' = \omega_{01} + \chi_{01}$ which is renormalized by a Lamb shift term χ_{01}. In this limit, the dispersive shift $\chi_{i,i+1}$ describes the coupling between the resonator and the qubit and is given by

$$\chi_{i,i+1} = \frac{g_{i,i+1}^2}{\Delta_i}. \tag{3.21}$$

In a CPB qubit χ is equal to χ_{01} as a result of symmetric level repulsion, but for the transmon due to its pairwise level repulsion χ is expressed by [49]:

$$\chi = \chi_{01} - \chi_{12}/2 \approx \frac{g^2 E_C}{\Delta_0(\Delta_0 - E_C)} \tag{3.22}$$

It is always negative for detunings $\Delta < 0$ which is the case for all experiments performed during this thesis. The interesting point in Equation 3.20 is that $\hbar\omega_r' + \hbar\chi\hat{\sigma}_z$ corresponds to a state dependent shift of the resonator frequency and hence can be used to read out the qubit state by measuring the amplitude and phase or the in-phase and quadrature components I and Q of the transmitted field $E = I\cos(\omega t) + Q\sin(\omega t)$ [9]. If the qubit is in the ground state $|0\rangle$, the resonance frequency is shifted to $\omega_r' - \chi$, whereas it is $\omega_r' + \chi$ for the qubit being in the excited state $|1\rangle$. This feature is illustrated in Figure 3.8.
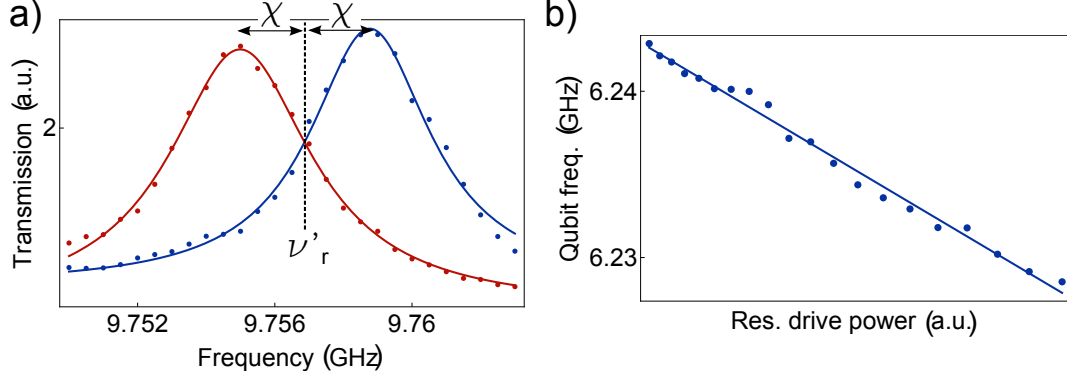
Figure 3.8: a) Measured transmission power in the resonator spectroscopy for a single qubit being in the $|0\rangle$ or $|1\rangle$ state, respectively. ν'_r corresponds to the renormalized resonator frequency $\omega'_r/2\pi$ which is shifted dependent on the qubit state by $\pm\chi$. The data is fitted in each case with a Lorentzian curve. b) AC stark shift of the qubit frequency ω_{01}. It decreases linearly with increasing number of photons in the resonator which is proportional to the drive power.

A further effect due to the virtual interaction between the qubit and resonator can be explained by rewriting the Hamiltonian 3.20 as

$$H = \frac{\hbar}{2}(\omega'_{01} + 2\chi\hat{a}^\dagger\hat{a})\hat{\sigma}_z + \hbar\omega'_r\hat{a}^\dagger\hat{a}. \tag{3.23}$$

Therefore, the AC Stark shift of the qubit frequency which depends on the number of photons in the resonator is easily visible. The qubit frequency is shifted by 2χ for each photon in the resonator and thus the resonator drive power corresponding to one photon P_{one} can be extracted. An AC Stark measurement is shown in Figure 3.8b where a P_{one} of -10 dBm is obtained.

The dispersive readout can also be used to perform a Quantum-Non-Demolition (QND) measurement. QND means that the interaction term in the Hamiltonian which couples the system and the measuring apparatus commutes with measured quantity. The measurement leaves the measured state not totally unchanged, but it is repeatable and therefore, one can overcome detection inefficiencies [35]. It is achieved by using a weak coherent drive with amplitude $\epsilon(t)$ which is given in a frame rotating at the measurement frequency ω_m by [12]:

$$H_{drive} = \hbar\epsilon(t)(\hat{a}^\dagger + \hat{a}) \tag{3.24}$$

3.4 Analytical considerations of the joined two-qubit readout

The dispersive model can be generalized to multi-qubit systems for a joint readout. If two qubits are coupled to the same resonator, the resonance frequency is renormalized by both qubits $\omega'_r = \omega_r - (\chi^A_{12} + \chi^B_{12})/2$ as well as a Lamb shift which occurs for each of them. The relevant parts of the dispersive Hamiltonian for the readout of the two qubit states are given by

$$H = \hbar(\Delta_{rm} + \chi^A\hat{\sigma}^A_z + \chi^B\hat{\sigma}^B_z)\hat{a}^\dagger\hat{a} + \frac{\hbar}{2}\sum_{q=A,B}(\omega^q_{01} + \chi^q)\hat{\sigma}^q_z + H_{drive}. \tag{3.25}$$

where $\Delta_{rm} = \omega'_r - \omega_m$ is the detuning of the measurement frequency from the renormalized resonator frequency and the subscripts A, B label the two qubits [11].

The measurement result of the field quadratures

$$
\begin{aligned}
\langle \hat{I}(t) \rangle &= Tr[\hat{\rho}(t)(\hat{a}^\dagger + \hat{a})] = Tr_q[\hat{\rho}_q(0)\hat{M}_I(t)] \\
\langle \hat{Q}(t) \rangle &= iTr[\hat{\rho}(t)(\hat{a}^\dagger - \hat{a})] = Tr_q[\hat{\rho}_q(0)\hat{M}_Q(t)]
\end{aligned}
\tag{3.26}
$$

can be analytically calculated for an infinite qubit lifetime. Here, $\hat{\rho}(t)$ denotes the full density matrix of the coupled qubit-resonator system and $\hat{\rho}_q(0)$ the density matrix of the qubits at the initial time. Tr_q labels the partial trace over both qubits and $\hat{M}^{I,Q}(t)$ the measurement operators for I and Q with the coherent state amplitude $\alpha_{ij}(t)$ which depends on the qubit state $|ij\rangle$ ($i, j \in \{0,1\}$). The measurement operators are given by:

$$
\begin{aligned}
\hat{M}^{I,Q}(t) &= \sum_{i,j} \langle \alpha_{ij}(t)|\hat{I}, \hat{Q}|\alpha_{ij}(t)\rangle |ij\rangle \langle ij| = \\
&= M_{00}^{I,Q} |00\rangle \langle 00| + M_{01}^{I,Q} |01\rangle \langle 01| + M_{10}^{I,Q} |10\rangle \langle 10| + M_{11}^{I,Q} |11\rangle \langle 11|
\end{aligned}
\tag{3.27}
$$

and $\alpha_{ij}(t)$ satisfies

$$
\partial_t \alpha_{ij} = -i(\Delta_{\mathrm{rm}} + \langle ij|(\chi^A \hat{\sigma}_z^A + \chi^B \hat{\sigma}_z^B)|ij\rangle)\alpha_{ij} - i\epsilon(t) - \frac{\kappa \alpha_{ij}}{2}.
\tag{3.28}
$$

This describes the time dependance of the coherent state amplitude for different qubits states in the input-output theory [37]. In the steady state $M_{ij}^{I,Q}$ can be calculated

$$
\begin{aligned}
M_{ij}^I &= \frac{-2\epsilon(t)(\Delta_{\mathrm{rm}} + (-1)^i\chi^A + (-1)^j\chi^B)}{(\kappa/2)^2 + (\Delta_{\mathrm{rm}} + (-1)^i\chi^A + (-1)^j\chi^B)^2} \\
M_{ij}^Q &= \frac{-\epsilon(t)\kappa}{(\kappa/2)^2 + (\Delta_{\mathrm{rm}} + (-1)^i\chi^A + (-1)^j\chi^B)^2}
\end{aligned}
\tag{3.29}
$$

Furthermore, $M^{I,Q}$ are nonlinear functions of $\chi^A\chi^B$ and therefore, containing two-qubit correlation terms. This can be used to reconstruct the full two-qubit state by state tomography measurements [29].

To improve the simultaneous readout of all four two-qubit states in a single-shot measurement (see also Section 3.6) both quadratures I and Q can be analyzed. The best readout fidelity of all four states can be achieved in a square formation of the states in the I-Q plane where the sides should be of maximal length. The measurement operator $M_{ij}^{I,Q}$ in the steady state depends on Δ_{rm}, $\chi^{A,B}$, ϵ and κ. The drive amplitude $\epsilon(t)$ can be seen as a scaling factor which defines on one hand, how fast the steady state is reached which is seen in the non-steady state solution. On the other hand, $\epsilon(t)$ determines how well the four states are separated due to the power of the resonator drive. A further scaling factor is given by the gain of the amplifiers which follow after the resonator. Here especially the Josephson parametric amplifier has to be mentioned which is described in Section 3.8. The magnitude of the resonator drive power is limited by the QND assumption of a weak coherent field where a critical number of photons in the resonator can be defined by [12]:

$$
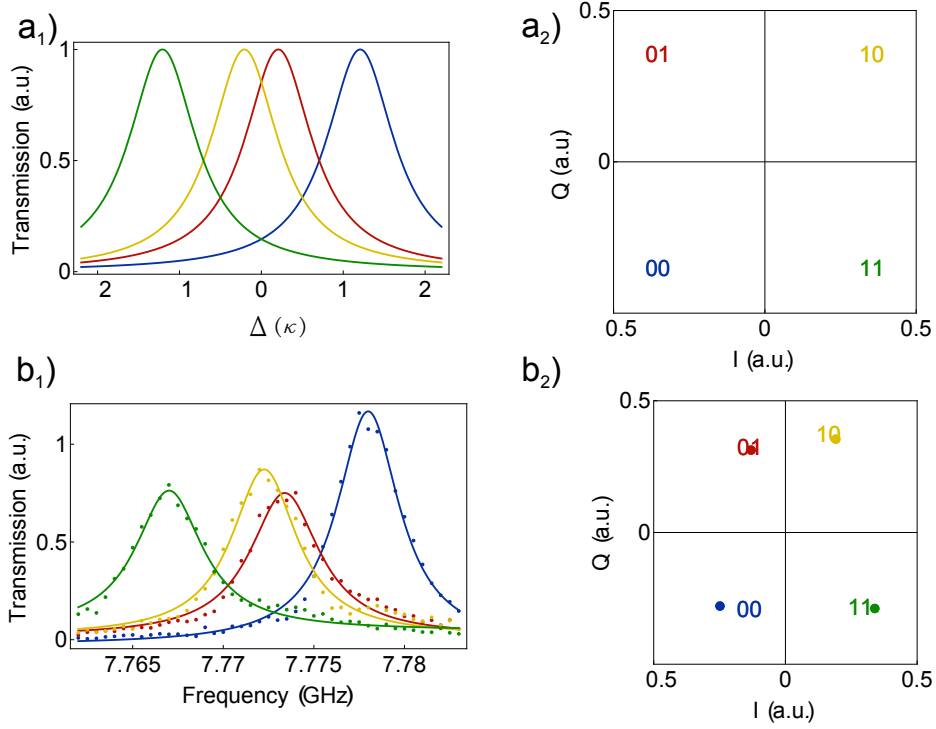n_{\mathrm{crit}} = (\frac{\Delta_0}{2g})^2.
\tag{3.30}
$$

Figure 3.9: a_1) The calculated power spectrum of the optimal configuration to distinguish the four two-qubit states in the I-Q plane is shown. Therefore, a $\chi\kappa^A = -1/\sqrt{2}$, $\chi\kappa^B = -1/2$ is required. a_2) The I-Q plane for these optimal $\chi\kappa^{A,B}$ is depicted where a square formation of the four states is visible. An offset in the Q-quadrature is chosen so that the points are located symmetrically around 0. b_1) Transmission power spectroscopy measurement dependent on the four possible states. A $\chi\kappa^A = -0.88$ and a $\chi\kappa^B = -0.79$ ratio is obtained from this measurement where a integration time of 200 ns is required to extracted κ with a high accuracy. b_2) The I-Q plane representation is depicted. The numbers define the simulated positions, whereas the dots are the measured data points (here for an integration time 150 ns is chosen to reduce the effects of the decay, but still be kept approximately in the steady state limit). For the simulation, a scaling factor, Δ and the offsets in I, Q are adapted. In the experiment the $\chi\kappa$s were chosen under the further conditions of high lifetimes $T1_{Qb1,\,Qb2} \approx 4300, 2000$ ns and coherence times $T2^*_{Qb1,\,Qb2} \approx 2900, 1600$ ns of the qubit.

For the derivation of the optimal parameters in the steady state $\epsilon(t)$ is not of relevance, because it cancels out by setting the differences of $M_{ij}^{I,Q}$ equal which is done in Equation 3.31.

The parameters Δ_{rm}, $\chi^{A,B}$ can be written in terms of κ, because they can be varied by tuning the qubit frequency and κ is to a good approximation fixed in the dispersive limit by the resonator design. To get a square formation $\Delta\kappa = \Delta_{\mathrm{rm}}/\kappa$ and $\chi\kappa^{A,B} = \chi^{A,B}/\kappa$ have to fulfill the following system of equations:

$$
\begin{aligned}
|M_{00}^I - M_{11}^I| &= |M_{00}^Q - M_{01}^Q| \\
|M_{00}^I - M_{11}^I| &= |M_{11}^Q - M_{10}^Q| \\
|M_{00}^I - M_{11}^I| &= |M_{01}^I - M_{01}^I|
\end{aligned}
\tag{3.31}
$$

together with $|M_{00}^I - M_{11}^I| \neq 0$.

The solution of these coupled equations is:

$$\Delta\kappa = 0 \quad \cong \quad \omega_r' = \omega_m$$
$$\chi\kappa^{A\,(B)} = -\frac{1}{\sqrt{2}} \qquad\qquad (3.32)$$
$$\chi\kappa^{B\,(A)} = -\frac{1}{2}.$$

Using Equation 3.22 one can approximately calculate the detuning of the qubit from the resonator Δ_0:

$$\Delta_0^{A,B} = \pm\frac{1}{2}(E_C - \sqrt{E_C^2 - 4\frac{g^2 E_C}{\kappa}\chi\kappa^{A,B}}) \qquad\qquad (3.33)$$

Therefore, the qubit transition frequencies for an optimal two-qubit readout can be determined in the steady state.

Taking the time dependence of the the resonator drive into account, one has to solve the differential Equation 3.28 for a realistic drive amplitude. Assuming a Lorentzian power spectrum of the resonator as presented in Section 3.1 the time evolution of the resonator population is given by the Fourier-transformation of this spectrum and therefore, the resonator drive amplitude is given by

$$\epsilon(t) = \epsilon_0(1 - e^{-\frac{1}{2}\kappa_{in}(t-t_{\text{st}})})\Theta(t - t_{\text{st}}) \qquad\qquad (3.34)$$

where t_{st} defines the beginning of the measurement pulse, ϵ_0 is the steady state amplitude and $\Theta(t)$ the Heaviside step function. The trajectory of the $|00\rangle$, $|01\rangle$, $|10\rangle$, $|11\rangle$ in the I-Q-plane for the optimal $\chi\kappa^{A,\,B}$ and $\Delta\kappa$ are shown in Figure 3.10a. In Figure 3.10b the same experimental data as in Figure 3.9b is plotted. In this case, it is fitted by the non-steady state solution where the measurement time, ϵ_0 and the I and Q offsets are the main fit parameters. $\chi\kappa^{A,\,B}$ and Δ are hold constant to match the steady state fit and are the same as extracted from the resonator measurement. A measurement time t_{meas} where the resonator drive is already at its maximum is extracted, but $\alpha_{ij}(t_{\text{meas}})$ has not reached the steady state. Therefore, the simulated positions agree more exactly with the measurement data as in the steady state fit.

Furthermore, Figure 3.10 illustrates the importance of the timing of the measurement and therefore, also the limitation of the readout fidelity due to a decay of the qubit becomes relevant. If the readout is decay limited, the optimal readout fidelity will be shifted to earlier readout times where the resonator drive has not reached its steady state [35]. In a more complete theoretical derivation the lifetime of both qubits should also be taken into account which would allow a more precise prediction of the measurement results. Furthermore, the spread of the measured data in the form of the signal to noise ratio can be taken into account where also the gain of the amplifiers has to be explicitly specified.

In conclusion in this section the fundamental analytical calculations to predict the position of the four two-qubit states $|00\rangle$, $|01\rangle$, $|10\rangle$, $|11\rangle$ in the I-Q-plane are presented pursuing two main aspects. First, it allows to calculate the required $\Delta_0^{A,B}$ of both qubits for a good separation in the I-Q-plane and second, the theoretical mean values can be compared to the experimental two-qubit single-shot data which is presented in Section 6.1. Furthermore, these theoretical ideas can be considered in the design of future samples to optimize parameters like g, E_C or κ for the readout also in this step.
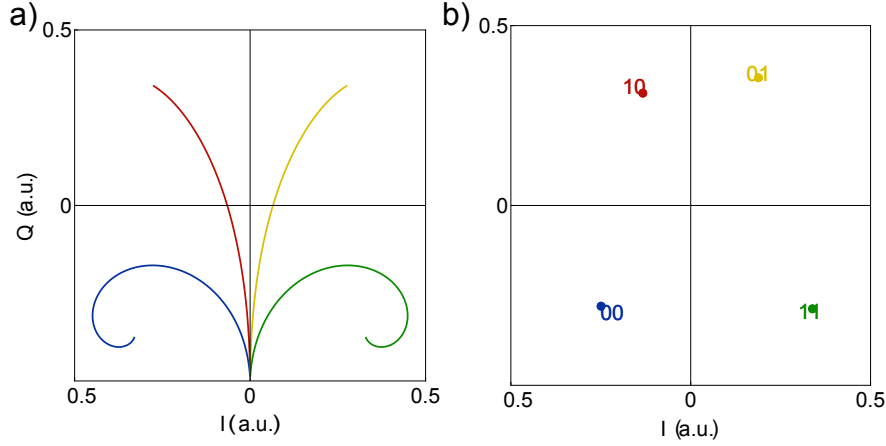
Figure 3.10: a) The time evolution of the four two-qubit states for the optimal $\chi\kappa^{A,\ B}$ and $\Delta\kappa$ in the steady sate solution. Here, the relevance of the readout time for the relative location of the states is visible. b) Plot of the same experimental data as in Figure 3.9b in the I-Q plane. The simulated positions are extracted from a fit with the non-steady state solutions.

3.5 Proposal for the two-qubit readout with two tones

For a further enhancement of the two-qubit readout more measurement tones at different frequencies can be used. Here, a method is described where these two tones are symmetric around $\Delta\kappa = 0$ and the steady state response of the measurement is assumed. Therefore, the readout can be seen as two independent 'single-qubit readouts' for the states $|00\rangle$, $|01\rangle$ and $|10\rangle$, $|11\rangle$ which is depicted in Figure 3.11a. To be distinguishable the two tones have to be down-converted to two different frequencies. Here, the symmetric situation is of advantage because the two tones can be down-converted to $\pm\nu_{d-c}$ which still allows a fast down-conversion on the FPGA (see also Section 4.3).

Again both quadratures of the measurement signal can be explored and the distance between the different states can be maximized to achieve an optimal readout fidelity. For example, with the first tone the contrast between $|00\rangle \leftrightarrow |01\rangle$ in the I-quadrature can be maximized while also the contrast between $|00\rangle , |01\rangle \leftrightarrow |10\rangle , |11\rangle$ can be set to half of its maximum. For the second tone, the same can be done for a permuted order of the states (see Figure 3.11). Under these maximization conditions one can calculate $\Delta\kappa_1$, $\Delta\kappa_2$ and $\chi\kappa$

$$
\begin{aligned}
\Delta\kappa_1 &= +\chi\kappa^{A\,(B)} \\
\Delta\kappa_2 &= -\chi\kappa^{A\,(B)} \\
\chi\kappa^{B\,(A)} &= -\frac{1}{2}
\end{aligned}
\tag{3.35}
$$

where $\chi\kappa^{B\,(A)} = -\frac{1}{2}$ defines the optimal ratio for a single-qubit readout for $\Delta = 0$. In Figure 3.11b all the extracted information is plotted in the I-Q plane showing a square formation. Its sides are increased by a factor of $\sqrt{2}$ compared to one tone measurement. By assuming that the signal to noise ratio stays constant in the one and two tone measurement an increase in the readout fidelity is presented which depends on the standard deviation of the measurement data and therefore, is proportional to the signal-to-noise ratio. This dependence is shown in Figure 3.11c.
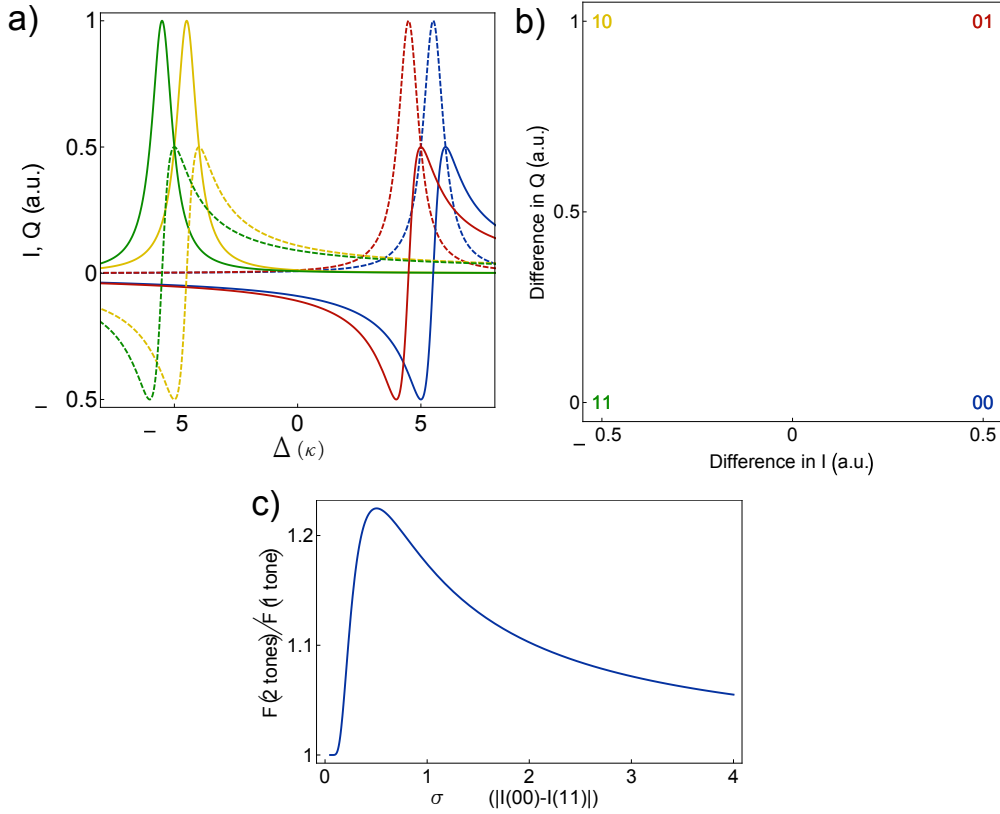
Figure 3.11: a) The I, Q quadrature dependence of Δ is shown for $\Delta\kappa_{1,2} = \pm\chi\kappa^A$ and $\chi\kappa^B = -1/2$. The solid lines illustrate the relevant I and Q curves for a measurement tone at $\Delta\kappa_1 = 5$ and the dashed lines that ones for a tone at $\Delta\kappa_2 = -5$. For example, if one looks at the I quadrature at $\Delta\kappa_1 = 5$, $|00\rangle$ and $|01\rangle$ differ by 1. Furthermore, $|00\rangle$, $|01\rangle$ have a difference of $1/2$ to $|01\rangle$, $|11\rangle$ in the Q quadrature. The reverse statement holds for $\Delta\kappa_2 = -5$. This is equal to an optimal single-qubit readout with one tone. b) To illustrate the difference between the one an two tone method the differences in I and Q are plotted in the I, Q plane as in Figure 3.9. Therefore, an increase of the sides by a factor of $\sqrt{2}$ compared to the one tone method is obtained. c) Comparison of the readout fidelity in the two tones F(2 tones) and one tone F(1 tone) method as a function of the standard deviation $\sigma = \sigma_I = \sigma_Q$. σ is given in units of $|I(00) - I(11)| = |Q(00) - Q(01)|$. For details of the readout fidelity see Section 3.6.

3.6 Single-shot readout in single- and multi-qubit systems

In the previous section, the averaged measurement responses have been discussed, but for the qubit initialization by measurement as well as for the quantum teleportation single-shot readout is necessary. Therefore, the transmon qubits are operated in the dispersive regime and similar measurement techniques are used as for the average readout. An additional low-noise amplification of the measurement signal is required to obtain a high enough signal to noise ratio (SNR). The low-noise amplification is realized by a Josephson parametric amplifier and is explained in detail in Section 3.8. Here, the single-shot fidelities for single and multi-qubit system are derived. Furthermore, the threshold for an optimal qubit state estimation is considered for qubits with a finite lifetime.

First, the single-qubit case shall be considered and then adapted to multi-qubit systems. In experiments the SNR is limited even in the case of an infinite qubit lifetime due to noise added by the amplification of the signal. This is detailed in the description of the setup in Section 4.3. Gambetta et al. [35] theoretically predict that the measured signal I of state $|0\rangle$ and state $|1\rangle$ consists of the actual qubit state plus Gaussian noise:

$$P_{|0\rangle,\,|1\rangle}(I) = \frac{1}{\sigma\sqrt{2\pi}}\, \mathrm{e}^{-(I \mp \langle I\rangle)^2/(2\sigma^2)} \tag{3.36}$$

The readout fidelity is in principle defined as

$$F = 1 - \sum_{i\neq j} P(i|j) \tag{3.37}$$

where the sum is taken over all states and $P(i|j)$ defines the probability that one measures i but the system state was j. This is illustrated in Figure 3.12a where the blue and red filled areas correspond to possible readout errors in the single-qubit case. For a fidelity of 0 no information can be extracted from the measurement where 1 means that the qubit states are perfectly distinguishable. To detect the qubit state in a single measurement a threshold I_{th} is defined. For $I > I_{\mathrm{th}}$ we say that the qubit was initially in state $|0\rangle$ and in state $|1\rangle$ for $I < I_{\mathrm{th}}$. Therefore, the readout fidelity can be written as

$$F = 1 - P(0|1) - P(1|0) = 1 - \int_{-\infty}^{I_{th}} dI P_{|1\rangle}(I) - \int_{I_{th}}^{\infty} dI P_{|0\rangle}(I) = 1 - \sum_{j=-\infty}^{I_{th}} P_{|1\rangle}(I_j) - \sum_{j=I_{th}}^{\infty} P_{|0\rangle}(I_j) \tag{3.38}$$

where sums are used in the discrete case. This can also be expressed in terms of the cumulative probability distribution CP_i as shown in the lower part of Figure 3.12a and the fidelity is the difference between the two curves which is plotted in yellow:

$$F = CP_{|1\rangle} - CP_{|0\rangle} \tag{3.39}$$

This threshold can be shifted from 0 due to an offset in the measurement signal or an finite qubit lifetime. Therefore, the optimal threshold to maximize the readout fidelity is given at the position where

$$P_{|0\rangle}(I_{\mathrm{th}}) \;=\; P_{|1\rangle}(I_{\mathrm{th}}). \tag{3.40}$$

This relation also holds for a finite qubit lifetime T1, where the excited state of the qubit decays at a time t_{decay} to the ground state which is exponentially distributed $P_{|1\rangle}(t_{\mathrm{decay}}) = \exp(-t_{\mathrm{decay}}/T1)$. In principle, two different cases have to be considered. First, if the qubit decays before the measurement starts, no difference is detectable to a qubit initially prepared in the ground state. Therefore, no information can be extracted in the measurement about the original state. The fidelity is hence limited by this decay. This problem occurs in the single-qubit single-shot measurements and is analyzed in Section 5.3. Second, the qubit can decay during the measurement and the excited state probability $P_{|1\rangle}$ becomes non-Gaussian. As Gambetta et al. [35] further pointed out, non-Gaussian terms become relevant for long integration times T_{int}, but for $T1 \gg T_{\mathrm{int}}$ $P_{|1\rangle}$ is still dominated by the Gaussian properties. In
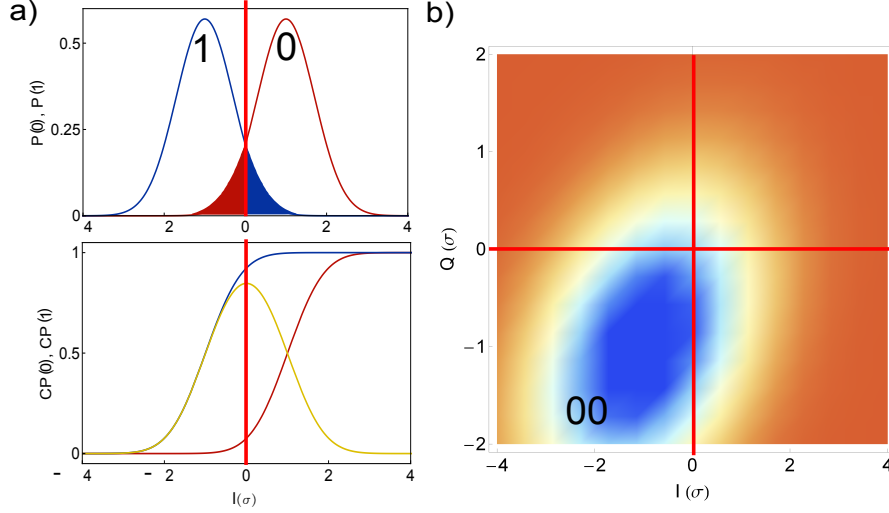
Figure 3.12: a) In the upper plot, the normalized Gaussian distributions of the $|0\rangle$ and $|1\rangle$ state are shown as used in the fit of the single-qubit single-shot experiments. The colored areas mark the readout errors due to an overlap of the distributions and the optimal threshold is marked by the red vertical line. The integral of this distribution results in cumulative probability distributions which are shown in the lower plot and the progress of the readout fidelity is illustrated in yellow. The maximal readout fidelity is found at the optimal threshold. b) To illustrate the two-qubit state readout a density plot of the multivariate normal distribution for the $|00\rangle$ state and the threshold in the I- and Q-quadrature are depicted. The error of the readout is given like in the single-qubit case by integrating the measurement results above the I- or Q-threshold.

the quantum feedback experiments 'short' boxcar filters are required to minimize the effective time delay of the feedback operations and no further integration of the signal is performed in the measurements. Therefore, the excited state is considered as a Gaussian distribution in our experiments. To underline this with numbers we have used a 4 point boxcar filter in the single-qubit readout which results in an ratio $T_{\text{int}}/T1 \approx 40$ ns/1400 ns ≈ 0.03. In the multi-qubit experiments we used an 16 point boxcar filter and hence, find a ratio of $T_{\text{int}}/T1 \approx 160$ ns/2500 ns ≈ 0.06 due to increased qubit lifetimes in this sample.

Moreover, the definition of the readout fidelity as well as the concept to distinguish the qubit states in a single-shot can be expanded to multi-qubit systems. In a two-qubit single-shot readout thresholds in the I- and Q-quadrature have to be defined and hence, the four different states can be dedicated to the four quadrants as shown in Figure 3.12b for the $|00\rangle$ state. For this state the readout fidelity can be calculated as follows

$$F_{00} = 1 - P(01|00) - P(10|00) - P(11|00) =$$

$$1 - \int_{-\infty}^{I_{th}} dI \int_{Q_{th}}^{\infty} dQ P_{|00\rangle}(I,Q) - \int_{I_{th}}^{\infty} dI \int_{Q_{th}}^{\infty} dQ P_{|00\rangle}(I,Q) - \int_{I_{th}}^{\infty} dI \int_{\infty}^{Q_{th}} dQ P_{|00\rangle}(I,Q)$$

(3.41)

where $P_{|00\rangle}(I,Q)$ is the multivariate normal distribution

$$P_{|00\rangle}(I,Q) = \frac{1}{2\pi|\boldsymbol{\sigma}|^{1/2}} \, e^{-\frac{1}{2}((I,Q)-\langle(I,Q)\rangle)^T \boldsymbol{\sigma}^{-1}((I,Q)-\langle(I,Q)\rangle)}$$

(3.42)

with the covariance matrix of I and Q $\boldsymbol{\sigma}$ and their mean value vector $\langle(I,Q)\rangle$.

The total readout fidelity is given by the mean value of the four single readout fidelities:

$$F = \langle F_{00} + F_{01} + F_{10} + F_{11} \rangle \tag{3.43}$$

The formulas which are derived in this section are used in the single- as well as in the multi-qubit experiments. By them the readout fidelities and the optimal threshold for the qubit state estimation as well as feedback or feed-forward operations are extracted out of the measurement results.

3.7 The dispersive J-Coupling and the controlled-phase gate

So far, single-qubit operations and readout have been explained and also the possibility to read out two-qubit states. In this section, moreover the techniques for realizing two-qubit operations will be described whereby the two qubits are dispersively coupled to the same resonator. Principally, two different approaches have to be distinguished. In the first approach a single excitation between the qubits is exchanged via a photon inside the resonator. Therefore, the qubits can stay at their preset frequencies, e.g to maximize the coherence times. The qubit and resonator states are coupled by two-photon sideband transitions which are driven by a strong additional microwave drive fields. The drawback of this method is that the operation takes about 100ns and that it is sensitive to the photon lifetime which is also in the range of 100ns [52].

In the second approach, which is used in the experiments in this thesis, the interaction between the qubits is given by the so called J-coupling by analogy with nuclear magnetic resonance experiments. The qubits are tuned into resonance with each other, but not with the resonator. As a result, an exchange of a single excitation via a virtual photon inside the resonator is achieved. A related effect can be seen in the single-qubit case, where the Lamb shift and AC Stark shift also appear due to this virtual interaction. Here, the qubit-qubit interaction can be implemented on the 10ns time scale where additional flux pulses are required for a fast qubit frequency tuning [28].

The Hamiltonian in the dispersive regime where direct interactions between the resonator and the qubits are neglected consists of three parts:

$$H = H_r + H_q + H_J \tag{3.44}$$

where H_r stands for the dispersively shifted resonator, H_q for the dispersively shifted qubits and H_J for the J-coupling term. This coupling term reads

$$H_{\text{J-coupling}} = \frac{1}{2} \sum_{q \neq q'} \sum_{i,i'=0}^{N-1} J_{ii'}^{qq'} (\ket{i}\bra{i+1}_q \ket{i'+1}\bra{i'}_{q'} + \ket{i+1}\bra{i}_q \ket{i'}\bra{i'+1}_{q'}) \tag{3.45}$$

with

$$J_{ii'}^{qq'} = g_{i,i+1}^q g_{i',i'+1}^{q'} \frac{\Delta_i^q + \Delta_{i'}^{q'}}{2\Delta_i^q \Delta_{i'}^{q'}}. \tag{3.46}$$

The prefactors $J_{ii'}^{qq'}$ is the transition rate between the states $\ket{i}_q \leftrightarrow \ket{i+1}_q$ of one qubit and $\ket{i'}_{q'} \leftrightarrow \ket{i'+1}_{q'}$ of the other qubit, if these transitions are in resonance [5]. However, if a transition is not in resonance $|\omega_{i,i+1}^q - \omega_{i',i'+1}^{q'}| \gg J$, this process is not energy conserving and

no interaction takes place. Thus, the effective coupling strength is controlled by tuning the qubit frequency [57].

The relevant transition to perform a controlled-phase gate which is explained below is $|11\rangle \leftrightarrow |02\rangle$. These two states are coupled by $J_{01}^{AB}(|2\rangle\langle 1|_A |0\rangle\langle 1|_B + |1\rangle\langle 2|_A |1\rangle\langle 0|_B)$ and a detuning between ω_{01}^A and ω_{01}^B of α^A is required. If one of the qubits is tuned in resonance with the $|0\rangle - |2\rangle$ transition of the other qubit, the system oscillates at a frequency $2J_{01}$ between the states $|11\rangle$ and $|02\rangle$

$$|\psi(t)\rangle = \cos(2J_{01}t)|11\rangle + i\sin(2J_{01}t)|02\rangle. \tag{3.47}$$

In our multi-qubits experiments coupling strengths $J_{01}/2\pi$ of 13 and 17 MHz are measured. By waiting a time $t_c = \pi/2J_{01}$ the system ends up in the state $|\psi(t_c)\rangle = -|11\rangle$, while the other three computational states $|00\rangle, |01\rangle, |10\rangle$ do not obtain a phase. Additionally, it has to be considered, that the qubits pick up dynamical phases ϕ^A and ϕ^B due to the frequency tuning and flux crosstalk between the qubits. These additional phases can be compensated by single-qubit rotations around the z axis, so called phase gates. Finally, one ends up with following unitary two-qubit operation

$$\begin{pmatrix} 1 & 0 & 0 & 0 \\ 0 & 1 & 0 & 0 \\ 0 & 0 & 1 & 0 \\ 0 & 0 & 0 & -1 \end{pmatrix} \tag{3.48}$$

which is called the controlled phase (c-phase) gate [77]. By applying a $\pi/2$ $(-\pi/2)$ rotation around the y-axis of qubit A (B) the CNOT gate can be implemented and therefore an arbitrary multi-qubit operation (see Section 2.1).

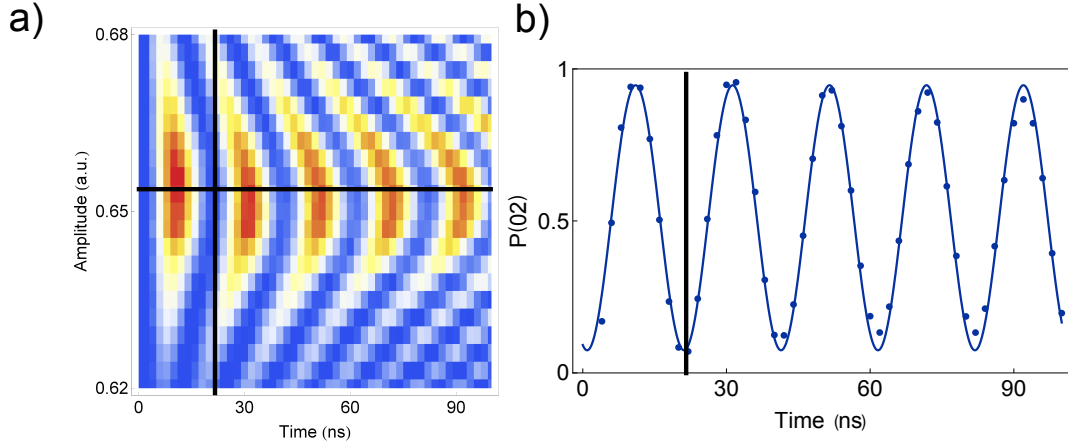Figure 3.13: Calibration measurements of c-phase gate: a) A sweep of the amplitude of the flux pulse versus the length of the pulse. The optimal values are depicted by the black horizontal and vertical lines. b) The single oscillation between the $|11\rangle$ and $|02\rangle$ state is plotted for the optimal amplitude of the flux pulse and the optimal pulse length is marked by the vertical line.

3.8 Parametric amplification

Josephson parametric amplifiers (paramps) are required to achieve high fidelities in the single-shot measurements. The basic idea behind these amplifiers is that the critical current I_C is modulated by an external signal where small changes in I_C can lead to a significantly modified transport property of the system which allows an amplification near the quantum noise limit [79].

One possible realization of these amplifiers is the coupling of an array of SQUID loops to a $\lambda/4$ transmission line resonator forming a nonlinear resonator. The schematic setup is shown in Figure 3.14. Additionally, the system is driven close to its bifurcation point by a large amplitude coherent pump at frequency ω_p [25].
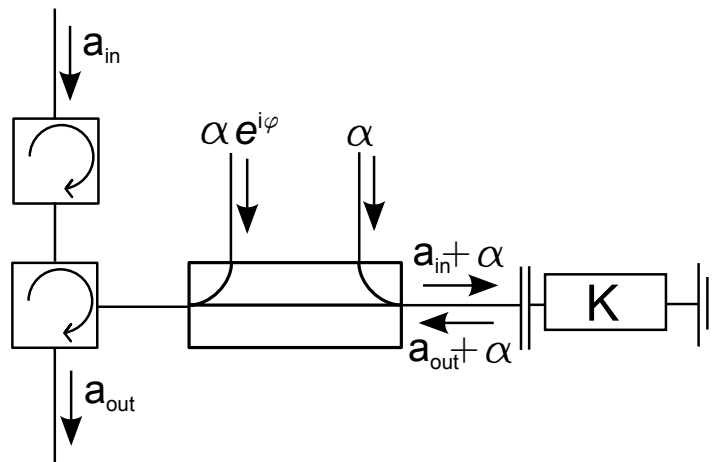
Figure 3.14: The schematic setup of the paramp is depicted. A $\lambda/4$ transmission line resonator with an array of SQUIDs is implemented. A circulator separates the input and output ports of the paramp. The pump tone is added to the input and subtracted from the output by a directional coupler which minimizes the pump leakage into the input and the output port. At the output this prevents the saturation of further amplifiers (e.g. a cold HEMT amplifier) whereas at the input it reduces leakage into the resonator. To reduce this leakage even further additional circulators are used. [43]

Theoretically the paramp can be modeled as a resonator with a Kerr-like non-linearity added to the harmonic oscillator Hamiltonian:

$$H = \hbar\omega_0 a^\dagger a + \frac{\hbar}{2}K a^\dagger a^\dagger a \qquad (3.49)$$

where K is the Kerr constant. K and the resonance frequency ω_0 are proportional to the Josephson coupling energy $E_J(\phi)$ and hence, can be tuned by applying a magnetic flux ϕ. A detailed theoretical derivation of the paramp as a non-linear Kerr medium can be found in the article of Yurke and Buks [85]. Here, the further description is restricted to the parts which are relevant for the experiments. Paramps can be operated in two different regimes called the phase-preserving and phase-sensitive mode which will be explained next.

3.8.1 The phase-preserving mode

In the phase-preserving mode the two quadratures I and Q of the electric field are equally amplified, while the pump is detuned from the signal frequency by $\Delta = \omega_p - \omega_s$ resulting in an upper and lower sideband called signal S and idler Id. For this situation the output field mode can be written as [19]:

$$\hat{a}_{\text{S,out}} = -\sqrt{G_s}\, \hat{a}_{\text{S,in}} - \sqrt{G_s - 1}\, \hat{a}^{\dagger}_{\text{Id,in}} \tag{3.50}$$

with the photon number gain G_s at the signal frequency ω_s. In Clerk et al. [19] it is shown, that this relation between the signal and idler is typical for a quantum limited amplifier which adds minimal noise to the signal.

In addition, the bandwidth of the paramp decreases, if the gain at the signal frequency ω_s is increased. Hence, an important relation is the gain-bandwidth $\sqrt{G_s}D$ product which stays constant. Furthermore, a generalized input-output relation can be defined for a frequency dependent gain g(ω)

$$\hat{a}_{S,out}(\omega) = -g(\omega)\hat{a}_{S,in}(\omega) - \sqrt{g(\omega) - 1}\hat{a}^{\dagger}_{I,in}(\omega) \tag{3.51}$$

g(ω) can be approximated for a large gain at ω_s

$$g(\omega) \propto \frac{\sqrt{G_s}}{1 - i((\omega - \omega_s)/D)}. \tag{3.52}$$
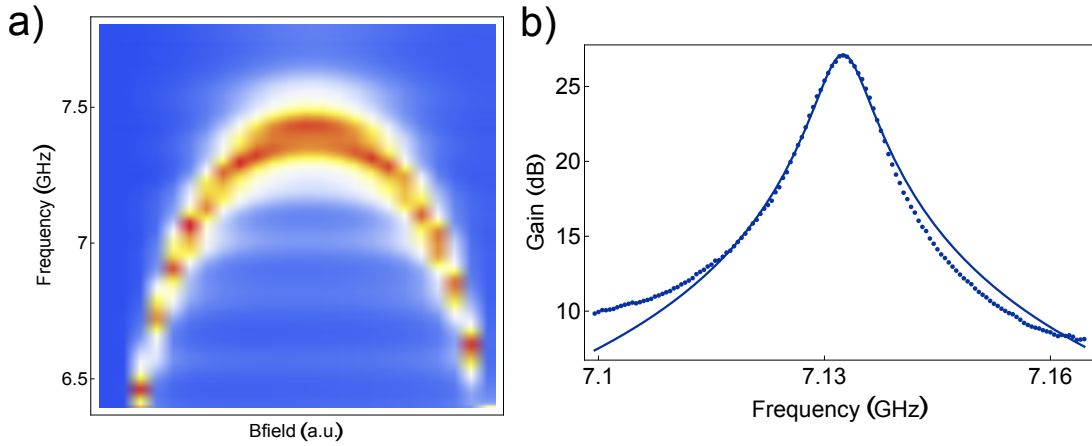
Figure 3.15: a) A sweep of the magnitude of the B-field at the SQUIDS of the paramp to extract the required value for an optimal gain at the resonator frequency. b) A typical paramp gain curve with a nearly Lorentzian line shape which is shown by the fit.

3.8.2 The phase-sensitive mode

In the phase-sensitive mode the signal is exactly at the pump frequency eliminating the idler and converting a single pump photon into two signal photons. In this regime one quadrature of the electric field is amplified, while the other one is attenuated,

$$\hat{I}_{\text{s,out}} = \sqrt{G}\ \hat{I}_{\text{s,in}}$$
$$\hat{Q}_{\text{s,out}} = \hat{Q}_{\text{s,in}}/\sqrt{G}$$

$$(3.53)$$

where G is the gain in power and no extra noise has to be added to preserve the canonical commutation relation:

$$[\hat{I}_S\ ,\ \hat{Q}_S] = i \tag{3.54}$$

The output state is therefore squeezed in the attenuated quadrature. Which quadrature is amplified is defined by the relative phase between the pump and the signal, therefore the paramp becomes phase-sensitive. An optimization procedure to find this phase is explained in Section 5.1.

4 Measurement Setup

In order to operate systems on the single quantum level they have to be well isolated from environmental influences, but at the same time controllable to perform qubit operations. Therefore, circuit QED systems are cooled to temperatures on the order of 20 mK to avoid thermal excitations. Furthermore, they are shielded against high and low frequency electromagnetic noise. The pulses for the qubit control and readout are generated at room temperature and then guided to the circuit QED chip whereby they are attenuated to minimize the thermal noise through these connections.

In this chapter the main aspects of the experimental setup which is required to achieve the aforementioned criteria are discussed. First, the physical implementation of the circuit QED system is described. Second, the dilution refrigerator needed to cool the resonator and the qubits to their ground states shall be introduced shortly in Section 4.2. Next, the signal generation procedure to perform qubit operation and drive the resonator is presented in Section 4.3. Furthermore, the relevant parts of the feedback loop are explained and signal analysis is described. Finally, the FPGA applications to perform feedback are detailed in Section 4.4.

4.1 Sample

The physical realization of the transmission line resonator and the transmon qubit will be explained shortly in this section. The superconducting transmission line resonator is fabricated out of niobium by optical lithography and etching techniques on a mono-crystalline sapphire chip [40]. Typical transmon transitions frequencies are between 4 - 10 GHz. Consequently, the resonator frequencies have to be in this range to operate the system in the dispersive limit. These frequencies correspond to wavelengths of 30 - 80 mm and therefore, a meander form of the resonator is applied to fit on the sapphire chip which is shown in Figure 4.1.

The transmon are manufactured out of aluminum with electron beam lithography, shadow evaporation and oxidation of aluminum. With theses techniques structures in the sub-micron to micron size can be written and Josephson junctions with a tunnel barrier thickness of a few atomic layers can be made. The magnitude of the charging energy E_C and the coupling g can be designed by the geometry of the circuit. The Josephson energy E_J is controllable by the thickness of the tunnel barrier [31]. Furthermore, each qubit is capacitively coupled to an additional transmission line allowing to drive the qubits independently and is called charge gate line [76]. To tune the qubit frequency on short time scales like described in Section 3.7 a further transmission line passes near the SQUID loop such that a current through the line induces a magnetic field through the SQUID loop - the so called flux line [61].

The superconducting chip is placed on a printed circuit board (PCB) which connects the inputs and outputs of the on-chip transmission lines to adapters where microwave cables can be used. This PCB is mounted on a cooper sample holder and superconducting coils are placed on this holder underneath the sample to tune the qubit transition frequency on long time scales. By calibrating the DC voltage applied at these coils one can tune the qubit

frequency independently also on a multi-qubit sample.

The experiments in this thesis were performed on two different samples. The single-qubit experiments were performed on a sample where one transmon qubit is coupled to a CPW resonator. An optical image of the sample and the transmon is shown in Figure 4.1a. The resonator has a resonance frequency $\nu_{\mathrm{res}} \approx 7.135$ GHz and a decay rate $\kappa/2\pi \approx 6.3$ MHz. The charging energy of the qubit is $E_C/h \approx 350$ MHz, and the coupling $g/2\pi \approx 65$ MHz. The transmon was used at two different transition frequencies ν_{01} of 6.146 GHz and 6.514 GHz corresponding to a Josephson coupling energy E_J of approximately 15.0 GHz and 17.0 GHz. Energy relaxation times $T1_{6.146,\ 6.514} \approx (1400,\ 1000)$ ns and the coherence time $T2^*_{6.146,\ 6.514} \approx (280,\ 270)$ ns are detected at this points.

Figure 4.1b illustrates the second sample which consist of three resonators and four qubits whereby only qubit 1 to 3 are used in the experiments. To read out the qubits resonator 1 and 3 are used which have resonance frequencies $\nu_{\mathrm{res1,\ res3}} \approx (7.690,\ 9.720)$ GHz and decay rates $\kappa/2\pi_{\mathrm{res1,\ res3}} \approx (2.6,\ 3.0)$ MHz. For the two-qubit gates, qubit 1 and 2 are coupled through resonator 1 and qubit 2 and 3 through resonator 2 which has a resonance frequency of approximately 8.7 GHz. The qubits have charging energies $E_C/h_{\mathrm{qb1,\ qb2,\ qb3}} \approx (297,\ 303,\ 285)$ MHz and couplings $g/2\pi_{\mathrm{qb1,\ qb2,\ qb3}} \approx (260,\ 180,\ 240)$ MHz. They are operated at transitions frequencies of $\nu_{\mathrm{qb1,\ qb2,\ qb3}} \approx (5.020,\ 6.100,\ 6.720)$ GHz which results in Josephson coupling energies of $E_J^{\mathrm{qb1,\ qb2,\ qb3}} \approx (12.0,\ 17.1,\ 21.5)$ GHz. Energy relaxation times $T1_{\mathrm{qb1,\ qb2,\ qb3}} \approx (2600,\ 2400,\ 2000)$ ns and the coherence time $T2^*_{\mathrm{qb1,\ qb2,\ qb3}} \approx (1100,\ 1400,\ 1200)$ ns are measured at this qubit frequencies.
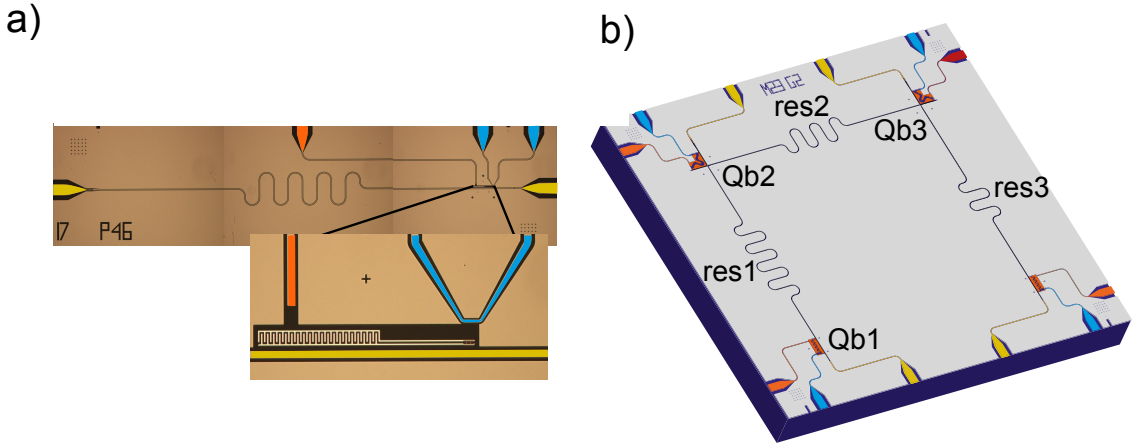
Figure 4.1: a) Optical image of the single-qubit sample at which the state initialization by measurement protocol has been performed. b) Rendering image of the multi-qubit sample which is designed for the implementation of the quantum teleportation algorithm where the required qubits and resonator are labeled. The cross-overs of the resonators are realized by aluminum air-bridges. On both samples the resonators are colored in yellow, the charge lines in orange and the flux lines in blue.

4.2 Dilution refrigerator and wiring

The sample holder is installed in a dilution refrigerator which maximally cools the system down to temperatures of 10 mK. For these temperatures the qubits and the resonator are in their ground states, since the relation $h\nu \gg k_B T$ holds for the typical qubit frequencies. Moreover, the low temperature suppresses quasi-particles excitations in the superconducting

material which would lead to decoherence [40]. The single-qubit experiments were done in a cryogen free VeriCold DR200-10 cryostat and the multi-qubit experiments in a conventional Kelvinox 400HA cryostat form Oxford Instruments. Both of them use a $^3He^4He$ mixture in a closed dilution circuit to reach millikelvin temperatures [83]. The refrigerators have different temperature stages and the sample is located at the base temperature stage. Each of these stages is shielded with a metallic cylinder from thermal excitations and a vacuum is present in all of them to prevent heat transfer from convection [68].

The microwave cables which are connected to the input ports of the sample are fed to the outside via several attenuators at the different temperature stages. Therefore, electrical and thermal noise from the warmer parts is stepwise reduced until a nearly noise free signal reaches the sample. The output port of the sample is first connected to the parametric amplifier where additional circulators are placed in the path to minimize the pump leakage into the resonator by terminating the third port of these. Two more circulators are installed in the output path at the 20mK and 100mK stage to absorb noise from the top. The signal is further amplified at the 1K stage with high electron mobility transistor amplifiers (HEMT) followed by an attenuator to reduce reflection from the top [40].

4.3 Pulse generation and signal analysis

Microwave generators (MWG) like the Agilent E8257 or Rohde-Schwarz SMF100 create coherent signals in the range of approximately 250 kHz to 20 GHz. These generators can be switched on and off through a voltage-gate, but in order to generate short pulses on the nanosecond timescale or pulses of arbitrary shape, arbitrary waveform generators (AWGs) in combination with I-Q mixers are required. Due to the reduced anharmonicity of the transmon, qubit control pulse with a Gaussian envelope with σ of circa 5 ns are used in the experiments to narrow the frequency spectrum. The pulse shape can be further optimized, especially to reduce phase errors of the single-qubit gates by the so called derivative removal by adiabatic gate (DRAG) method [17, 36, 59]. This procedure is employed in the multi-qubit experiments and a detailed description can be found in the PhD thesis of Baur [5].
The Tektronix AWG5014 provides four independent analog waveform channels, eight digital markers and can be operated up to 300 MHz with a maximal sampling rate of 1.2 GS/s. Since the qubit transition frequencies are typical between 4 - 10 GHz, the output signal of the AWG has to be up-converted with an I-Q mixer to the required frequency. The signals of two AWG channels at frequency ω_{IF} and amplitude $A_{IF}(t)$ which are phase shifted by $\pi/2$ are connected to the I, Q inputs of the mixer. A MWG is connected to the LO input port with frequency ω_{LO}. In the mixer the LO input is spitted up into two parts and one of them is phase shifted by $\pi/2$. Next, each of them is multiplied with I or Q ,respectively. Afterwards, both signal are combined and the resulting output signal at the RF port is given by

$$S_{RF} = \frac{A_{LO}A_{IF}(t)}{\sqrt{2}} \cos((\omega_{LO} - \omega_{IF})t + \phi). \tag{4.1}$$

The output signal can be arbitrarily formed in the GHz range by controlling $A_{IF}(t)$. Moreover, the phase ϕ of the output signal is dependent on the phases at the inputs and can therefore, be controlled by adjusting them which is used in Section 5.1 to adapt the paramp pump phase. However, this makes the system vulnerable to phase instabilities which is detailed in Section 5.2.

After the signal has left the cryostat it is analyzed in a heterodyne detection scheme. Therefore, it is band-pass filtered, further amplified and next analog down-converted by an I-Q mixer to 25 MHz. For the down-conversion the RF port and the LO port of the mixer are used as inputs, the I-port as output while the Q-port is blocked. In the next step the signal is amplified a last time and low-pass filtered to suppress high frequency components which also occur in the down-conversion process. This low frequency signal can be digitized in an analog-to-digital converter with sampling rate of 100 MHz and is then digitally down-converted to DC. The 25 MHz frequency of the analog down-conversion is chosen to perform this operation fast on a field programmable gate array (FPGA) [51]. The FPGA also does the further analysis of the signal where in the experiments a Xilinx Virtex 4 is used which is contained in the Nallatech DSP Xtreme Development Kit IV. This FPGA is a general-purpose integrated circuit which can be reprogrammed to implement different applications. FPGAs allow a high bandwidth data processing in a pipelined manner to perform real time data analysis, which is especially interesting for implementing fast feedback operations. To send triggers to or from the FPGA four so called user pins are available.

For the feedback measurements the measurement data is analyzed in real time on the FPGA and dependent on the result a trigger can be given to additional AWGs. To hold the feedback time as short as possible, the feedback pulses are created on Tektronix AWG520s, because they have a time delay from the input of the trigger to the output of the signal at the channels in the order of 38 ns. The overall feedback delay from the time where the data is analyzed until the pulse is detected is measured by driving the resonator through the charge line of the qubit. This measurement is done for the different setups and for different digital filters. Where it has to be considered, that the integration of the measurement data is only performed by the filter in the feedback experiments. In the single-qubit feedback experiments a 4 point boxcar filter is applied to filter out the dc peak which is at -25 MHz after the digital down-conversion. In the VeriCold setup a feedback delay of 240 ns is measured including the data analysis, the pulse generation and all group delays in the path. In the multi-qubit experiments at least a 16 point boxcar filter has to be used to filter out the paramp pump tone at 6.25 MHz. With this filter we detected a total feedback delay of 275 ns and 278 ns for the two different AWG520s in the Oxford setup (see Figure 6.1 for details). For a 40 point filter with arbitrary coefficients a total feedback delay of 850 ns is measured which can be explained by the required time for the multiplication on the FPGA and the increased group delay of the filter. A further point which affects the feedback time is the length of the cables in the feedback loop which therefore, should be kept as short as possible.

In addition, a so called feedback enable trigger is implemented in the experimental setup which is illustrated in Figure 4.2. The AWG can run a sequence of patterns where in each pattern different qubit and measurement pulses as well as triggers can be defined. Therefore, different qubit preparations can be examined in one measurement run. We used this property in the single-qubit experiments to record reference measurements without feedback pulses and feedback measurements in the same measurement run by triggering the FPGA with this feedback enabled trigger. Hence, the feedback trigger is only given, if the feedback enabled trigger is activated in a pattern.

To avoid accumulation of random phases during the measurements all components are phase locked to an external Rubidium 10 MHz reference clock. This is also very important for single-shot measurements to keep the phase of the LO in the down-conversion constant

and hence, the rotation angle of the recorded measurement response in the I-Q plane. Also, in the teleportation scheme the phase stability between the AWGS has to be guaranteed to be able to apply the inverse operation with the feedback pulse.
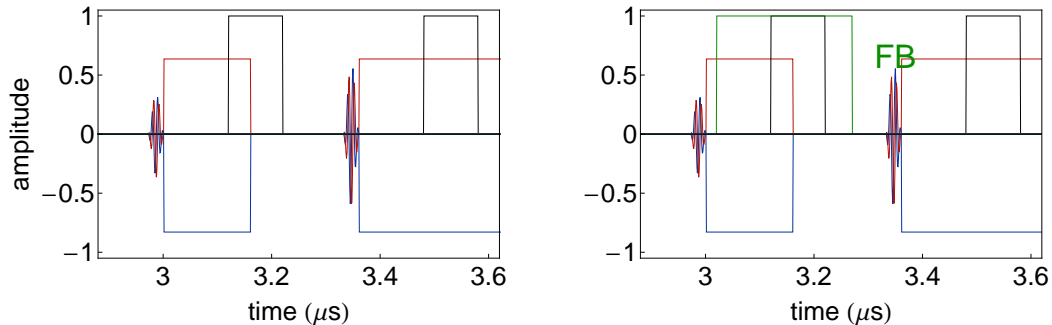

Figure 4.2: A typical sequence of patterns in a single-qubit feedback experiment is depicted. In both patterns the qubit is prepared with a $\pi/2$-pulse followed by a first measurement. Furthermore, a feedback π-pulse is present in both patterns, but is only executed in the second pattern where the feedback enabled trigger (green) is on during the first measurement. The qubit is finally measured a second time to examine the feedback operation. The black triggers are 'shot' triggers which define the start of the recorded data on the FPGA.

4.4 FPGA applications

Two FPGA firmware applications exist to perform feedback experiments. The TvModeV02 application had been developed to record time traces for different pulse sequences. This application adds up the time traces in a cyclic way and the averaged values are saved. Single-shot measurements can be performed by recording independent time traces without averaging. This application is mainly used in the multi-qubit experiments due to the ability to read out the qubit states at many different times. Therefore, it has been adapted to the requirements of the quantum teleportation algorithm. For the two-qubit single-shot readout two thresholds can be set in the I and Q quadrature (see Section 3.4) and four different feedback cases are independently selectable. Furthermore, two independent feedback triggers can be given to provide two different feedback pulses. In addition, two measurements can be recorded simultaneously in this application, which is also necessary to implement the quantum teleportation algorithm.

In order to record the full distribution of the single-shot data two histogram applications exist. The hist2DTVtimeRes application stores data in the form of time resolved quadrature histograms over period of 160 ns for 8 different segments. Furthermore, correlation histograms can be recorded in another mode of this application where two quadratures at two different measurement points are correlated. Two improvements to the version which had been used in the first feedback experiments of Yves Salathé and Thomas Karg [48] shall be mentioned here. First, the delay of the histogram application is equaled with that of the TvModeV02 application. Therefore, the same pulse sequences up to 8 segments can be used in both application and e.g., timing and optimal phase calibrations are valid for both. A specific improvement, for the single-qubit feedback experiments is, that the resolution in the I- quadrature is enhanced in the correlation mode at the expense of the Q-quadrature, because only one quadrature is required for the single-qubit readout.
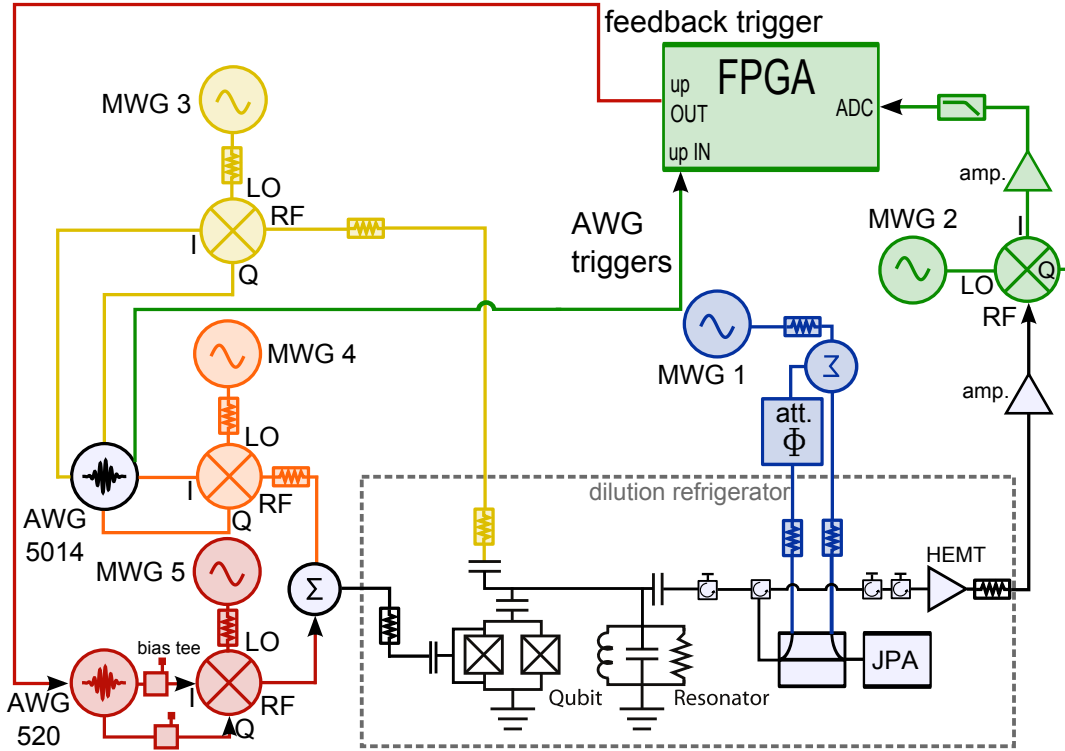
Figure 4.3: Schematic of the setup for single-qubit feedback experiments. The relevant parts for the qubit preparation are colored orange and for the readout in yellow. We switched the measurement pulse with an I-Q mixer to decrease the effective readout time of the qubit state (see also Section 5.3). The paramp pump tone and the displacer are depicted in blue (see Section 5.2). They are required to calibrate the amplification of the paramp as well as the cancellation of the paramp pump at the input and output. The green parts show the signal analysis and in red the feedback components are illustrated resulting in a closed-loop system. The bias tees before the I and Q input of the mixer enable a calibration of the LO leakage through the mixer by applying a DC voltage. Note, that this can be performed directly by the AWG5014. In the multi-qubit experiments the feedback enabled trigger is replaced by a second feedback trigger and two AWG520s are integrated in the setup which is shown on Figure 6.1. Furthermore, components to perform single and multi-qubit operations on three qubits as well as to control two resonators and paramps are set up.

5 Single-qubit feedback experiments

In the area of circuit QED rapid experimental improvements have taken place in the recent years. Reaching the strong coupling limit in 2004 [81] and reading out single qubits in the dispersive regime [29,82] allowed to observe many cavity QED phenomena in superconducting circuits. For example, the violation of a Bell type inequality [1] or the generation of single photon sources [50] have been demonstrated. Furthermore, constantly improving qubit life- and coherence times [49] also made it possible to realize first quantum algorithms like the Deutsch-Josza algorithm [23]. The ability of performing measurement dependent feedback is of great importance to implement more advanced quantum algorithms. Therefore, the essential technical parts and experimental results of single-qubit feedback experiments are described in this chapter.

It starts with a description of the basic calibration steps which are required to perform quantum feedback experiments and to improve the single-shot readout in single-qubit systems. For the single-shot readout the paramp is used in the phase-sensitive mode to achieve maximal amplification in one quadrature. Consequently, the ideal relative phase between the resonator and the pump tone has to be found for which a procedure is described in Section 5.1. During the measurement a phase drift between the MWG which drives the resonator and the one of the paramp pump was noticed and tried to circumvent by splitting the signal of one MWG. Therefore, the technical realization and phase stability tests are presented in Section 5.2. In order to examine the single-shot readout more precisely the transmon qubit has been tuned to two frequencies with different lifetimes and χ/κ ratios. At both points single-shot measurements as well as feedback experiments have been performed. The results are shown and analyzed in Section 5.3. The evaluation of the feedback loop is explained and analyzed in Section 5.4.1. Moreover, the suppression of Rabi oscillations on the basis of feedback operations is shown in Section 5.4.2. Finally, the qubit initialization by measurement protocol is presented to enhance the preparation of the ground and excited state in Section 5.4.3.

5.1 Paramp pump phase optimization

In this section the procedure of optimizing the relative phase between the paramp pump tone and the resonator drive tone is explained. For this, a short description of the paramp calibration is given. To use the paramp as an amplifier with high gain first the voltage which is applied to the coils beneath the SQUID loops of the paramp has to be adapted so that a high gain is found at the resonator frequency (see Figure 3.15). Furthermore, the pump power has to be calibrated as well as the displacement signal, which should cancel the pump tone reflected from the paramp as shown in Figure 3.14. The strong pump has to be prevented to enter the input of the paramp so that no photons leak back in the resonator and e.g. shifts the qubit frequencies by an AC Stark effect. Furthermore, it has to be canceled from the output port to keep the input power of the HEMT amplifier low. This is a non-trivial task due to the highly non-linear behavior of the paramp near the bifurcation point [43]. Therefore,

optimization algorithms have been written by Christopher Eichler, Jonas Govenius [43] and Lukas Heinzle [46] to find a point with high gain and low cancellation. Practically, gains in the region of 20 to 25 dB and cancellation between 0 to -10 dB were reachable.

After the paramp has been calibrated, the optimal phase relation ϕ_{RF} between the pump tone of the paramp and the resonator drive has to be found for using the paramp in the phase-sensitive mode. ϕ_{RF} can be varied by tuning the phase of the I and Q inputs of the up-conversion mixer, for details see Section 4.3. In the experiments the I-quadrature was chosen to be amplified whereby Q is attenuated. Furthermore, also the phase of the LO signal ϕ_{LO} in the analog down-conversion has to be adapted so that the signal-to-noise ratio is optimized in the I-quadrature as well. To achieve the optimization of both phases in one measurement ϕ_{RF} is swept in the measurement while ϕ_{LO} can be varied for each ϕ_{RF} in the data analysis afterwards. In the analysis the difference between the $|0\rangle$ and $|1\rangle$ state in the I-quadrature of the measurement data is maximized:

$$\Delta I(\phi_{LO}) = \mathrm{Re}[e^{-i\phi_{\mathrm{LO}}} I(|0\rangle)] - \mathrm{Re}[e^{-i\phi_{\mathrm{LO}}} I(|1\rangle)] \tag{5.1}$$

The result is shown in Figure 5.1a where the black square marks the point of the optimized phases. In Figure 5.1b the measured data points are shown for the optimal ϕ_{LO} and the extracted ϕ_{RF}^{Max} is labeled. This measurement is performed in the averaging mode and analyzed at the point in the filtered time trace which is later used for the feedback decision. The optimized angles have an accuracy of approximately 10° which can be explained by a flat distribution of $\Delta I(\phi_{LO})$ around the maximum point.
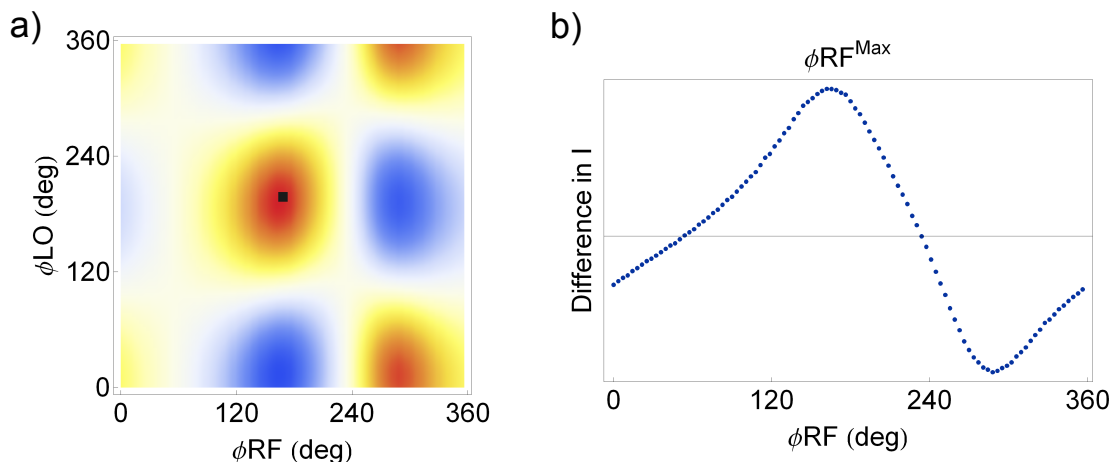

Figure 5.1: The analyzed data of ϕ_{RF} and ϕ_{LO} in an averaged measurement: a) A density plot of ϕ_{RF} and ϕ_{LO} where the black square marks the optimal phases to operate the paramp. b) The difference of $I(\phi_{RF})$ is shown for the optimal ϕ_{LO}. The dependence of the amplification on ϕ_{RF} is clearly visible. To maximize the contrast in the I-quadrature ϕ_{RF}^{max} is chosen.

To improve the readout fidelity further ϕ_{RF} and ϕ_{LO} can be calibrated more precisely by using single-shot measurements. ϕ_{LO} is optimized by rotating the means of $|0\rangle$ and $|1\rangle$ in the I-Q plane to the I-axis. The dependence of the single-shot fidelity on ϕ_{RF} is illustrated in Figure 5.2. For a range of 20° the readout fidelity varies between 74 % and 77 % where the single-shot fidelity is limited due to decay and thermal excitation which is described in more detail in Section 5.3. Here, the focus lies on the properties of the cumulative probability

distributions of $|0\rangle$ and $|1\rangle$. As one can see in Figure 5.2 the 'S-curves' are maximally separated in I-direction for the highest readout fidelity which is plotted in the yellow curves. For $\phi_{RF} = 135°$ and 140° the maximum fidelity is shifted to lower voltages in the I-quadrature because the excited state is broadened which can also be observed in time resolved histograms which are depicted in Figure 5.3. At $\phi_{RF} = 142°$ the $|1\rangle$ and $|0\rangle$ state are as symmetric as possible in this measurement and the symmetry gets lost towards the $|0\rangle$ state for higher ϕ_{RF} which is well illustrated in the time resolve histograms. An explanation for this behavior is that the paramp amplifies one quadrature while squeezing the other one and therefore, an asymmetry is found for a non-ideal phase.

In conclusion, the optimal phases for the pump tone as well as for the LO of the analog down-conversion can be found in two steps. First, in an averaged measurement the optimal area of phases can be approximated and afterwards determined more accurately by analyzing the single-shot measurements. The experimental results of the feedback experiments which are shown in the following sections are recorded after such an optimization of ϕ_{RF} and ϕ_{LO}.
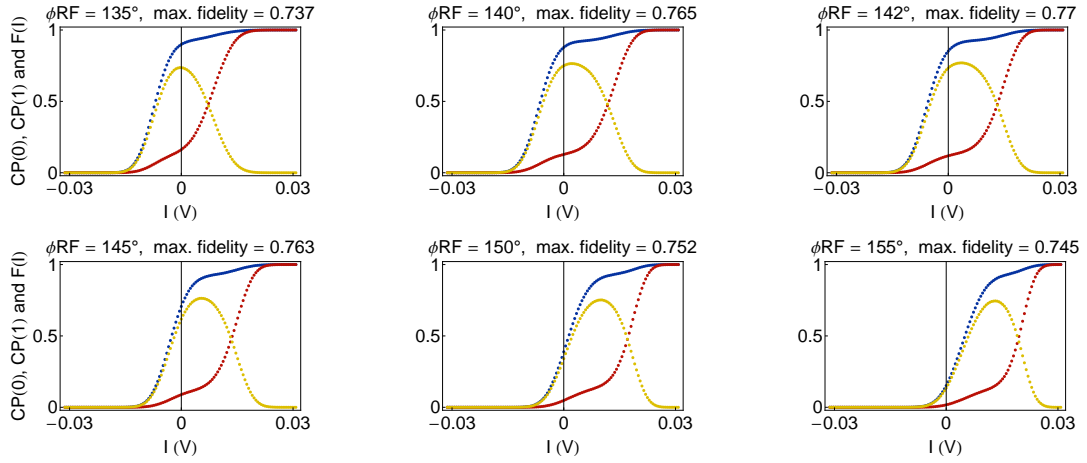

Figure 5.2: The cumulative probability distributions for $|0\rangle$, $|1\rangle$ and the resulting single-shot fidelity which is the difference between these 'S-curves' is shown for different values of ϕ_{RF}. At the most symmetric point the fidelity reaches its maximum.
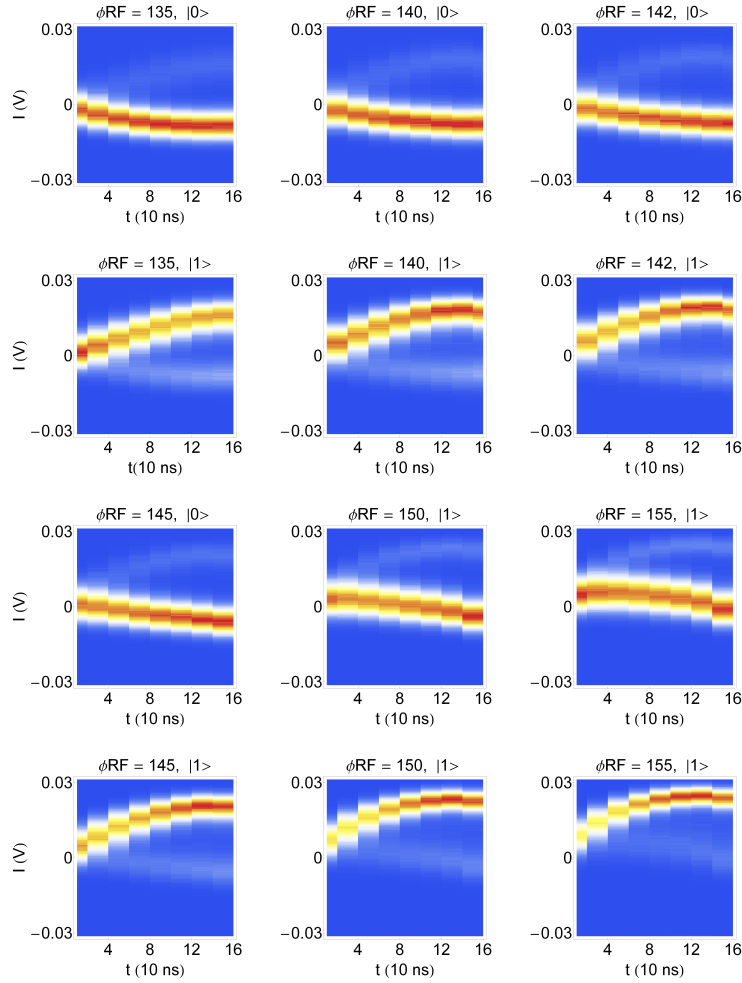
Figure 5.3: In the time resolved histograms of the I-quadrature a shift of the asymmetric form of the excited state for $\phi_{RF} = 135°$, $\phi_{RF} = 140°$ to a more symmetric case for $\phi_{RF} = 142°$ is observable. For higher values of ϕ_{RF} the symmetry gets lost towards the ground state.

5.2 Improvements of the phase stability

During the single-shot and feedback experiments a drift of the optimal phases has been observed. This phase drift happens on the time scales of 30 to 60 min and has made a frequent recalibration of ϕ_{RF}, ϕ_{LO} necessary to perform experiments with high fidelity. Therefore, we have measured the phase stability between the MWG of the pump tone and the one of the resonator drive by the phase optimization method in the average case. Moreover, we have analyzed the influence of pattern reloads on the AWG. The results can be seen in Figure 5.4 where the drift of ϕ_{RF} lies between 20° to 25° over a measurement time of 100 min. Apart from the fast drift at the beginning of the measurement without reload of the pattern the two curves are similar and can explain the previous observed decrease of the single-shot fidelity during the measurements.

Because the reload of the pattern has no noticeable influence only an intrinsic phase drift of the AWG could take place on this side. On the other hand, if a phase drift occurs between the MWGs this can be circumvented by using the same MWG for the pump of the paramp and the resonator drive for which the circuit is depicted in Figure 5.6. This experimental setup

has been realized and tested. Nevertheless, it brings the further issue that an IF frequency of 0 MHz has to be chosen at the I and Q inputs of the mixer which switches the measurement pulse. This is necessary, since the paramp pump and the resonator drive have to be at the same frequency to operate the paramp still in the phase-preserving mode. Therefore, leakage through the mixer can enter the resonator directly at its resonance frequency what has to be prevented. To achieve this an additional variable attenuator (Weinschel DA6-30) has been added at the output of the mixer to reduce leakage into the resonator. Furthermore, it allows to sweep the measurement drive power, while holding the amplitude at the I, Q inputs of the mixer constant.
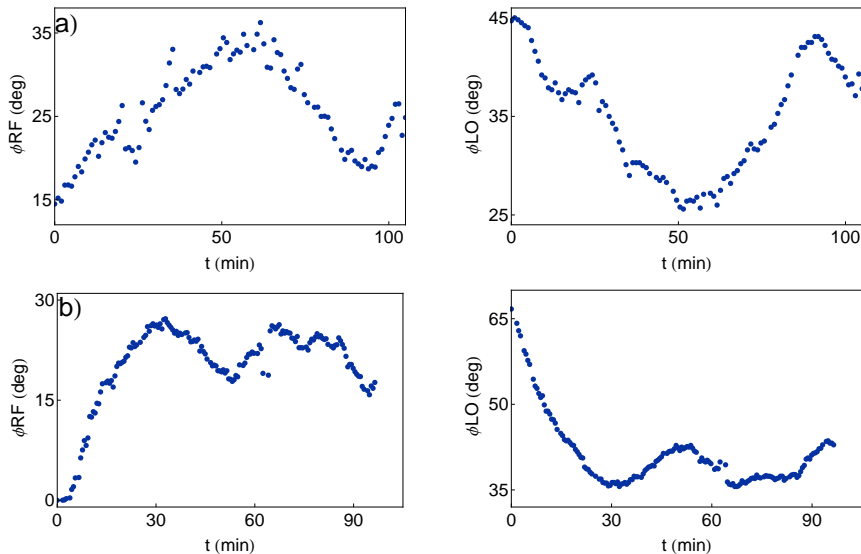

Figure 5.4: A phase stability test of the optimal ϕ_{RF} in an averaged measurement for approximately 100 min. A phase shift can be monitored for the case where the pattern on the AWG is reloaded (a) as well as without reload (b). The drift is in the range of $20°$ to $25°$ and can explain the decrease in the single-shot readout fidelity which has been noticed during the experiments.

If the leakage can be reduced so far that the average photon number $\langle n \rangle$ in the resonator is given by the thermal photons in the resonator a constant qubit frequency can be observed in an AC Stark shift measurement. In general, the predicted AC Stark shift of the qubit transition frequency $\Delta\nu_{\mathrm{AC}} = 2\chi\langle n \rangle$ is a linear function of the average photon number. Hence, it is directly proportional to the power of the resonator drive [34, 72], which is explained in Section 3.1 and Section 3.3.2. This phenomenon has been measured in the uncombined case of the MWG with a finite IF frequency of 240 MHz by sweeping the amplitude $A_{I,Q}$ at the I and Q inputs of the mixer which is shown in Figure 5.5a. The resonator drive power is proportional to $A_{I,Q}^2$ and thus, $\Delta\nu_{\mathrm{AC}}$ changes in a quadratic way in this measurement. A saturates below an amplitude of 99 mV is extracted, which indicates that a constant number $\langle n \rangle < 1$ of photons is in the resonator. The same experiment has been performed in the combined setup by changing the attenuation Att of variable attenuator. Therefore, the applied power is proportional to $10^{\mathrm{Att}/10}$ which is depicted in Figure 5.5b. In this case, the qubit transition frequency stays constant above an attenuation of -18dB. Consequently, the number of photons can also be reduced to residual thermal photons in the resonator, if the signal of one MWG is used. From this point of view measurements can be performed as in the uncombined case.
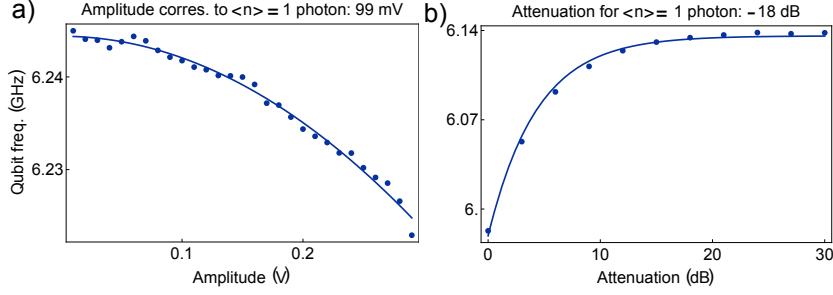
Figure 5.5: AC Stark shift measurements to point out that a constant number of photons is reachable in the resonator: a) The measurement tone is switched with an I-Q mixer at an IF frequency of 240 MHz. The power of the drive is varied by changing the amplitude A_{IF} at the I, Q input ports. Therefore, the qubit transition frequency changes in a quadratic way and a saturates below an amplitude of 99 mV. b) Here, an IF frequency of 0 MHz is used at the I, Q inputs of the mixer and the output signal is damped with an variable attenuator. The qubit transition frequency follows a exponential law and stays constant above an attenuation of -18 dB. This is a strong indication that only thermal photons are left in the resonator.
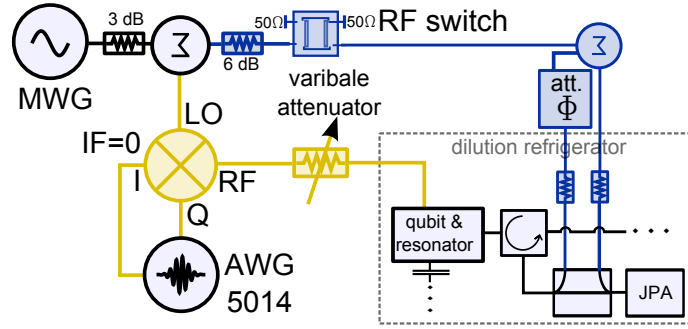

Figure 5.6: The relevant parts to combine the resonator drive and the paramp pump tone at one MWG are depicted. To switch the measurement an I-Q mixer with an IF frequency of 0 MHz is used and the LO leakage is reduced by the variable attenuator. The attenuation in the paramp pump line are chosen in such way that an input power at the LO input of the mixer near the 1 dB compression point can be used while also the paramp pump power is optimized for a high gain. The RF switch is introduced to switch the paramp pump tone between the measurements.

After the basic requirements of the combined setup have been examined, the phase stability has been tested. In Figure 5.7 the drift of ϕ_{RF} and ϕ_{LO} is plotted over a time of approximately 200 min. Besides a short drift at the beginning an oscillation in the range of 6° occurs. Therefore, the precision of the measurement of about 10° has also to be considered which is described in Section 5.1. This results in a phase stability of ϕ_{RF} at the required level which allows to perform experiments over a long time scale without recalibrating the phase. ϕ_{LO} shows a strong drift in the first 150 min of this measurement and then stays constant which has been also observed during single-shot measurements. This drift is less problematic because the optimal LO rotation is analyzed in each feedback experiment and can therefore be compensated easily during the measurements. Note, that the stability of the measurement setup is also limited by the paramp calibration where especially the cancellation has to be recalibrated in time intervals of the order of 3 h which has not been observed systematically

during this thesis.

Summarizing, the combination of the resonator drive and the paramp pump tone at one MWG enhances the phase stability to an adequate precision to have a reasonable measurement time after the calibration of the system. Furthermore, it has been shown that the LO leakage through the mixer can be fully reduced by using a variable attenuator.
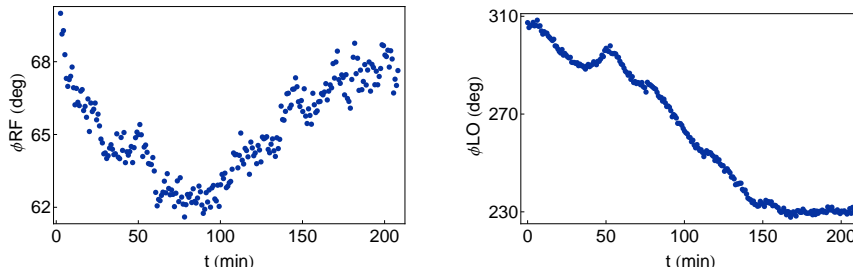

Figure 5.7: The result of the phase stability test for the combined paramp pump tone and resonator drive tone at one MWG over a period of 200 min. ϕ_{RF} oscillates in a range of approximately 6° and therefore, fulfills the requirements to perform experiments on long time scales. ϕ_{LO} drifts strongly in this experiment, but can be easily compensated during the single-shot and feedback experiments and hence, does not influence the long time usage of the setup.

5.3 Analysis and comparison of the single-shot readout

In this section the single-shot readout performance at two different qubit transition frequencies is compared. The resonance frequency of the resonator is $\nu_{res} \approx 7.134$ GHz and the decay rate $\kappa/2\pi \approx 6.8$ MHz. At first, the qubit has been tuned to a frequency of 6.514 GHz which results in χ/κ ratio of approximately 0.35. This has been measured by two resonator spectroscopies with the qubit being in $|0\rangle$ or $|1\rangle$, respectively, like described in Section 3.3.2. The qubit lifetime T_1 is on the order of 1000 ns and the coherence time $T_2^* \approx 270$ ns. At qubit transitions frequencies closer to the resonator we measured lifetimes which are limited by the Purcell effect [63] and therefore, higher χ/κ ratios were not be studied in the single-shot case. Even at the 6.514 GHz point the single-shot readout fidelity is mainly limited due to qubit decay before the measurement which can be seen in Figure 5.8. Figure 5.8a shows the progress of the single-shot readout in steps of 20 ns. The readout fidelity reaches its maximum at 40 ns, but the best separation in the I-direction is given for a readout time of 100 ns. This can be explained by the decay of the qubit, which can be clearly seen in the S-curve for the excited state (red). Figure 5.8b illustrates this further. First, the excited state population at the different measurement points is fitted to extract T1. The measurement result agrees well with an average measurement of T1. Furthermore, the occurrences for the qubit prepared in the excited and ground state are shown at a measurement time of 80 ns. At that point a decay of the about 18 % is found which mainly limits the readout fidelity. To reduce the effective readout time of the qubit, in this measurement, as in all measurements presented in this chapter, the so called On-Hold sequence is used to populate the resonator more quickly [43]. We used this sequence with a strong On-pulse of $t_{on} = 3$ ns followed by a Hold-pulse with an amplitude of

$$A_{\text{Hold}} = t_{on}\sqrt{\frac{\chi^2 + \kappa^2}{4}} \tag{5.2}$$

to keep the number of photons in the resonator in a steady state during the measurement.
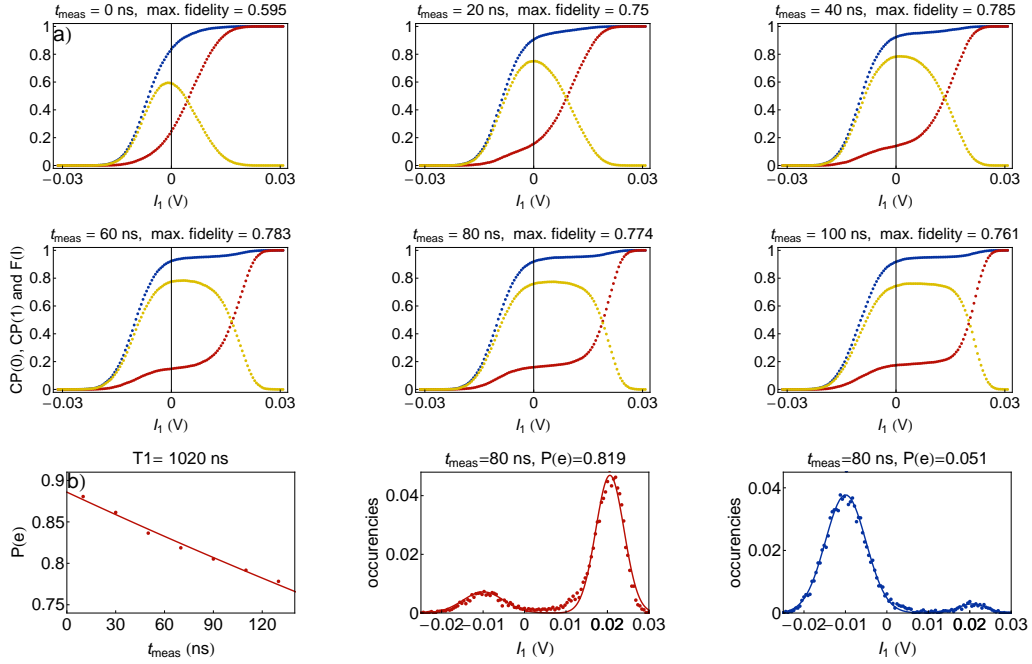

Figure 5.8: a) Time resolved measurement of the single-shot readout fidelity for the qubit tuned to 6.514 GHz. The maximum fidelity is reached at 40 ns where the best separation of the ground and excited sate in the I-direction is given at 100 ns. b) On the left side, the extracted T1 from the measured excited state probabilities is shown. In the middle and on the right side the occurrences for the qubit prepared in the excited and ground state for $t_{meas} = 80$ ns are plotted.

To perform feedback experiments the qubit state has to be measured twice with a minimal time difference of 300 ns and hence, an increased qubit lifetime is required such that the performance is not limited by a qubit decay between the measurements. This aim has not been reached with the current sample, but the situation is improved by tuning the qubit transition frequency to approximately 6.146 GHz. Here, χ is too low to be observed directly in a resonator spectroscopy measurement. Therefore, it is obtained by measuring the anharmonicity of the qubit and fitting the measured data to the analytic solution of the CPB Hamiltonian [5]. With this method a χ/κ ratio of 0.18 is calculated. Furthermore, a T_1 of approximately 1400 ns and T_2^* of about 280 ns is found for this qubit frequency.

To compare both situations the drive amplitude ϵ is calibrated by AC Stark shift measurements so that the photon number in the resonator is about 30. This has been identified to be ideal for the single-shot readout as it is close to the critical photon number for the 6.514 GHz case. Moreover, for 6.146 GHz no higher readout fidelity has been reached for higher drive powers, because the two states start to get asymmetric which we explained as a power broadening of the states. Furthermore, the gain of the paramp was approximately 24 dB and the cancellation about −5 dB in both measurements. As an incidental remark, all further single-qubit feedback experiments are performed at similar conditions.

First, the ratio of the differences between the mean values of the ground and excited state distributions can be compared to the expected ratio in the limit of a infinite qubit lifetime.

Therefore, the ground state distribution without thermal excitations as well as the excited state distribution without decay are chosen in the experimental data. These mean values are marked in Figure5.9 as vertical black lines. Theoretically, a ratio of

$$\frac{\langle I_{|0\rangle}^{\chi/\kappa=0.35}\rangle - \langle I_{|1\rangle}^{\chi/\kappa=0.35}\rangle}{\langle I_{|0\rangle}^{\chi/\kappa=0.18}\rangle - \langle I_{|1\rangle}^{\chi/\kappa=0.18}\rangle} \approx 1.48 \tag{5.3}$$

is expected, where a ratio of

$$\frac{\langle I_{|0\rangle}^{6.514}\rangle - \langle I_{|1\rangle}^{6.514}\rangle}{\langle I_{|0\rangle}^{6.146}\rangle - \langle I_{|1\rangle}^{6.146}\rangle} = \frac{0.028\ V}{0.02\ V} \approx 1.45 \tag{5.4}$$

is measured which confirms the theoretically expected value. The overlap in the ideal case of no qubit decay and no thermal excitation between the ground and excited state distribution increases from 0.2 % for a qubit frequency of 6.514 GHz to 1.2 % for a frequency of 6.146 GHz which defines the theoretical upper limit of the readout fidelity. But in the experimental situation, the readout fidelity is limited by thermal excitations and the qubit decay before the measurement which is described in detail for the qubit at a frequency of 6.514 GHz. Thermal excitations of the qubit can be seen in the histograms as a remaining peak at the excited state position where the qubit should be in the ground state. The thermal excitation of the qubit has been in the range from 6.0 % to 7.5 % for base stage temperatures from 60 mK to 110 mK. For these temperatures thermal excitation from 0.4 % to 4 % would be expected in average and hence, more thermal noise is probably introduced to the chip through the wiring. Furthermore, an imperfection of the π-pulse has to be taken into account. This can be estimated by about 1.5 % from the residual ground state occupation when the qubit is prepared in the excited state.

Moreover, the deviation of the Gaussian fit from the experimental data if the qubit is excited by a π-pulse shall be considered shortly. The fit deviates mostly at the center region between the ground and excited state peak which can be understood by the finite bandwidth of the paramp. In the experiments, a bandwidth of about 50 MHz was measured and therefore, the qubit decay which theoretically takes place instantaneously, gets extended in time. The result is, that the probability of having measurement results between the ground and excited state distribution is increased, which explains why the fit leads to asymmetric over-estimation.

Table 5.1: Overview of the extracted parameters from a fit of the excited and ground state distribution with a Gaussian function.

ν_{qubit}	6.514 GHz	6.146 GHz
$\langle I_{|0\rangle}\rangle - \langle I_{|1\rangle}\rangle$	0.028 V	0.02 V
max. readout fidelity	77.4 %	77.0 %
overlap	0.2 %	1.2 %
thermal excitations	5.2 %	7.6 %
decay	9.4 %	6.9 %

At the end of the analysis of the single-shot fidelities the possibility of pre-selection measurement runs shall be explained to decrease the error in the readout fidelity due to thermal

excitation. The main idea is that one performs a measurement before the actual experiment and takes only those measurements for the further analysis for which the qubit was initially in the ground state. The efficiency of this procedure can be further increased by a state dependent feedback on the qubit, if it has been measured in the excited state which shall be described in more detail in the next section.
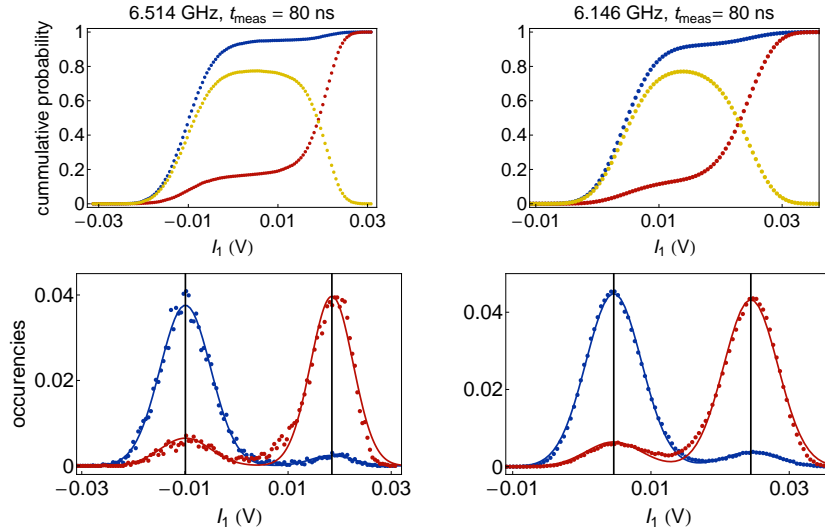

Figure 5.9: The single-shot readout results for qubit frequencies of 6.514 GHz and 6.146 GHz are shown at a measurement time of 80 ns. On the upper plots the cumulative probability distribution for a qubit prepared in the ground or excited state are presented where on the lower ones the occurrences for these cases are depicted.

5.4 Feedback Experiments

Besides the single-shot readout the main focus of the experiments is the realization of a measurement-based feedback. Previous experiments had been realized by Yves Salathé and Thomas Karg [48]. These experiments have been repeated and improved during this thesis. The main improvements at the technical side concern the phase stabilization and an increase in the single-shot readout fidelity. Furthermore, the measurement applications on the FPGA are enhanced, which are explained in Section 4.4.

First, a evaluation of the feedback loop is presented where the qubit is prepared in a superposition state and is brought to the ground or excited state by a feedback action. Next, the suppression of Rabi oscillation with the help of feedback pulses will be explained in Section 5.4.2. Finally, a qubit initialization by measurement protocol is presented which allows to enhance the qubit state preparation.

5.4.1 Evaluation of the feedback loop

In order to test the performance of the feedback algorithm, the qubit is prepared in a superposition state

$$|\psi\rangle = \frac{1}{\sqrt{2}}(|0\rangle + \mathrm{e}^{-i\phi}|1\rangle) \tag{5.5}$$

by applying a $\pi/2$-pulse. Two measurements are performed where in the first one the decision of the feedback operation is made and the result is tested in the second measurement.

A π-pulse is chosen for the feedback operation. The measurement scheme can be seen in Figure 5.10a where in the second measurement the qubit should be found in the ground or excited state dependent on the feedback case.

To decide if a feedback operation should be performed, a threshold in the I-quadrature can be set on the FPGA. A feedback pulse can be given for measurement results above (FB>=) or below (FB<) that threshold. The optimal threshold is given at the intersection point of the Gaussian distributions of the ground and excited state and is shown in 5.10b as the green line. To set this threshold in the experiment, first a calibration measurement has to be made. Out of this the optimal threshold is extracted and set in the FPGA for the pursuing feedback experiments. Due to the feedback enabled trigger the optimal threshold can also be extracted in each feedback experiment and adapted for the next measurement run. By this iterative method we realized feedback experiments with an optimal set threshold. The threshold which is used on the FPGA is shown in red in Figure 5.10b and deviates about a value of 0.013 in units of I_1/I_1^{max}.
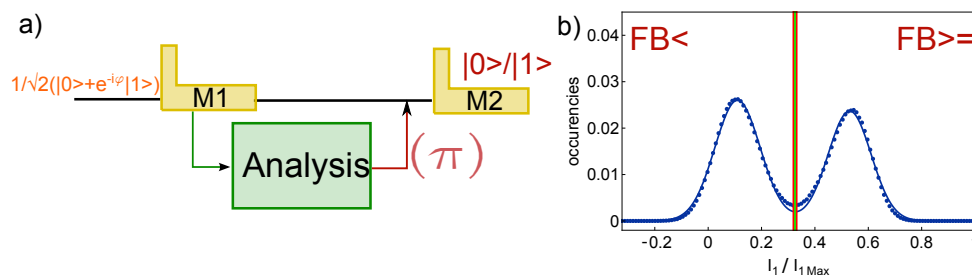

Figure 5.10: a) The measurement sequence to evaluate the performance of the feedback operation is presented. The qubit is prepared in a superposition state and a π-pulse is performed in the feedback operation. b) Plot of the occurrences where the qubit is prepared in the superposition state. The vertical green line indicates the optimal threshold for the qubit state estimation as well as the feedback decision. The red line shows the threshold that has been set in the FPGA. The feedback operation can be performed above (FB>=) or below (FB<) this threshold.

To illustrate the feedback measurement results 2D correlation histograms can be extracted out of a measurement with the correlator FPGA application and are depicted in the first row of Figure 5.11. On the horizontal axis the I-quadrature of the first measurement and on the vertical axis the I-quadrature of the second measurement is plotted. Therefore, the vertical (horizontal) red line indicates the threshold in the FPGA in the first (second) measurement. For example, if the qubit is measured in the ground state in both measurements, a result below both thresholds is found in the correlation histogram. However, if the qubit is first measured in ground and second in the excited state a point occurs in the histogram below the first, but above the second threshold. The other two cases can be explained similarly.

In the first 2D correlation histogram the reference measurement is shown and a superposition state is observable where the qubit is mostly detected either twice below or above the threshold. The third peak above the first, but below the second threshold identifies the decay between the first and the second measurement.

In the next correlation histogram a feedback pulse is applied for points above the threshold and therefore the peaks above the first threshold are flipped. For the FB< case a feedback pulse is given below the threshold and therefore the left parts are exchanged.
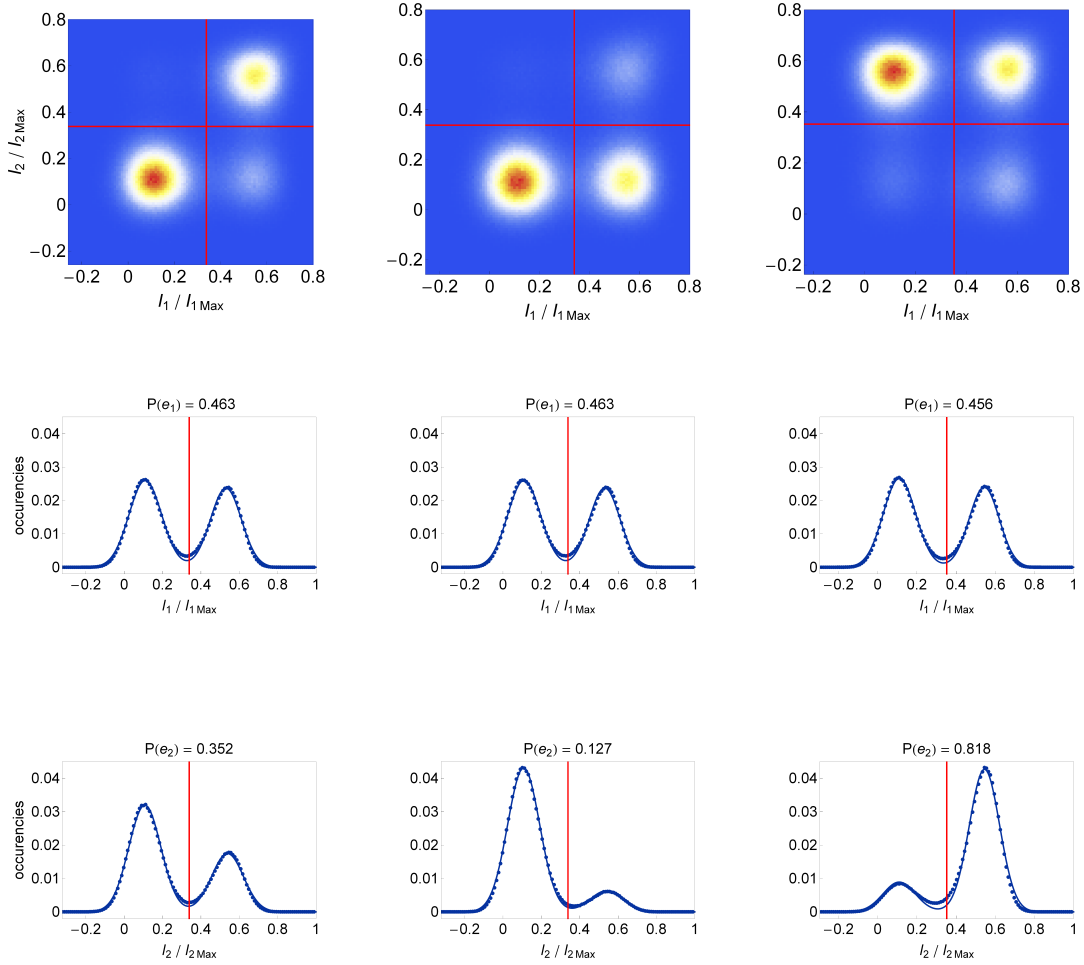
Figure 5.11: Results of the evaluation of the feedback loop: On the left side the reference measurement is shown where no feedback operation is performed in the measurement. In the first row, 2D correlation histograms are depicted where the I-quadrature of the first measurement is plotted on the horizontal axis and that of the second measurement on the vertical axis. Next, 1D histograms of the first and second measurement are shown to extract the populations in both measurements. This data is recorded in the same measurement as the FB>= which is possible due to the feedback enabled trigger. In the middle the results of the FB>= case are presented and on the right side of the FB< case in the same order as the reference measurement.

This qualitative picture can be analyzed in more detail by extracting the occurrences in the first and second measurement. Furthermore, the time between the pulse and the measurements is extracted in a time-resolved single-shot reference measurement where the qubit is excited by a π-pulse like it is shown in Figure 5.8. The result of the timing measurement can be seen in Figure 5.12. As fit function $\exp[-(t + \Delta t)/T1] - P(e)_{\text{thermal}}$ is used where $P(e)_{\text{thermal}}$ defines the thermal excitations in the system. The T1 times agree with an average measurement. The distance between the state preparation pulse and the start of the first measurement is $\Delta t_1 = 20$ ns and to the second measurement $\Delta t_2 = 410$ ns. Therefore, all relevant time intervals to analyze the decay of the qubit during the measurement are extracted. They will be used in the further analysis of the feedback test. In the first measurement which corresponds to the second row of Figure 5.11 a ratio of the ground and excited states occupancy of 54 % to 46 % is found which deviates from the parity due to the decay of the excited state and the

imperfect $\pi/2$-pulse. The data is measured 80 ns after the start of the measurement pulse and therefore, a decay of approximately 7.9 % is expected. In the first measurement an excited state occupancy of 46.3 % is found. Due to the decay a population of 46 % is expected. In the second measurement which is depicted in the third row of Figure 5.11 a further decay of qubit can be seen in the reference measurement by circa 10.9 % which is also predicted by the measured T1 and Δt_2 . For the FB> case the residual excitation of the qubit can also mostly be explained by the decay of the qubit. It is measured in the excited state and therefore, a feedback pulse will be given, but in the meantime the qubit decays to the ground state. The feedback π-pulse is given 390 ns after the state preparation pulse and therefore, P(e) is 37.8 % at this moment. The residual mismatch of 0.5 % to the measured populations of the excited state of 12.7 % originates from the imperfect pulses and from a detection error in the first measurement. On the right side the FB< case is shown where the qubit is mostly in the excited state after the feedback operation. Due to a decay between the feedback π-pulse and the second measurement a occupancy of the excited state of 82.3 % is expected at the measurement time. Hence, again a residual error or 0.5 % has to be explained for the FB> case by the readout and the imperfect pulses.

Summarizing the results of the evaluation, the measured data can be well explained by the decay of the qubit in the time between the state preparation and the readout. Therefore, the test of the feedback loop is successful which is also confirmed by the experiments in Section 5.4.2 and Section 5.4.3.
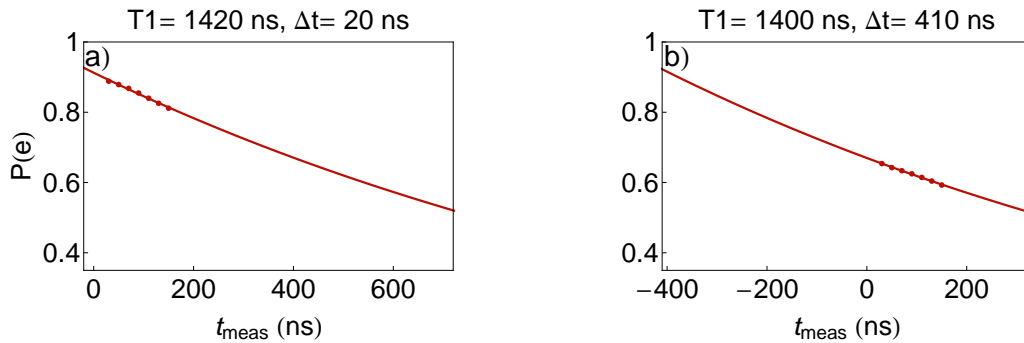
Figure 5.12: a) To analyze and explain the probabilities of the ground and excited state in the first and second measurement the timings between the state preparation and the beginning of the first measurement Δt_1 are extracted by an exponential fit to the data of a time resolved histogram measurement. Therefore, the time between the preparation and the first measurement amounts to 100 ns. The thermal excitation of the qubit are subtracted in the fit. b) The same approach is taken for the second measurement and here, a time between the feedback pulse and the readout of 110 ns is obtained.

5.4.2 Suppressing Rabi oscillations on the basis of feedback operations

A Rabi model was originally studied to measure the sign and magnitude of a spin in magnetic resonance experiments [64]. It can be generalized to any two-level system which is driven near the resonance frequency resulting in oscillations between the ground and excited state. The frequency of the oscillation is given by the Rabi frequency

$$\Omega_{Rabi} = \sqrt{\Delta^2 + A^2/\hbar^2} \tag{5.6}$$

with $\Delta = \omega_{\text{drive}} - \omega_{01}$ and $A = -d_{01}E$ where d_{01} is the transition dipole moment and E the magnitude of the electric field [39]. Due to the proportionality to E, a Rabi experiment in which the pulse amplitude is steadily increased can be used to calibrate the pulse amplitude of the qubit drive. A typical Rabi oscillation can be seen in the reference measurement in Figure 5.13 where the data is fitted with the theoretically expected excited state probability $P(e) = \frac{A^2}{\Omega_{\text{Rabi}}^2 \hbar^2} \sin \Omega_{\text{Rabi}} t/2 + \Phi$.

To show that the qubit initialization can be improved on the basis of feedback pulses a suppression of Rabi oscillation will be presented. The experimental scheme is similar to the feedback test of Section 5.4.1 where the qubit is prepared like in an usual Rabi experiment and the feedback pulse consists of a π-pulse. For the FB< case a feedback is given every time the qubit is measured in the ground state and therefore, the qubit should end up in the excited state independent of the Rabi pulse amplitude. The reverse argument holds for the FB>= case where the qubit ends up in the ground state. The results of the two different feedback cases are shown in Figure 5.13. In the reference measurements the qubit is found with P(e)≈ 7.5 %, if no pulse is applied and with P(e)≈ 86 % for a π-pulse due to the decay of the qubit before the measurement. These probabilities are extracted from single-shot measurements and will be detailed in the next section. Furthermore, all three measurements which are shown in Figure 5.13 are normalized on the basis of these probabilities. In the situation where feedback pulses are given dependent on the result of the first measurement, the thermal excitation can be reduced in the system and therefore, the qubit can be prepared with an enhanced probability in the ground or excited state. Therefore, the feedback data points are in average found at lower or higher probabilities which can be seen at the first points in Figure 5.13. The contrast between the two feedback cases is steadily reduced if the qubit is prepared more likely in the excited state which can be explained by the decay of the qubit in the time between the preparation and feedback pulses.

This measurement illustrates qualitatively the positive effect of a feedback-based initialization which will be considered more in detailed in the next section. Another possibility to proof the feedback performance is to do a Rabi experiment after the qubit state is prepared by an initialization by measurement protocol. Therefore, an increased contrast in the Rabi oscillation should be extracted [67]. On the other hand, the decay of Rabi oscillations can also be inhibited through quantum feedback control which has also been demonstrated recently in superconducting circuits [80].
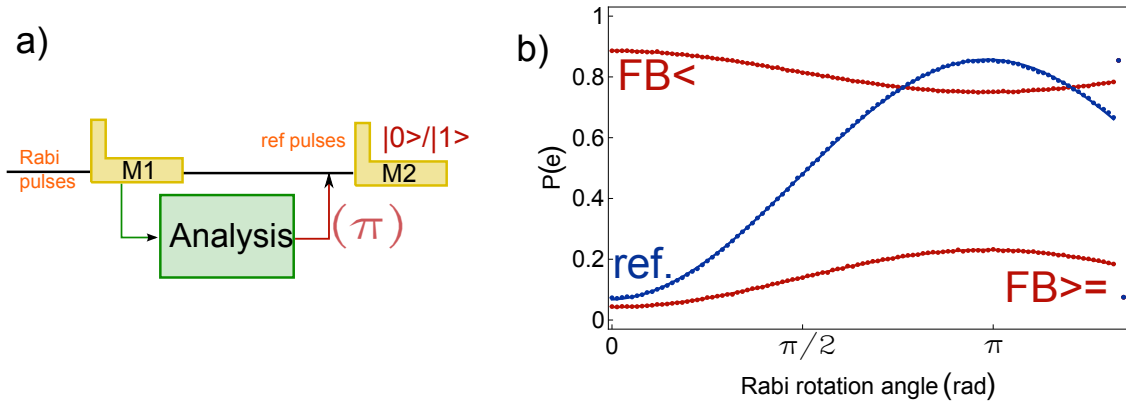
Figure 5.13: a) The pulse sequence to suppress Rabi oscillation by applying feedback operations is illustrated. b) The result of the Rabi experiment is plotted where the reference measurement is colored blue and the two feedback cases red. A suppression of the Rabi oscillation is clearly visible in both of them.

5.4.3 Feedback based state initialization

The next feedback experiments have been performed to proof the state initialization by measurement protocol with the current sample. Therefore, the qubit is prepared without a pulse (0-pulse) as well as with a π-pulse where the result is plotted in the references of Figure 5.14. The FB>= operation is performed, if one wants to initialize the qubit in the ground state, whereas the FB< case is carried out to prepare the excited state.

From the reference measurement with a 0-pulse as well as in the 1D histogram of Measurement 1 of the feedback cases, the thermal excitations of the qubit are extracted, which amount to about 7.5 %. To improve the ground state occupation feedback pulses are given, if the qubit is measured in the excited state in the first measurement (FB>=) and therefore, the population of the the excited state can be reduced to 4.8 % in the second measurement. In the first measurement of the reference π-pulse case, the qubit is initialized in the excited state by about 85.0 %. The reduction can also be explained by the thermal excitation and by a qubit decay before the measurement. By applying a feedback pulse, if the qubit is measured in the ground state (FB<), the occupation of the excited state can be increased to about 88.7 % which is visible in the 1D histogram of Measurement 2 in the FB< case. Since the decay times of the qubit before both measurements are nearly equal (see Figure 5.12), the conclusion can be drawn, that excited state initialization is also improved by using a feedback based initialization method. These results explain the enhanced qubit initialization at the beginning of the Rabi experiment which is presented in Section 5.4.2.
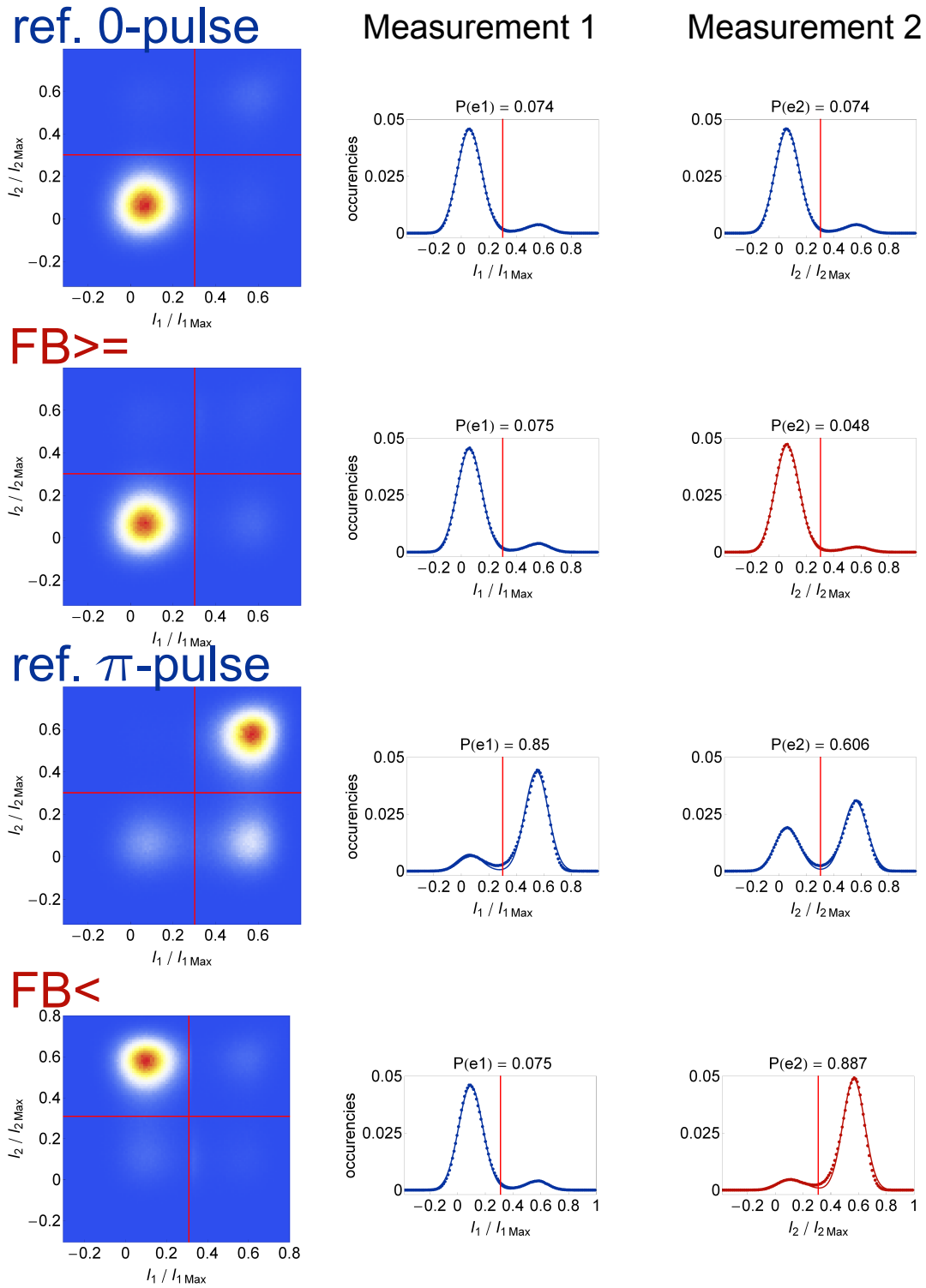
Figure 5.14: The reference and feedback measurements to proof the enhanced state initialization by a protocol which is based on feedback operations are presented. In the feedback experiments the thermal excitations of the qubit can be reduced to 4.8 % (FB>=) as well as the excited state preparation can be improved to 88.7 % (FB<).

Moreover, the state initialization by measurement protocol is detailed by two examples, if the qubit is in an arbitrary state. Assuming the qubit is found in an arbitrary superposition state at the end of the previous measurement run, e.g. like it is prepared for the feedback test in Section 5.4.1, the here presented feedback scheme can be used to initialize it in the ground state for the next run. In this experimental system we are able to initialize the qubit with 87.3 % in the ground state for an initialization time of 400 ns. Therefore, the active initialization brings the qubit about 5 times faster to the ground state than the passive initialization where a waiting time of about 2000 ns is required to get a similar ground state occupation. The same holds in principle for the second example where the qubit is prepared with a π-pulse and is returned to the ground state by feedback pulses. This situation is shown in Figure 5.15 for FB>= where in the first measurement a excited state occupation of 85 % is detected (see also the π-pulse reference measurement). In the second measurement the qubit is mainly in the ground state with about 23.4 % excited sate population left. Again a waiting time of approximately 2000 ns is necessary in the passive initialization method to reach this excited state occupation.

In contrast, if the waiting times in the passive method are increased, the qubit state population will reach the thermal steady state and therefore, an excited state occupation of about 7.5 %. A possibility to improve the active initialization method is to repeat the feedback loop several times. Therefore, the ground state occupation should result in at least 95 % as shown in the FB< initialization method to reduce thermal excitations.

Furthermore, the reduction of the contrast in the suppression of the Rabi experiment can be explained with an additional set of histogram data depicted in Figure 5.15. For the FB< experiment an excited state probability of 74.4 % is found in the second measurement which agrees well with the minimum of the population in the feedback Rabi experiment. In the second measurement of the FB>= case the excited state occupation of 23.4 % corresponds to the maximum probability of this case in the Rabi experiment. Therefore, the increased difference when the Rabi angle is 0 as well as the reduced contrast for a Rabi angle of π is explained.

Due to readout errors, thermal excitations during the measurement and the decay of the qubit before the feedback pulse a further improvement of the state initialization has not been achieved in this experiment. Nevertheless, these are no fundamental restrictions of this initialization method and it should be possible to improve them by increased lifetimes, reduced temperatures and better separation of the ground and excited state (see, e.g. the characteristics and single-shot readout results of qubit 3 in 'teleportation-sample' which are shown in Figure 6.5). A further improvement is the decrease of the feedback delay, although this would not decrease the time of the initialization method in a high amount. Since a time of approximately 170 ns has to be chosen between the end of the first measurement and the feedback pulse to avoid that residual photons of the first measurement are still present in the resonator at the time the feedback pulse is given

$$n < 1 \rightarrow t \approx 170 \text{ ns} \tag{5.7}$$

for $\langle n \rangle \approx 30$ and $\kappa/2\pi = 6.3$ MHz. Therefore, the minimal time of this protocol is limited also by this restriction.

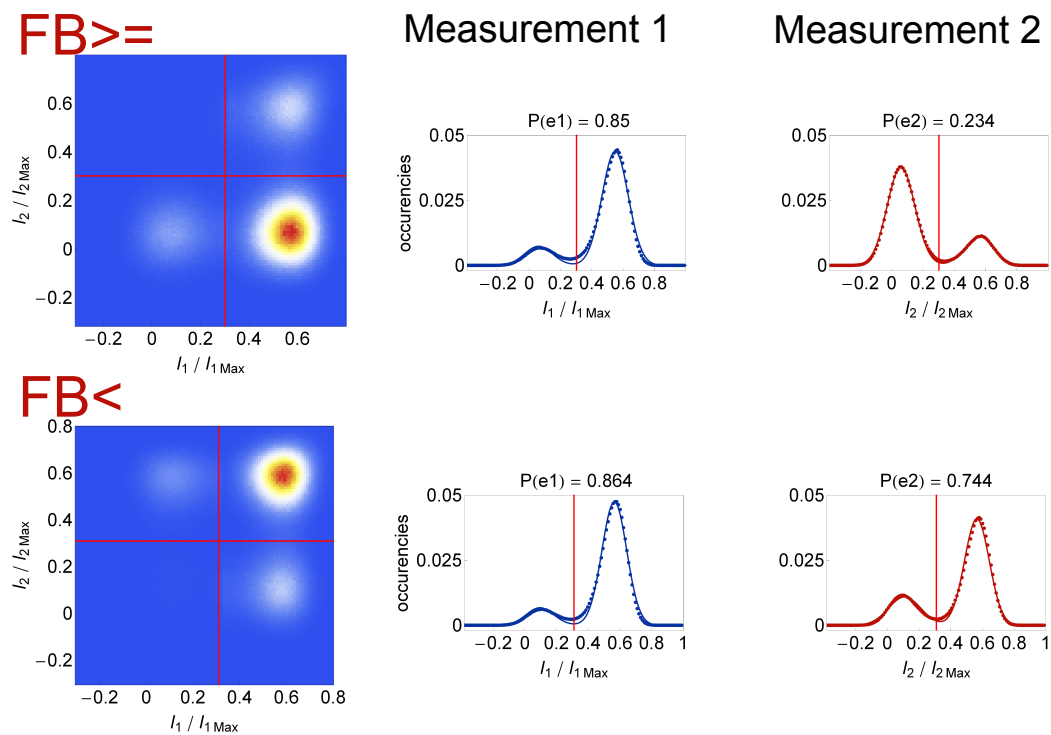Figure 5.15: The results of the feedback experiments when the qubit is prepared in the excited state are depicted. For the FB>= case the populations is 'flipped' by the feedback pulse. In the FB< situation mainly the qubit is excited by the feedback pulse, if it decays before the first measurement. This data explains the reduced contrast in the Rabi experiment for an Rabi rotation angle of π.

6 Towards full quantum teleportation

The implementation of the quantum teleportation algorithm is an important step to realize quantum computers [16, 86]. The full algorithm has been implemented in microscopic degrees of freedoms like single photons where long range quantum teleportation over 143 km has been demonstrated [56]. Furthermore, teleportation has been performed with continuous variable states [33] and in trapped ion systems [3, 66]. As described in Section 2.2.2 the quantum teleportation can be split into a non-classical and a classical part. In superconducting circuits the non-classical part has been implemented in 2012 in the quantum device lab up to the the single-shot readout using quantum state tomography to reconstruct the three-qubit state [4]. Further improvements in the qubit lifetimes and coherence times as well as a new sample design which is shown in Figure 6.1b makes the realization of the deterministic quantum teleportation possible [75]. Therefore, the qubit whose state should be teleported (Qb1) is coupled to a resonator different from the resonator to which the qubit of the receiver (Qb3) is coupled. They are linked by an ancilla qubit (Qb2) which shares separated resonators with Qb1 and Qb3. Due to this sample design Qb1 and Qb2 can be read out independently of Qb3. Moreover, quantum state tomography is executed on Qb3 to fully reconstruct its state and compare it with the prepared state of Qb1. Process fidelities of 69.9 ± 2.0 % for post-selection on one of the four two-qubit states have been obtained. In a second step, two-qubit readout techniques have been developed allowing two-qubit state estimation in each single-shot (for details see Section 3.4 and Section 6.1). Therefore, process fidelities of 58.8 ± 2.4 % have been reached which are well above the classical limit of $\frac{1}{2}$. This result is the first demonstration of teleportation in a macroscopic system and underlines the fast progress in superconducting circuits.

The remaining step towards the implementation of the full quantum teleportation scheme implies the possibility to perform the rotations on Qb3 dependent on the measurement result of Qb1 and Qb2. We implemented this feed-forward process in a similar way as the feedback loop in the sate initialization by measurement protocol which is explained in Section 4.3. For fast data processing again an FPGA based data analysis is used where the digital logic to sent two independent feedback triggers has been implemented (see Section 4.4 for details). Furthermore, two feedback pulse generation units have been set up where each contains an AWG520 and an I-Q mixer. The LO input is driven by the same MWG as used for the preparation pulses of Qb3. The relevant parts of this feed-forward setup are depicted in Figure 6.1. The dc voltage at one of the I-Q mixers is supplied from the dc outputs of an AWG5014 at the channels which are connected to the flux lines. The other I-Q mixer is connected to SRS dc voltage sources. Moreover, the possibility to reduce the effective readout time by performing the On-Hold-sequence has been realized in this setup, but has not been made use of so far. Since it possibly reduces the readout time it helps to decrease the dephasing of the qubits during the whole protocol.
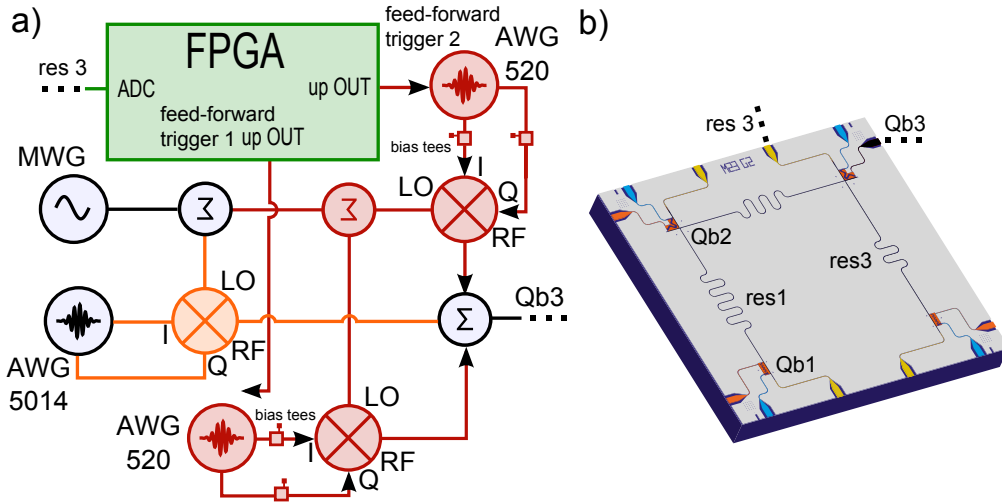
Figure 6.1: a) The feed-forward setup is depicted which allows to perform two independent feed-forward or feedback operations based on a prior measurement. The preparation (orange) and feed-forward (red) components are driven by the same MWG and for each feed-forward pulse a separate AWG520 is triggered by the FPGA. b) The rendering image of the sample which is used in the experiments which are presented in this chapter (for details see Section 4.1).

In this chapter the experimental results of the evaluation of the feed-forward process shall be detailed. Therefore, a comparison between an asymmetric 40-point Chebychev filter and boxcar filters is presented in Section 6.1 to examine the two-qubit readout while reducing the effective feed-forward time. To underline the result, the two-qubit readout with a 16-point boxcar filter in an optimal calibrated system is shown where a readout fidelity of 78.8 % is found. This result is fitted by the solutions in steady and the non-steady state case which are derived in Section 3.4. Next, a test of the feed-forward process is presented where a π-pulse is given on Qb3 dependent on the joined two-qubit readout of Qb1 and Qb2 in Section 6.2. Finally, suggestions for more advanced tests of the feed-forward setup are described which should lead to the implementation of the full quantum teleportation algorithm.
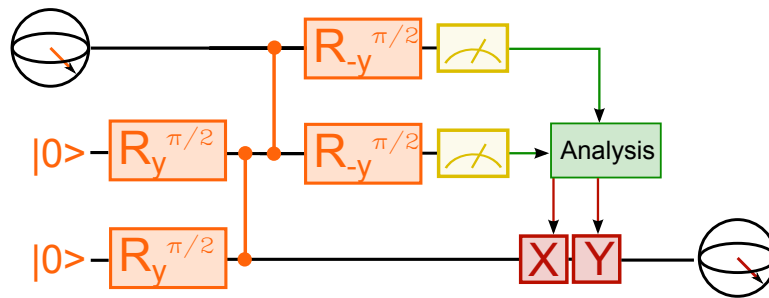

Figure 6.2: The circuit of the full quantum teleportation as it is implemented in superconducting circuits. The Hadamard and C-Not gates are decomposed in single-qubit rotations ($R_{\pm y}^{\pi/2}$) and controlled phase gates which are indicated by the vertical lines and explained in detail in Section 3.7.

6.1 Comparison of the two-qubit single-shot readout

The main focus of this section lies on the benchmarking of a 16-point boxcar (boxcar16) filter in comparison to an asymmetric 40-point Chebychev filter (cheb40) convolved with a 4-point Sinc with an effective bandwidth of 3.9 MHz. The deterministic quantum teleportation experiment is performed with the cheb40 filter. Therefore, we decided to compare it with boxcar filters which coefficients are 1/(Length of the Filter) to be normalized. Due to the fast multiplication on the FPGA with values of the form $1/2^n$ boxcar filters are very interesting to realize fast feed-forward processes. Furthermore, the filter length shall be chosen short to reduce the effective group delay of the filter [55]. The total feed-forward delay is measured with both filters and is found to be about 850 ns for the cheb40 and about 280 ns for the boxcar16 filter. This result underlines the speed advantage of the boxcar integration. To test the possibility of the two-qubit single-shot readout with this filter, unfiltered single-shot data is recorded and afterwards convolved with different filters.

For the two-qubit single-shot readout the paramp is operated in the phase-preserving, so that both quadratures of the signal are amplified equally. The paramp pump frequency is detuned by 6.25 MHz from the resonator drive frequency. 6.25 MHz are chosen, so that the measurement drive lies within the 3dB bandwidth of the paramp of 12 MHz and that it can easily be filtered out to receive a high qubit state estimation in the single-shot measurements. In this experiment is performed with a paramp gain of about 20 dB. The cheb40 filter is designed to operate the paramp at a detuning of 6.25 MHz and therefore, selected in the deterministic quantum teleportation experiment. To filter out the paramp pump by a boxcar filter a length of 16 points is required for the sampling rate of 10 ns [55]. Furthermore, the qubits are prepared in $|0\rangle$ and the second excited energy level $|2\rangle$ to achieve a better separation in the I-Q plane where the qubit frequencies are chosen for high T1 and $T2^*$ times and high fidelity of the two-qubit gates. Therefore, the resonator drive frequency is set to the center between the resonance frequencies of $|02\rangle$ and $|20\rangle$ which corresponds to $\Delta = 0$ in this case.
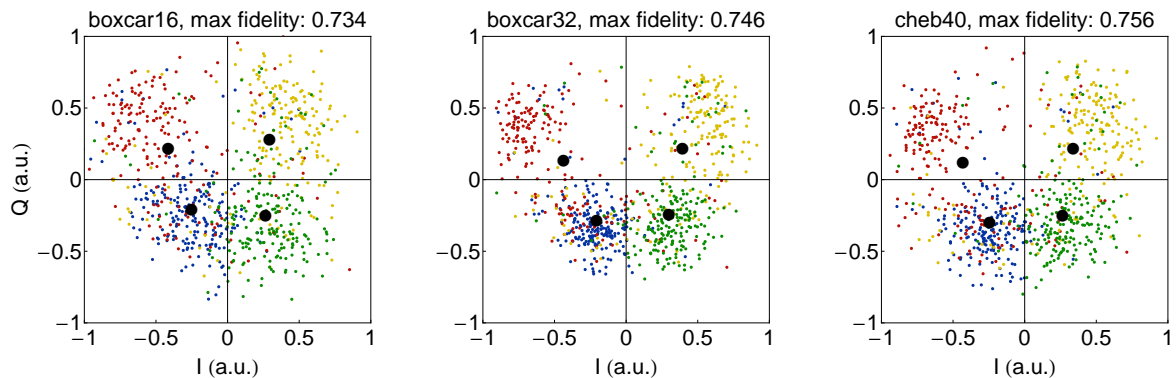
Figure 6.3: The joined two-qubit single-shot readout results of the same recorded data are presented for different filters. The cheb40 is used in realization of the deterministic quantum teleportation and the boxcar filters are compared with it. The boxcar filters are chosen so that the paramp pump tone is filtered out and are meant for the feed-forward process to reduce its effective delay. The maximal single-shot readout fidelity is found to be reduced by 1 % for the boxcar32 and by 2.2 % for the boxcar16. Therefore, the boxcar16 filter is implemented in the feed-forward to minimize the group delay of the filter.

In Figure 6.3 the single-shot readout results of the same unfiltered data are plotted and the mean values of the different states are shown by black dots. In all cases the maximal readout fidelity is extracted for the optimal rotation in the I-Q plane, the offsets in I, Q and the optimal readout time where the filter length defines integration time. Moreover, the threshold in I and Q are found under the condition that the separation lines are orthogonal to each other which is required for the feed-forward application in the FPGA (see Section 4.4). This algorithm is used in the feed-forward experiments presented in Section 6.2 to determine the optimal thresholds in I and Q as well as the optimal rotation in the I-Q-plane.

For the boxcar16 filter a wider spread of all four states is visible in Figure 6.3 in comparison with the other two filters. This can be explained by the lower effective integration time, but results only in a 2.2 % lower maximal fidelity . Considering the individual readout fidelities, one can state that the readout fidelities are most similar with the boxcar16 filter between 78 % and 68 % whereas asymmetric for the cheb40 filter 87 % to 59 % and the boxcar32 filter 88 % to 59 %. This can be explained by a fast decay especially of the $|02\rangle$ and $|20\rangle$ states during the measurement of which the mean values are clearly shifted towards the $|00\rangle$ state. A decay of the $|22\rangle$ state is only marginally detected. A reason can be that the $|12\rangle$ and $|21\rangle$ states cannot be distinguished from the $|22\rangle$ state in this measurement. Under these conditions the optimal integration length is shifted to smaller times. Therefore, the boxcar16 filter performs equally than the other two in the present experimental situation. This does not imply that this result can be directly generalized to different experimental setups, but it is sufficient for our purposes in the first experimental implementation of the feed-forward setup.

In Figure 6.4 the highest experimentally achieved two-qubit readout fidelity with the boxcar16 filter is presented where the paramp pump tone has been recalibrated so that a gain of 20 dB and cancellation below 0 dB has been reached. Furthermore, pre-selection measurements of 500 ns before the preparation of the qubits are performed. Only those measurement traces are taken into account where both qubits are found in the ground state in the pre-selection measurement. We have analyzed about 65 % of all runs for this measurement and have found a maximal readout fidelity of 78.8 %. This can be compared to the readout fidelity in the deterministic quantum teleportation experiment (cheb40 filter) of 80.7 %. The large black points in Figure 6.4 mark the four mean values of the $|00\rangle$, $|02\rangle$, $|20\rangle$, $|22\rangle$ states where the points labeled with with numbers show the simulated mean values. The orange points show the expected steady state positions, whereas the black ones indicate the dynamical solutions. The χ/κ ratios between the $|2\rangle$ and $|0\rangle$ levels are extracted from resonator spectroscopy measurements where the qubits are prepared in one of the four different states like presented in Figure 3.9b for the $|0\rangle$ and $|1\rangle$ levels. For the fit ϵ_0, offsets in I and Q, the detuning Δ, a rotation ϕ_{LO} and t_{meas} are fit parameters. This simulation results indicate that the steady state of the measurement is not reached for this integration time at the beginning of the measurement, but like explained above the readout fidelity gets limited due to decay for later measurement times.
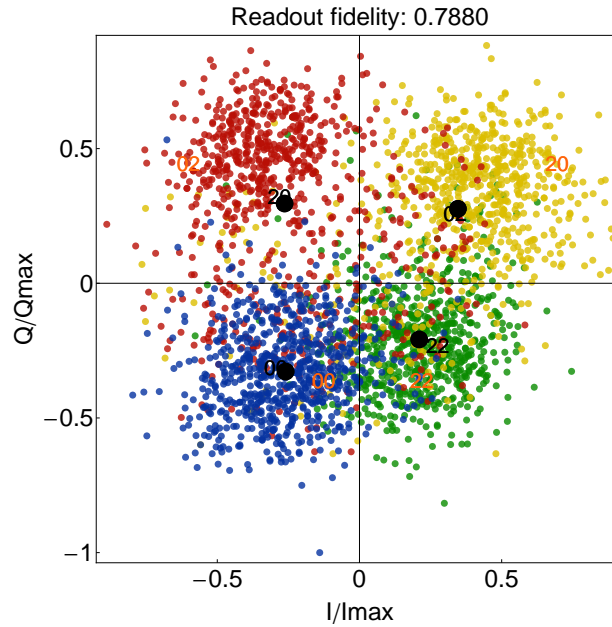
Figure 6.4: Histogram of the single-shot readout of the four two-qubit states in the I-Q-plane. No further integration besides the boxcar16 filter is performed in the analysis like in the feed-forward process. The black dots mark the mean values of the four points and the points labeled with numbers are the simulated mean values. The orange points show the expected steady state values whereas the black ones are simulated with non-steady state solution and predict the experimental mean values well. A single-shot readout fidelity of 78.8 % is extracted which underlines the choice of the boxcar16 filter to be applied in the feed-forward measurements.

Summarizing, the boxcar16 filter seems an appropriate choice for the two-qubit single-shot readout in the full quantum teleportation experiment due to the speed advantage in the feed-forward process and the achieved single-shot readout fidelities close to the cheb40 filter. A further improvement is the implementation of an optimal Bayesian filter in a look-up table on the FPGA to increase the readout fidelity while keeping the computational costs low [48]. Furthermore, one can minimize the cabling in the setup and a try to switch the feed-forward pulse with fast RF switches which have switching times in the order of 10 ns and hence, optimize the delay. Furthermore, the theoretical considerations of Section 3.4 allow a good prediction of the expected single-shot mean values also for short readout times at the beginning of the measurement.

6.2 Examination of the feed-forward setup and outlook to further experiments

To examine the feed-forward setup a test which contains all three qubits in a similar way like in the quantum teleportation protocol has been executed. Therefore, Qb1 and Qb2 are prepared in one of the four states $|00\rangle$, $|02\rangle$, $|20\rangle$, $|22\rangle$ and a joined two-qubit single-shot readout is performed. Dependent on this measurement result a π-pulse is given on Qb3 to excite it only in a specific case. Finally, Qb3 is also measured in a single-shot readout. Here, all four states have been selected individually. The new TvModeV02 feedback application (see 4.4) has been used and hence, also tested. The single-shot readout results of Qb3 for the individual selection of the states can be seen in Figure 6.5. The different colors correspond to

the prepared state of Qb1 and Qb2 as in the two-qubit readout of Figure 6.4. Qualitatively, an excitation of Qb3 dependent on the selected two-qubit state is visible in all four cases. This can be underlined by the total state fidelity which includes all preparation errors for the four different states and is shown above each plot. Therefore, fidelities between 81.5 % and 85.2 % are obtained giving an estimation of the performance of the feed-forward setup. But these fidelities do not directly correspond to feed-forward operation in the quantum teleportation protocol. Since in this test a pulse has only been given dependent on one state, only readout errors between this state and the others are of relevance. However, those among them are not taken into account. In the full quantum teleportation a different feed-forward pulse has to be given in each of the four cases and therefore, all readout errors are of importance. This explains also how a higher state fidelity on Qb3 than the readout fidelity of Qb1 and Qb2 is obtained, which should limit the state fidelity of Qb3. To analyze this result further, one can also extract the excited state occupation P(e) of Qb3 only in the case where it should be excited. For the state $|00\rangle_{Qb1,Qb2}$ P(e)$\approx$ 75 %, $|02\rangle_{Qb1,Qb2}$ P(e)$\approx$ 68 %, $|20\rangle_{Qb1,Qb2}$ P(e)$\approx$ 80 % and $|22\rangle_{Qb1,Qb2}$ P(e)$\approx$ 60 % are found. On the other hand, readout fidelities of the individual sates of 89 ± 3 %, 70 ± 5 %, 77 ± 2 %, 74 ± 1 % are measured. For the $|02\rangle_{Qb1,Qb2}$ and $|20\rangle_{Qb1,Qb2}$ cases the excitations of Qb3 can be understood by the readout fidelities where for the other two states deviations of 15 % are found. For this disparity no explanation is identifiable in this experiment and therefore should be analyzed in the next experiment run.
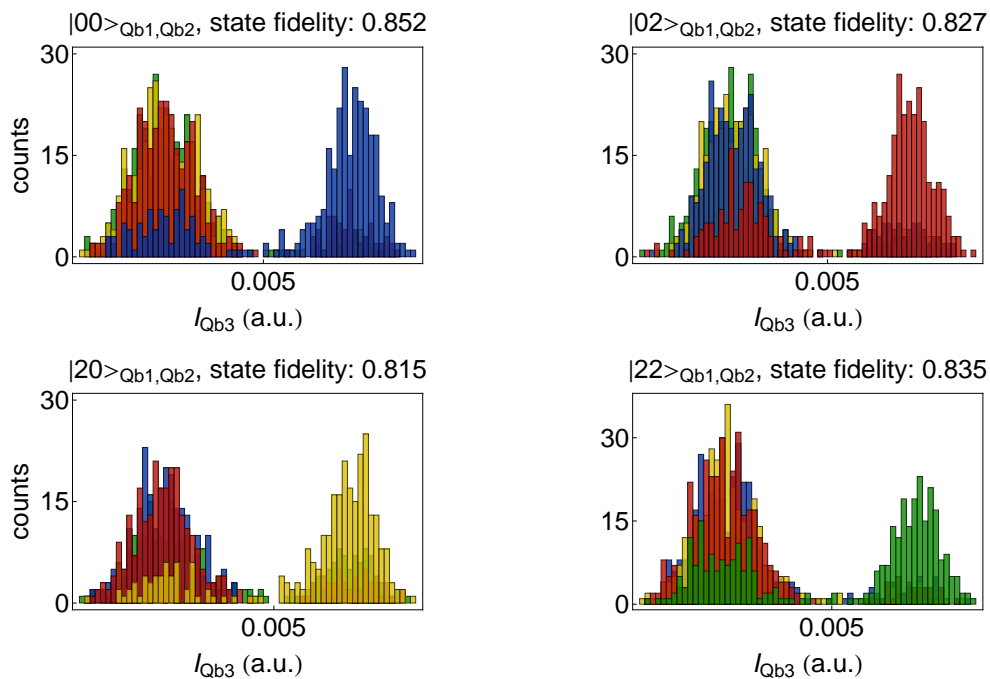
Figure 6.5: The occupancies of Qb3 are depicted. Qb1 and Qb2 are prepared in all four different states which are colored as in the single-shot readout result in Figure 6.4. A pulse is given on Qb3 dependent on this measurement results. The plots are presented in the way that always the selected state is plotted in front of the others. Qualitatively, the occupation of the excited state of Qb3 is mostly given for the selected state of the two-qubit readout which is also underlined by the state fidelities.

In summary, this experimental test indicates the functionality of the implemented feed-forward setup and the enhanced FPGA application to perform pulses dependent on the measurement

result of a two-qubit single-shot readout. This result allowed us to try a first experimental realization of the full quantum teleportation algorithm. Unfortunately, we struggled already with problems for repeating the deterministic quantum teleportation in this experimental run and therefore, could only reach process fidelities of the whole algorithm of less than 40 %.

Finally, suggestions for a more detailed evaluation of the feed-forward setup will be presented. In a possible test Qb3 could be implemented by applying a $\frac{\pi}{2}_x$-pulse at the time where it gets entangled with Qb2 in the teleportation algorithm. Qb3 can then be brought to the excited state with a second $\frac{\pi}{2}_x$-pulse which should be performed like the π-pulse in the experimentally realized test by the feed-forward setup (Figure 6.6a). In this test one could also do quantum tomography on Qb3 and therefore can extract the influence of the coherence and dephasing of Qb3 as well as of phase drifts between the different system which generate pulses on Qb3. Moreover, the opportunities of using spin-echo sequences to reduce the effects of dephasing like the Hahn echo [45] or the Carr-Purcell-Meiboom-Gill sequence [15] can be studied.
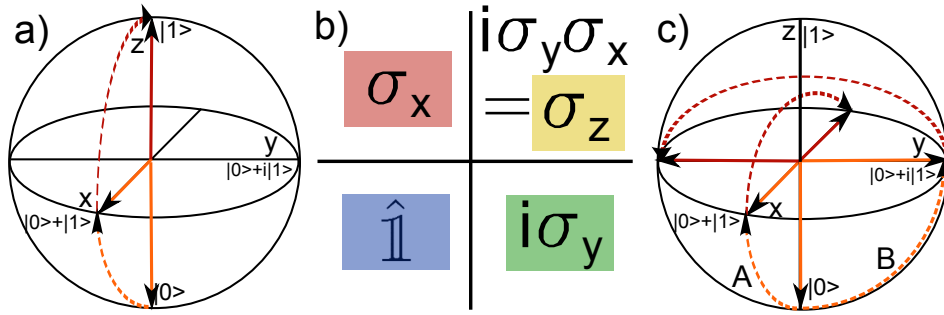

Figure 6.6: a) To examine the feed-forward setup in more detail different pulse schemes are possible. Here, an idea to test the phase stability as well as the influence of the coherence time is shown. b) The feed-forward pulses which are required in the quantum teleportation experiment are illustrated. The idea is to use an $\hat{\sigma}_x$- and $i\hat{\sigma}_y$-gate where the $\hat{\sigma}_z$-gate is the combination of both. b) A second idea of an experimental test for the feed-forward setup to evaluate the different feed-forward pulses without the requirement of two-qubit gates. This allows a direct test of the feed-forward setup excluding errors from the two-qubit gates.

Additionally, one could also evaluate the same feed-forward scheme as in the quantum teleportation protocol (Figure 6.6b). Therefore, Qb3 should be first prepared with a $\frac{\pi}{2}_x$-pulse. Applying one of the four operations $\hat{\mathbb{1}}$, $\hat{\sigma}_x$, $i\hat{\sigma}_y$, $\hat{\sigma}_z$ on this state rotates it to ± 1 on x-axis

$$
\begin{aligned}
\hat{\mathbb{1}}, \ \hat{\sigma}_x \ \frac{1}{\sqrt{2}}(|0\rangle + |1\rangle) &= \frac{1}{\sqrt{2}}(|0\rangle + |1\rangle) \\
i\hat{\sigma}_y, \ \hat{\sigma}_z \ \frac{1}{\sqrt{2}}(|0\rangle + |1\rangle) &= \frac{1}{\sqrt{2}}(|0\rangle - |1\rangle)
\end{aligned}
\tag{6.1}
$$

which allow to distinguish the $\hat{\mathbb{1}}$, $\hat{\sigma}_x$ gates from the $i\hat{\sigma}_y$, $\hat{\sigma}_z$ operations. Second, Qb3 can be prepared with a $\frac{\pi}{2}_y$-pulse in the $1/\sqrt{2}(|0\rangle + i|1\rangle)$ state and therefore, the Qb3 ends up in different states for the $\hat{\mathbb{1}}$, $i\hat{\sigma}_y$ and the $\hat{\sigma}_x$, $\hat{\sigma}_z$ gates (Figure 6.6c). Out of this a process fidelity can be extracted which benchmarks the feed-forward operations without the need of two-qubit gates. If this test as well as the deterministic quantum teleportation with the readout of Qb3 at the point in time of full algorithm are successful, the combination of both to the full quantum teleportation protocol should finally work.

7 Conclusion

The main idea behind the present master thesis is the further analysis of the single-shot readout related to feedback experiments. Therefore, a existing setup was given for the single-qubit experiments where already feedback experiments had been performed [48]. In a first step two different qubit frequencies have been evaluated according to their single-shot readout performance and quality for quantum feedback experiments. These experiments have been performed at both points resulting in clear results which were limited by the phase stability of paramp pump tone in comparison to the resonator drive. Therefore, further technical improvements of the system have been realized resulting in a distinctly increased phase stability by combining both tones at the same microwave generator. This allowed us to calibrate the single-shot readout more carefully and to achieve nearly symmetrically qubit state distributions. Due to this improvements the feedback setup could be evaluated in more detail. Experimental data has been recorded which is mainly explainable by the decay of the qubit during the feedback operation. Furthermore, the suppression of Rabi oscillation on the basis of feedback operations has been demonstrated and a qubit state initialization protocol has been implemented. The reduction of thermal excitation of the qubit could be shown in the recorded data. However, the initialization to the ground state out of an arbitrary superposition state to enable a fast qubit reset was limited by the decay of the qubit during the feedback operation. Hence, the active initialization method did not exceed the passive one in respect to the occupation of the ground state. But it has already been shown that it can be performed much faster than this method. Therefore, no fundamental restrictions of the presented feedback protocols are found during the experiments.

The developed tools for the single-qubit feedback experiments together with the here presented results allow a implementation in other quantum experiments where an initialization in the ground state with a high accuracy is necessary. Therefore, also a repeated initialization sequence can be implemented to increase the quality of the preparation further. This sequence is especially interesting for quantum algorithm which assume all qubits initialized in the ground state as well as for quantum error correction where well initialized ancilla qubits are required. Implementing this method will increase the efficiency of the quantum algorithm in superconducting circuit even further going towards the realization of deterministic quantum computing.

A further experiment can be performed with qubits of an increased lifetime where the full active qubit state initialization out of an arbitrary qubit state should be possible. This will finally allow to use the state initialization by measurement to decrease the measurement duration which becomes interesting for long qubit lifetimes in the future.

For the multi-qubit experiments a feed-forward setup has been built up to fulfill the requirements of the full quantum teleportation algorithm. Therefore, the single-qubit feedback setup has been extended to be able to perform two independent feedback or feed-forward operations. Furthermore, the possibility to apply these operations dependent on the single-shot results of a joined two-qubit readout has been implemented. Experimental tests of the two-qubit single-shot readout with a boxcar filter which is required to minimize the feed-forward delay have been performed and readout fidelities which are nearly similar to those measured with a Chebychev filter have been obtained. In this context, the two-qubit single shot readout has been analyzed theoretically to predict the mean values of the experimental results in the I-Q plane. This has been required to extract qubit frequencies for an appropriate separation of the four two-qubit states. Furthermore, these analytical results have been compared to the experimental data finding a consistent method to fit the data for the average as well as for the single-shot measurements.

Moreover, the performance of the feed-forward setup has been evaluated experimentally and a first, experimental try of the full quantum teleportation algorithm was implement which has not been successful so far. This was mainly due to technical issues which can hopefully be solved in the near future.

The feed-forward setup of the multi-qubit experiments can be investigated in more detail in relation to the other components of the system. Here, especially the phase stability as well as the influence of coherence and dephasing times of the qubits can be studied. Furthermore, improvements such as spin-echo schemes can be implemented to reduce errors due to dephasing in quantum algorithms. In addition, new protocols can be realized with the available tools and the multi-qubit sample like the creation and stabilization of entanglement from an initially separable state. Therefore, several feedback based measurement schemes have been proposed, e.g. by Sarovar et al. [69] or Liu et al. [53] which are adaptable to the present experimental conditions.

Nevertheless, the next step in the multi-qubit experiments shall be focused on the first realization of the full quantum teleportation algorithm in macroscopic system which is "by golly a wonderful problem" like Richard Feynman pointed out.

Bibliography

[1] Markus Ansmann, H. Wang, Radoslaw C. Bialczak, Max Hofheinz, Erik Lucero, M. Neeley, A. D. O'Connell, D. Sank, M. Weides, J. Wenner, A. N. Cleland, and John M. Martinis. Violation of Bell's inequality in Josephson phase qubits. *Nature*, 461(7263):504–506, September 2009.

[2] K.J. Astrom and R.M. Murray. *Feedback Systems: An Introduction for Scientists and Engineers.* Princeton University Press, 2008.

[3] MD Barrett, J Chiaverini, T Schaetz, J Britton, WM Itano, JD Jost, E Knill, C Langer, D Leibfried, R Ozeri, and DJ Wineland. Deterministic quantum teleportation of atomic qubits. *Nature*, 429(6993):737–739, JUN 17 2004.

[4] M. Baur, A. Fedorov, L. Steffen, S. Filipp, M. P. da Silva, and A. Wallraff. Benchmarking a quantum teleportation protocol in superconducting circuits using tomography and an entanglement witness. *Phys. Rev. Lett.*, 108:040502, Jan 2012.

[5] Matthias Baur. *Realizing quantum gates and algorithms with three superconducting qubits.* PhD thesis, ETH Zurich, 2012.

[6] Charles H. Bennett, Gilles Brassard, Claude Crépeau, Richard Jozsa, Asher Peres, and William K. Wootters. Teleporting an unknown quantum state via dual classical and Einstein-Podolsky-Rosen channels. *Phys. Rev. Lett.*, 70(13):1895–1899, Mar 1993.

[7] Charles H. Bennett and Stephen J. Wiesner. Communication via one- and two-particle operators on einstein-podolsky-rosen states. *Phys. Rev. Lett.*, 69:2881–2884, Nov 1992.

[8] CharlesH. Bennett. The thermodynamics of computation-a review. *International Journal of Theoretical Physics*, 21:905–940, 1982.

[9] R. Bianchetti, S. Filipp, M. Baur, J. M. Fink, M. Göppl, P. J. Leek, L. Steffen, A. Blais, and A. Wallraff. Dynamics of dispersive single-qubit readout in circuit quantum electrodynamics. *Physical Review A*, 80(4):043840, 2009.

[10] Romeo Bianchetti. *Control and readout of a superconducting artificial atom.* PhD thesis, ETH Zurich, 2010.

[11] A. Blais, J. Gambetta, A. Wallraff, D. I. Schuster, S. M. Girvin, M. H. Devoret, and R. J. Schoelkopf. Quantum-information processing with circuit quantum electrodynamics. *Physical Review A*, 75(3):032329, March 2007.

[12] A. Blais, R.-S. Huang, A. Wallraff, S. M. Girvin, and R. J. Schoelkopf. Cavity quantum electrodynamics for superconducting electrical circuits: An architecture for quantum computation. *Physical Review A*, 69(6):062320, June 2004.

[13] H.-J. Briegel, W. Dür, J. I. Cirac, and P. Zoller. Quantum repeaters: The role of imperfect local operations in quantum communication. *Phys. Rev. Lett.*, 81(26):5932–, December 1998.

[14] M. Büttiker. Zero-current persistent potential drop across small-capacitance josephson junctions. *Phys. Rev. B*, 36(7):3548–3555, Sep 1987.

[15] H. Y. Carr and E. M. Purcell. Effects of diffusion on free precession in nuclear magnetic resonance experiments. *Phys. Rev.*, 94(3):630–638, May 1954.

[16] Andrew M. Childs, Debbie W. Leung, and Michael A. Nielsen. Unified derivations of measurement-based schemes for quantum computation. *Phys. Rev. A*, 71(3):032318, Mar 2005.

[17] J. M. Chow, L. DiCarlo, J. M. Gambetta, F. Motzoi, L. Frunzio, S. M. Girvin, and R. J. Schoelkopf. Optimized driving of superconducting artificial atoms for improved single-qubit gates. *Phys. Rev. A*, 82(4):040305, Oct 2010.

[18] John Clarke and Frank K. Wilhelm. Superconducting quantum bits. *Nature*, 453(7198):1031–1042, June 2008.

[19] A. A. Clerk, M. H. Devoret, S. M. Girvin, Florian Marquardt, and R. J. Schoelkopf. Introduction to quantum noise, measurement, and amplification. *Rev. Mod. Phys.*, 82(2):1155–1208, Apr 2010.

[20] David G. Cory, Amr F. Fahmy, and Timothy F. Havel. Ensemble quantum computing by NMR spectroscopy. *Proceedings of the National Academy of Sciences*, 94(5):1634–1639, March 1997.

[21] A. Cottet. *Implementation of a quantum bit in a superconducting circuit.* PhD thesis, Université Paris 6, 2002.

[22] D. Deutsch. Quantum theory, the Church-Turing principle and the universal quantum computer. *Proceedings of the Royal Society of London. Series A, Mathematical and Physical Sciences*, 400(1818):97–117, July 1985.

[23] L. DiCarlo, J. M. Chow, J. M. Gambetta, Lev S. Bishop, B. R. Johnson, D. I. Schuster, J. Majer, A. Blais, L. Frunzio, S. M. Girvin, and R. J. Schoelkopf. Demonstration of two-qubit algorithms with a superconducting quantum processor. *Nature*, 460(7252):240–244, July 2009.

[24] D. P. DiVincenzo. The physical implementation of quantum computation. *Fortschritte der Physik*, 48(9-11):771–783, 2000.

[25] C. Eichler, D. Bozyigit, C. Lang, M. Baur, L. Steffen, J. M. Fink, S. Filipp, and A. Wallraff. Observation of two-mode squeezing in the microwave frequency domain. *Phys. Rev. Lett.*, 107:113601, Sep 2011.

[26] A. Einstein, B. Podolsky, and N. Rosen. Can quantum-mechanical description of physical reality be considered complete? *Phys. Rev.*, 47(10):777–780, May 1935.

[27] R. P. Feynman. Simulating physics with computers. *International Journal of Theoretical Physics*, 21(6):467–488, June 1982.

[28] S. Filipp, M. Göppl, J. M. Fink, M. Baur, R. Bianchetti, L. Steffen, and A. Wallraff. Multimode mediated qubit-qubit coupling and dark-state symmetries in circuit quantum electrodynamics. *Phys. Rev. A*, 83(6):063827, Jun 2011.

[29] S. Filipp, P. Maurer, P. J. Leek, M. Baur, R. Bianchetti, J. M. Fink, M. Göppl, L. Steffen, J. M. Gambetta, A. Blais, and A. Wallraff. Two-qubit state tomography using a joint dispersive readout. *Phys. Rev. Lett.*, 102(20):200402, 2009.

[30] J. M. Fink, M. Göppl, M. Baur, R. Bianchetti, P. J. Leek, A. Blais, and A. Wallraff. Climbing the Jaynes-Cummings ladder and observing its nonlinearity in a cavity QED system. *Nature*, 454(7202):315–318, July 2008.

[31] Johannes Fink. *Quantum nonlinearities in strong coupling circuit QED*. PhD thesis, ETH Zurich, 2010.

[32] Edward Fredkin and Tommaso Toffoli. Conservative logic. *International Journal of Theoretical Physics*, 21:219–253, 1982.

[33] A. Furusawa, J. L. Sørensen, S. L. Braunstein, C. A. Fuchs, H. J. Kimble, and E. S. Polzik. Unconditional quantum teleportation. *Science*, 282(5389):706–709, 1998.

[34] J. Gambetta, A. Blais, D. I. Schuster, A. Wallraff, L. Frunzio, J. Majer, M. H. Devoret, S. M. Girvin, and R. J. Schoelkopf. Qubit-photon interactions in a cavity: Measurement-induced dephasing and number splitting. *Phys. Rev. A*, 74(4):042318, October 2006.

[35] J. Gambetta, W. A. Braff, A. Wallraff, S. M. Girvin, and R. J. Schoelkopf. Protocols for optimal readout of qubits using a continuous quantum nondemolition measurement. *Phys. Rev. A*, 76(1):012325, July 2007.

[36] J. M. Gambetta, F. Motzoi, S. T. Merkel, and F. K. Wilhelm. Analytic control methods for high-fidelity unitary operations in a weakly nonlinear oscillator. *Phys. Rev. A*, 83(1):012308–, January 2011.

[37] C. W. Gardiner and M. J. Collett. Input and output in damped quantum systems: Quantum stochastic differential equations and the master equation. *Phys. Rev. A*, 31(6):3761–3774, 1985.

[38] K. Geerlings, Z. Leghtas, I. M. Pop, S. Shankar, L. Frunzio, R. J. Schoelkopf, M. Mirrahimi, and M. H. Devoret. Demonstrating a driven reset protocol of a superconducting qubit. *arXiv:1211.0491*, 2012.

[39] C. Gerry and Peter L. Knight. *Introductory Quantum Optics*. Cambridge University Press, 2005.

[40] M. Göppl. *Engineering Quantum Electronic Chips - Realization and Characterization of Circuit Quantum Electrodynamics Systems*. PhD thesis, ETH Zurich, 2009.

[41] M. Göppl, A. Fragner, M. Baur, R. Bianchetti, S. Filipp, J. M. Fink, P. J. Leek, G. Puebla, L. Steffen, and A. Wallraff. Coplanar waveguide resonators for circuit quantum electrodynamics. *Journal of Applied Physics*, 104:113904, 2008.

[42] Daniel Gottesman and Isaac L. Chuang. Demonstrating the viability of universal quantum computation using teleportation and single-qubit operations. *Nature*, 402(6760):390–393, November 1999.

[43] Joonas Govenius. Single-shot qubit readout in circuit qed using parametric amplification. Master's thesis, Laboratory of solid state physics, ETH Zurich, 02 2012.

[44] Lov K. Grover. A fast quantum mechanical algorithm for database search. In *Proceedings of the twenty-eighth annual ACM symposium on Theory of computing*, pages 212–219, Philadelphia, Pennsylvania, United States, 1996. ACM.

[45] E. L. Hahn. Spin echoes. *Phys. Rev.*, 80:580–594, Nov 1950.

[46] Lukas Heinzle. Pump cancellation for a parametric amplifier. Master's thesis, Laboratory of solid state physics, ETH Zurich, 02 2012.

[47] B. D. Josephson. Possible new effects in superconductive tunnelling. *Physics Letters*, 1(7):251–253, July 1962.

[48] Thomas Karg. Feedback control of a superconducting qubit. Master's thesis, Laboratory for Solid State Physics, ETH Zurich, 2012.

[49] Jens Koch, Terri M. Yu, Jay Gambetta, A. A. Houck, D. I. Schuster, J. Majer, Alexandre Blais, M. H. Devoret, S. M. Girvin, and R. J. Schoelkopf. Charge-insensitive qubit design derived from the Cooper pair box. *Phys. Rev. A*, 76(4):042319, 2007.

[50] C. Lang, D. Bozyigit, C. Eichler, L. Steffen, J. M. Fink, A. A. Abdumalikov Jr., M. Baur, S. Filipp, M. P. da Silva, A. Blais, and A. Wallraff. Observation of resonant photon blockade at microwave frequencies using correlation function measurements. *Physical Review Letters*, 106(24):243601, Jun 2011.

[51] Christian Lang. Read-out strategies for multi-qubit states in circuit quantum electrodynamics. Master's thesis, Ludwig-Maximilians-Univers., Munich, 2009.

[52] P. J. Leek, S. Filipp, P. Maurer, M. Baur, R. Bianchetti, J. M. Fink, M. Göppl, L. Steffen, and A. Wallraff. Using sideband transitions for two-qubit operations in superconducting circuits. *Physical Review B*, 79:180511, 2009.

[53] Zhuo Liu, Lülin Kuang, Kai Hu, Luting Xu, Suhua Wei, Lingzhen Guo, and Xin-Qi Li. Deterministic creation and stabilization of entanglement in circuit qed by homodyne-mediated feedback control. *Phys. Rev. A*, 82(3):032335, Sep 2010.

[54] Daniel Loss and David P. DiVincenzo. Quantum computation with quantum dots. *Phys. Rev. A*, 57:120–126, Jan 1998.

[55] Richard G. Lyons. *Understanding Digital Signal Processing*. Prentice Hall PTR, Upper Saddle River, NJ, USA, 2 edition, 2004.

[56] Xiao-Song Ma, Thomas Herbst, Thomas Scheidl, Daqing Wang, Sebastian Kropatschek, William Naylor, Bernhard Wittmann, Alexandra Mech, Johannes Kofler, Elena Anisimova, Vadim Makarov, Thomas Jennewein, Rupert Ursin, and Anton Zeilinger. Quantum teleportation over 143 kilometres using active feed-forward. *Nature*, 489(7415):269–273, September 2012.

[57] J. Majer, J. M. Chow, J. M. Gambetta, J. Koch, B. R. Johnson, J. A. Schreier, L. Frunzio, D. I. Schuster, A. A. Houck, A. Wallraff, A. Blais, M. H. Devoret, S. M. Girvin, and R. J. Schoelkopf. Coupling superconducting qubits via a cavity bus. *Nature*, 449(7161):443–447, September 2007.

[58] Yuriy Makhlin, Gerd Schön, and Alexander Shnirman. Quantum-state engineering with Josephson-junction devices. *Rev. Mod. Phys.*, 73(2):357–400, May 2001.

[59] F. Motzoi, J. M. Gambetta, P. Rebentrost, and F. K. Wilhelm. Simple pulses for elimination of leakage in weakly nonlinear qubits. *Phys. Rev. Lett.*, 103(11):110501, 2009.

[60] Michael A. Nielsen and Isaac L. Chuang. *Quantum Computation and Quantum Information*. Cambridge University Press, 2000.

[61] Markus Oppliger. Tomographic reconstruction of dark states in circuit quantum electrodynamics. Master's thesis, ETH Zurich, 2012.

[62] D. M. Pozar. *Microwave Engineering*. Addison-Wesley Publishing Company, 1993.

[63] E. M. Purcell. Spontaneous emission probabilties at radio frequencies. *Phys. Rev.*, 69:681, 1946.

[64] I. I. Rabi. Space quantization in a gyrating magnetic field. *Phys. Rev.*, 51:652–654, Apr 1937.

[65] M. D. Reed, L. DiCarlo, S. E. Nigg, L. Sun, L. Frunzio, S. M. Girvin, and R. J. Schoelkopf. Realization of three-qubit quantum error correction with superconducting circuits. *Nature*, 482:382–385, February 2012.

[66] M. Riebe, H. Häffner, C. F. Roos, W. Hänsel, J. Benhelm, G. P. T. Lancaster, T. W. Körber, C. Becher, F. Schmidt-Kaler, D. F. V. James, and R. Blatt. Deterministic quantum teleportation with atoms. *Nature*, 429(6993):734–737, 2004.

[67] D. Ristè, J. G. van Leeuwen, H.-S. Ku, K. W. Lehnert, and L. DiCarlo. Initialization by measurement of a superconducting quantum bit circuit. *Phys. Rev. Lett.*, 109:050507, Aug 2012.

[68] Y. Salathé. Towards gigahertz bandwidth digital signal processing in circuit quantum electrodynamics. Master's thesis, ETH Zurich, 2011.

[69] Mohan Sarovar, Hsi-Sheng Goan, T. P. Spiller, and G. J. Milburn. High-fidelity measurement and quantum feedback control in circuit qed. *Phys. Rev. A*, 72:062327, Dec 2005.

[70] Philipp Schindler, Julio T. Barreiro, Thomas Monz, Volckmar Nebendahl, Daniel Nigg, Michael Chwalla, Markus Hennrich, and Rainer Blatt. Experimental repetitive quantum error correction. *Science*, 332(6033):1059–1061, 2011.

[71] Benjamin Schumacher. Quantum coding. *Phys. Rev. A*, 51(4):2738–2747, Apr 1995.

[72] D. I. Schuster, A. Wallraff, A. Blais, L. Frunzio, R.-S. Huang, J. Majer, S. M. Girvin, and R. J. Schoelkopf. AC Stark shift and dephasing of a superconducting qubit strongly coupled to a cavity field. *Physical Review Letters*, 94(12):123602, April 2005.

[73] P. W. Shor. Algorithms for quantum computation: Discrete logarithms and factoring. In *Proceedings, 35th Annual Symposium on Foundations of Computer Science, Santa Fe*, page 124. IEEE Computer Society Press, 1994.

[74] Peter W. Shor. Scheme for reducing decoherence in quantum computer memory. *Phys. Rev. A*, 52:R2493–R2496, Oct 1995.

[75] L. Steffen, A. Fedorov, M. Oppliger, Y. Salathe, P. Kurpiers, M. Baur, G. Puebla-Hellmann, C. Eichler, and A. Wallraff. Realization of deterministic quantum teleportation with solid state qubits. *arXiv:1302.5621*, 2013.

[76] Lars Steffen. Local qubit control in circuit quantum electrodynamics. Master's thesis, Laboratory of solid state physics, ETH Zurich, 2008.

[77] Frederick W. Strauch, Philip R. Johnson, Alex J. Dragt, C. J. Lobb, J. R. Anderson, and F. C. Wellstood. Quantum logic gates for coupled superconducting phase qubits. *Phys. Rev. Lett.*, 91(16):167005–, October 2003.

[78] Lieven M. K. Vandersypen, Matthias Steffen, Gregory Breyta, Costantino S. Yannoni, Mark H. Sherwood, and Isaac L. Chuang. Experimental realization of Shor's quantum factoring algorithm using nuclear magnetic resonance. *Nature*, 414:883, 2001.

[79] R. Vijay, M. H. Devoret, and I. Siddiqi. Invited review article: The josephson bifurcation amplifier. *Rev. Sci. Instrum.*, 80(11):111101, 2009.

[80] R. Vijay, C. Macklin, D. H. Slichter, S. J. Weber, K. W. Murch, R. Naik, A. N. Korotkov, and I. Siddiqi. Stabilizing rabi oscillations in a superconducting qubit using quantum feedback. *Nature*, 490:77 – 80, 2012.

[81] A. Wallraff, D. I. Schuster, A. Blais, L. Frunzio, R.-S. Huang, J. Majer, S. Kumar, S. M. Girvin, and R. J. Schoelkopf. Strong coupling of a single photon to a superconducting qubit using circuit quantum electrodynamics. *Nature*, 431:162–167, 2004.

[82] A. Wallraff, D. I. Schuster, A. Blais, L. Frunzio, J. Majer, S. M. Girvin, and R. J. Schoelkopf. Approaching unit visibility for control of a superconducting qubit with dispersive readout. *Physical Review Letters*, 95:060501, 2005.

[83] G.K. White and P.J. Meeson. *Experimental Techniques in Low-Temperature Physics*. Monographs on the Physics and Chemistry of Materials, 59. Clarendon Press, 2002.

[84] W. K. Wootters and W. H. Zurek. A single quantum cannot be cloned. *Nature*, 299:802–803, 1982.

[85] Bernard Yurke and Eyal Buks. Performance of cavity-parametric amplifiers, employing kerr nonlinearites, in the presence of two-photon loss. *J. Lightwave Technol.*, 24(12):5054–5066, 2006.

[86] Xinlan Zhou, Debbie W. Leung, and Isaac L. Chuang. Methodology for quantum logic gate construction. *Phys. Rev. A*, 62(5):052316, Oct 2000.

Danksagung

Zum Abschluss meiner Arbeit möchte ich mich bei einigen Personen, die zum Gelingen dieser Arbeit beigetragen haben bedanken.

Zuerst gilt mein Dank Andreas Wallraff für die Aufnahme in seine Gruppe, seine hilfreichen und kritischen Fragen zu unseren Experimenten und das sehr gelungene Skiwochenende.

Für seine stete Hilfsbereitschaft, seine Geduld zu all meinen Fragen sowie die angenehme und lehrreich Zeit möchte ich mich besonders bei meinem Betreuer Yves Salathé bedanken. Es hat mir wirklich viele Freude bereitet mit dir zusammenzuarbeiten.

Dies gilt auch für Markus Oppliger und Lars Steffen. Danke, dass ihr uns so freundlich in euer Projekt mitaufgenommen habt und für die interessante und angenehme Zeit beim Experimentieren. Außerdem möchte ich mich auch bei Christian Lang bedanken, dass du immer Zeit hattest für meine Fragen und experimentellen Probleme, bei David Jarausch, für die gegenseitige Hilfe bei unseren Masterarbeiten und bei Anna Stockklauser, für deine Unterstützung und Kekse zum Schreiben dieser Arbeit.

Ein besonders herzlicher Dank gilt meinen Eltern, Christine und Manfred Kurpiers, für ihren Beistand auf meinem ganzen Weg hierher und meiner Freundin Chirstina Kreuzmair für die aufbauenden Momente und die schöne Zeit in den letzten Jahren.